Doctoral Dissertation

Study of ATLAS LVL1 Muon Trigger Performance using Di-muon events

January 2009

Graduate School of Science and Technology,
Kobe University

Hironori KIYAMURA

Doctoral Dissertation

Study of ATLAS LVL1 Muon Trigger Performance using Di-muon events

「アトラス実験におけるダイミューオン事象を用いた
レベル１ミューオントリガーシステムの性能評価」

January 2009

Graduate School of Science and Technology,
Kobe University

Hironori KIYAMURA

Abstract

The ATLAS experiment is one of those using the LHC, the world's largest proton-proton synchrotron collider, which will produce the world's highest center of mass energy of 14 TeV. The major purposes of the experiment are to find the Higgs boson in the Standard Model and to explore the new physics beyond the Standard Model.

In the ATLAS experiment, the performance of the event trigger system is quite important because of the large background environment. The total event rate of about 1 GHz will be reduced to about 200 Hz by the three-level trigger system. As the first step of the event trigger, the level-1 muon trigger selects events with high-p_T muons over the threshold. Its performance has to be evaluated by analyzing collision data from the early stage of the data taking. For this purpose, a strategy to measure the level-1 muon trigger efficiency was established and evaluated using the Monte Carlo simulation. The method is called tag-and-probe method, which uses di-muon events triggered by the single muon trigger. The muon trigger efficiency for low-p_T region is measured using $J/\psi \to \mu\mu$ events and, for high-p_T region, $Z \to \mu\mu$ events are used. As a result, the muon trigger efficiency as a function of p_T is expected to be measured within the statistical uncertainty of about 0.1 % at the plateau and a few percent at the threshold for the integrated luminosity of 100 pb^{-1}. The effect from the background sources was also expected to be up to a few percent.

Using the tag-and-probe method, the muon trigger efficiency can be measured in detail as a function of p_T, η and ϕ of muons. By parameterizing the result, the detailed map called trigger efficiency map can be created. The map is useful for various physics measurements, such as crosssections, primary distributions of produced particles and multi-muon trigger efficiencies. For example, the di-muon trigger efficiency for $J/\psi \to \mu\mu$ events was calculated using the map. The expected accuracy of measured di-muon trigger efficiency is a few percent.

In this thesis, performance of the tag-and-probe method was evaluated using the Monte Carlo simulation. We have developed a tool for the measurement for low-p_T region. Using the tool, we'll measure the muon trigger efficiency for low-p_T muons, which is very important in the early stage of the data taking, and evaluate the performance of the system.

Contents

1 Introduction

LHC and its goal

Today, it is considered that the smallest unit of matter is an elementary particle. Through the past studies, it is found that there exist twelve types of elementary particles and their natures have been revealed. They are categorized to quarks and leptons in three generations, where each generation consists of two quarks and two leptons. All atoms consist of the quarks and leptons in the first generation.

The interactions between elementary particles are described in the Standard Model. The Standard Model is based on the gauge theory and all interactions are described to be mediated by gauge bosons. For example, the strong, electromagnetic and weak interactions are mediated by gluons, photons, and W or Z bosons, respectively. Note that the gravitational interactions are not included in the Standard Model.

In a simple gauge theory, gauge bosons should be massless. However, W and Z bosons were found to be massive. To explain the existence of their mass, the Higgs mechanism was introduced. W and Z bosons interact with the Higgs field and they obtain their mass by the spontaneous symmetry breaking of the vacuum of the Higgs. Productive researches have been carried out for more than ten years at the Large Electron-Positron Collider (LEP) in CERN and TEVATRON in Fermi National Accelerator Laboratory in USA. Their highlights were the verification of the Standard Model up to an energy scale of about 200 GeV, the precision measurement of the W and Z masses and finally the discovery of the top quark.

As a result of the Higgs mechanism, a neutral Higgs boson appears in the Standard Model. However, it has not been discovered yet in the past experiments. A direct evidence of the existence of the Higgs boson is demanded in order to prove the correctness of the Standard Model.

Even if the Higgs boson is discovered, there still exists a problem called as the hierarchy problem. The Supersymmetry is considered as a solution of the problem. It is a symmetry that relates elementary particles of one spin to another particle that differs by half a unit of spin, where it is called as a superpartner. Superpartners of ordinary particles in the Standard Model are considered to exist close to the TeV energy scale. Therefore, the discovery of superpartners is greatly expected.

In the year 2008, the Large Hadron Collider at the European Organization for Nuclear Research (CERN) came into operation. It is the world's largest proton-proton synchrotron collider which accelerates a bunch of protons to 7 GeV, resulting in the world's highest center of mass energy of 14 TeV. This is 7 times higher than that at the TEVATRON, the most powerful hadron collider in the past. The LHC can produce the energy scale up to a few TeV, which is enough to produce the new particles.

Another feature of the LHC is its high design luminosity of 10^{34} cm^{-2} s^{-1}, with which studies for rare physics processes can be done. To achieve such high luminosity, the bunch crossing rate is 40 MHz corresponding to 10^9 events/second.

At one of the four colliding points at the LHC, a general-purpose detector called ATLAS (A Toroidal

LHC ApparatuS) is placed. The detector is 22 m in height and 44 m in length and its weight is about 7000 tons. In the experiment, from the studies for new physics down, various physics studies are performed.

Muon trigger in the ATLAS experiment

Because of the high luminosity of the LHC and large cross-section of proton-proton inelastic interactions, there are a lot of background events produced and we have to extract events of interest from them. In the ATLAS experiment, the event selection is done by the three-level trigger system. The first, second and third part is called the level-1 trigger, the level-2 trigger and the event filter, respectively. After the event filter, the event rate will be reduced to about 200 Hz. Because of the unexplored energy region realized by the LHC, required performance for the event selection system is quite high especially for the level-1 trigger, where the event rate have to be reduced to about 75 kHz with identifying the bunch crossing. Therefore, in addition to its good selection efficiency, time resolution of less than 25 ns have to be achieved.

The level-1 trigger system is divided into two parts: one is using the muon system and the other is using the calorimetry. From here, the subject is pursued focusing on the level-1 muon trigger.

While almost all particles from the interaction point are caught by the calorimetry, muons can reach outside of the calorimetry because of their mass 200 times heavier than the electron mass. Therefore, muons can be detected under the clean environment even in the ATLAS experiment. In addition, they often appear in the final state of target physics events. Therefore, selecting events using muons is very efficient and effective in such a high background environment at the LHC.

The level-1 muon trigger is based on the measurement of muon trajectories. By measuring their transverse momentum (p_T), events with high-p_T muons can be selected with six p_T thresholds. If a track is triggered, its triggered position and p_T level are recorded and they are sent to the level-2 trigger.

After the data taking starts, the system has to be evaluated using the collision data. Here, the performance of the level-1 muon trigger is evaluated by its trigger efficiency for a muon. Therefore, a strategy for the muon trigger efficiency measurement from data have to be established. Further, for the quick evaluation, the strategy should be established before the experiment starts. The cross section measurement also requires the precise measurement of the muon trigger efficiency.

In this thesis, two strategy for the muon trigger efficiency measurement are examined and evaluated using the Monte Calro simulation. The one uses events collected by the calorimeter trigger and the other uses events collected by the muon trigger itself. In the latter, so-called “tag-and-probe method” is adopted.

With higher luminosity in future, the level-1 trigger rate for the single muon may exceed its limit of data taking rate even with the highest p_T threshold. In such a case, the di-muon trigger requiring two or more muons over the threshold will be used instead. It is also used for the data taking with the design luminosity to correct events with low-p_T muons. Therefore, the di-muon trigger efficiency should be also measured from the collision data. For this measurement, the muon trigger efficiency can be used. In this thesis, the way of the di-muon trigger efficiency measurement using the muon trigger efficiency is also described.

In the ATLAS experiment, the muon trigger efficiency will be widely measured using the tag-and-probe method. The muon trigger efficiency for high-p_T muons is measured using $Z \to \mu\mu$ events. For low-p_T muons, we established a method to measure the efficiency using J/ψ events. In the early stage of the ATLAS experiment, the muon trigger efficiency for low-p_T muons is important for the detector commissioning and b physics studies. A tool for the measurement has been developed and is waiting for the final adjustment using the collision data. At the beginning of the year 2009, a paper describing the simulation studies in the ATLAS collaboration was published, where our study is contained.

Outline of this thesis

The following contents are included. Chapter 2 contains an overview of the physics motivation of the ATLAS experiment and Chapter 3 shows the experimental apparatuses of the LHC and the ATLAS experiment. In Chapter 4, the overview of the ATLAS event trigger and data acquisition system is shown and the level-1 muon trigger is detailed. Chapter 5 describes the way of the muon reconstruction and its performance briefly. In Chapter 6, the expected performance of the muon trigger system obtained from the Monte Calro simulation is shown. In Chapter 7, two strategies for the muon trigger efficiency measurement are explained and evaluated using the Monte Calro simulation. Chapter 8 describes how to measure the di-muon trigger efficiency from the muon trigger efficiency obtained by the method in Chapter 7. At the end of this thesis, the summary and conclusion are presented.

2 Physics Motivation at the ATLAS experiment

Particle physics deals with the elementary building blocks of matter and their mutual interactions. During the 20th century a theory emerged that successfully describes all known elementary particles and their interactions. This "Standard Model" incorporates the Glashow-Weinberg-Salam theory of electro-weak processes and quantum chromodynamics (QCD)[1][2][3], and only the gravitational interactions are not included. The Standard Model is a quantum field theory that describes the interactions of spin -$\frac{1}{2}$ point-like fermions, whose interactions are mediated by spin -1 gauge bosons. The fermions in the Standard Model are divided into a category of particles that are insensitive to the strong interactions, the leptons, and a category of particles that are subject to the strong interactions, the quarks. Further, they are ordered in three generations of increasing mass, as shown in Table 2.1. Each generation consists of two leptons and two quarks, each set with a difference of unit electric charge. The first generation consists of the electron (e), the electron neutrino (ν_e), the up quark (u) and the down quark (d). All these fermions are stable and are the building blocks of ordinary matter. The up and down quarks form protons and neutrons, which together with the electrons build up the atoms and subsequently all forms of matter surrounding us. The second generation consists of the muon (μ), the muon neutrino (ν_μ), the charm quark (c) and the strange quark (s). These have the same properties as the first generation particles, except they have larger masses and are not stable. Finally, the particles of the third generation, consisting of the tau (τ), the tau neutrino (ν_τ), the top quark (t) and the bottom quark (b), are again heavier. The neutrinos are neutral particles, all other particles are charged. Mass and charge for each particle are also summarized in Table 2.1.

	1^{st} generation	2^{nd} generation	3^{rd} generation	Charge
Neutrinos	ν_e	ν_μ	ν_τ	0
Leptons	e (0.511 MeV)	μ (106 MeV)	τ (1.78 GeV)	-1
Quarks	u (1.5-3.3 MeV)	c (1.16-1.34 GeV)	t (169.1-173.3 GeV)	$+\frac{2}{3}$
	d (3.5-6.0 MeV)	s (70-130 MeV)	b (4.13-4.37 GeV)	$-\frac{1}{3}$

Table 2.1: Matter particles of the Standard Model. Values in brackets indicate their masses.

In the Standard Model, interactions between fermions occur via the exchange of gauge bosons. The electromagnetic force is mediated by the photon (γ). The weak force is mediated via the exchange of either the charged $W^\pm$ or W^- boson or the neutral Z boson. The strong force is mediated by the gluon (g). The photon and the gluon are massless, The mass of the $W^\pm$ is 80.398±0.025 GeV and the mass of the Z boson is 91.1876±0.0021 GeV [1]. They have been observed in experiments.

While the Standard Model well describes the interactions of the components of matter at the smallest scales (10^{-18} m) and highest energies (~200 GeV) accessible by past experiments, there are some problems which have not been solved yet and new theories beyond the Standard Model are needed. In this chapter, two expected theories are briefly mentioned.

2.1 Standard Model Higgs

In a simple gauge theory, all gauge bosons are necessarily massless in order to preserve the local gauge invariance of the theory. However, $W^{\pm}$ and Z bosons have masses. The Higgs mechanism[4][5][6] provides a possible explanation of the origin of the masses through the spontaneous symmetry breaking of the gauge invariance.

2.1.1 Higgs mechanism

The Higgs mechanism is an extension of the Goldstone Theorem which states that if a Lagrangian has a global symmetry which is not a symmetry of the vacuum. Then, there must exist one massless boson, scalar or pseudo-scalar, associated to each generator which does not annihilate the vacuum. In the Higgs mechanism, a weak isospin doublet of complex scalar fields $\phi^0(x)$ and $\phi^+(x)$ is introduced as:

$$\phi(x) = \begin{pmatrix} \phi^+(x) \\ \phi^0(x) \end{pmatrix} = \frac{1}{\sqrt{2}} \begin{pmatrix} \phi_1(x) + i\phi_2(x) \\ \phi_3(x) + i\phi_4(x) \end{pmatrix}. \tag{2.1}$$

It belongs to the $SU(2)_L \otimes U(1)_Y$ multiplets and along with the scalar potential $V(\phi)$ represented as:

$$V(x) = \mu^2 \phi^\dagger \phi + \lambda(\phi^\dagger \phi)^2, \ \lambda > 0. \tag{2.2}$$

This gives a contribution to the electroweak Lagrangian L as:

$$\mathcal{L}_{Higgs} = (D_\mu \phi)^\dagger (D_\mu \phi) - V(\phi), D^\mu = \partial^\mu - i\frac{g}{2}\sigma \cdot \mathbf{W}^\mu - i\frac{g\prime}{2} Y B^\mu, \tag{2.3}$$

where D_μ is the covariant derivative.

The minimum of V corresponding to the ground state of the system (i.e. vacuum) is at $|\phi| = 0$ for the case $\mu^2 > 0$, while, for the case $\mu^2 < 0$, the minimum shifts to

$$|\phi|^2 = \phi^\dagger \phi = \frac{1}{2}(\phi_1^2 + \phi_2^2 + \phi_3^2 + \phi_4^2) = -\frac{\mu}{2\lambda} = \frac{v^2}{2}, \tag{2.4}$$

where v is the vacuum expectation value. This leads to the definition of new field variables, $\eta_1 = \phi_1$, $\eta_2 = \phi_2$, $\eta_3 = \phi_3 - v$ and $\eta_4 = \phi_4$, and the potential takes the form as shown in Fig. 2.1. They have their origin at an arbitrarily minimum chosen as:

$$| < 0|\phi|0 > | = \frac{1}{\sqrt{2}} \begin{pmatrix} 0 \\ v \end{pmatrix}. \tag{2.5}$$

The symmetry of the Lagrangian becomes hidden by the choice of a particular minimum. The Lagrangian expressed in the new fields reveals a massive scalar particle η_3 of mass $\sqrt{2\lambda v^2}$, the Higgs boson H and three massless Goldstone bosons, ϕ_1, ϕ_2 and η_4. These Goldstone bosons can be removed by applying a unitary gauge transformation to $\phi(x)$ such that only the real Higgs field remains like:

$$\phi(x) = U\phi(x) = \frac{1}{\sqrt{2}} \begin{pmatrix} 0 \\ v + H(x) \end{pmatrix}. \tag{2.6}$$

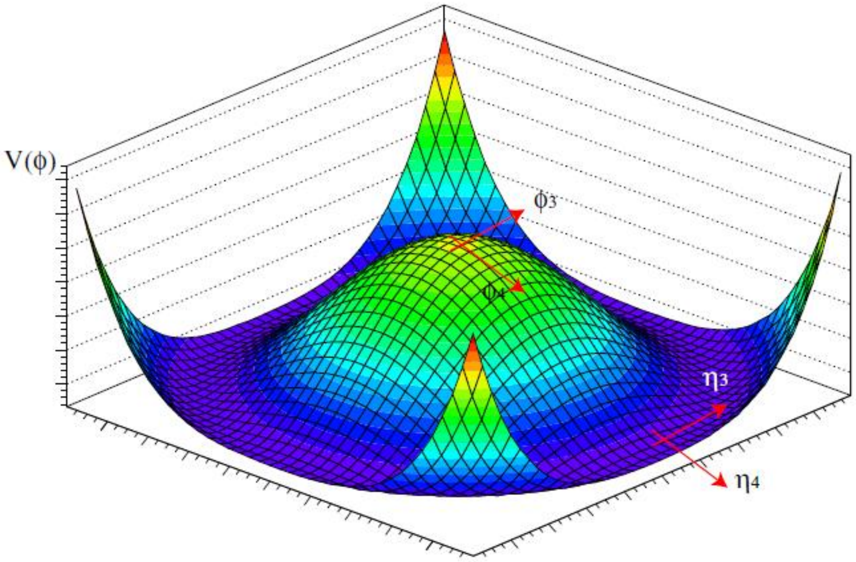

Fig. 2.1: The Higgs potential V for a complex scalar field with $\mu^2 < 0$ and $\lambda > 0$.

In this way, the degree of freedom corresponding to the three disappeared Goldstone boson are eaten by the $W^\pm$ and Z fields which acquire mass and a third, longitudinal polarization state. Then, the gauge boson masses are generated as:

$$\begin{aligned} M_W &= \frac{gv}{2}, \\ M_Z &= \frac{1}{2}v\sqrt{g^2 + g'^2}, \\ M_\gamma &= 0. \end{aligned} \tag{2.7}$$

The massive physical field Z_μ and the massless one A_μ are represented using their mixing angle θ_W (called the Weinberg angle) as:

$$\begin{aligned} A_\mu &= \cos\theta_W B_\mu + \sin W^3_\mu, \\ Z_\mu &= -\sin\theta_W B_\mu + \cos\theta_W W^3_\mu, \end{aligned} \tag{2.8}$$

where the value θ_W satisfies the following equation:

$$\frac{g'}{g} = \tan\theta_W. \tag{2.9}$$

In addition, the Higgs field couples to the fermion matter fields to generate their masses. The coupling of the Higgs field to a fermion pair is parameterized by an arbitrary Yukawa coupling constant $\lambda_f = \sqrt{2}m_f/v$, which is different for each fermion and proportional to its mass m_f. Lepton number conservation is assumed within the SM, giving a diagonal lepton mass matrix. The lack of quark generation number conservation in electroweak interactions means that the observed physical mass eigenstates of quarks are not eigenstates of the weak isospin. The level of quark mixing is parameterized in terms of the Cabibbo-Kobayashi-Maskawa mixing matrix.

2.1.2 Experimental constraint of Higgs mass

The mass of the Higgs boson remains the only unknown parameter in the Standard Model, and several constraints on its mass have been obtained from past experimental measurements. The most stringent bounds on the Higgs mass come from the LEP experiments. A Higgs mass smaller than 114.4 GeV is excluded with a confidence level of 95 % by direct searches at LEP [8]. Furthermore an upper limit on its mass can be obtained from a fit to the electroweak results from LEP and SLD [1]. The result of the fit is shown in Fig. 2.2[7]. It shows the $\Delta\chi^2(m_H) = \chi^2_{min}(m_H) - \chi^2_{min}$ as a function of the Higgs mass. The mass region that is excluded by direct searches is indicated by the grey area. The associated band represents the estimate of the theoretical uncertainty due to higher-order corrections, where the constraints from the mass of the top quark and $W^{\pm}$ bosons observed in the Tevatron experiment are included. After a renormalization of the probability content of the region $m_H > 114$ GeV to 100 %, using the assumption that the prior probability density for m_H is flat in m_H, an upper limit of 199 GeV is obtained with a confidence level of 95 %.

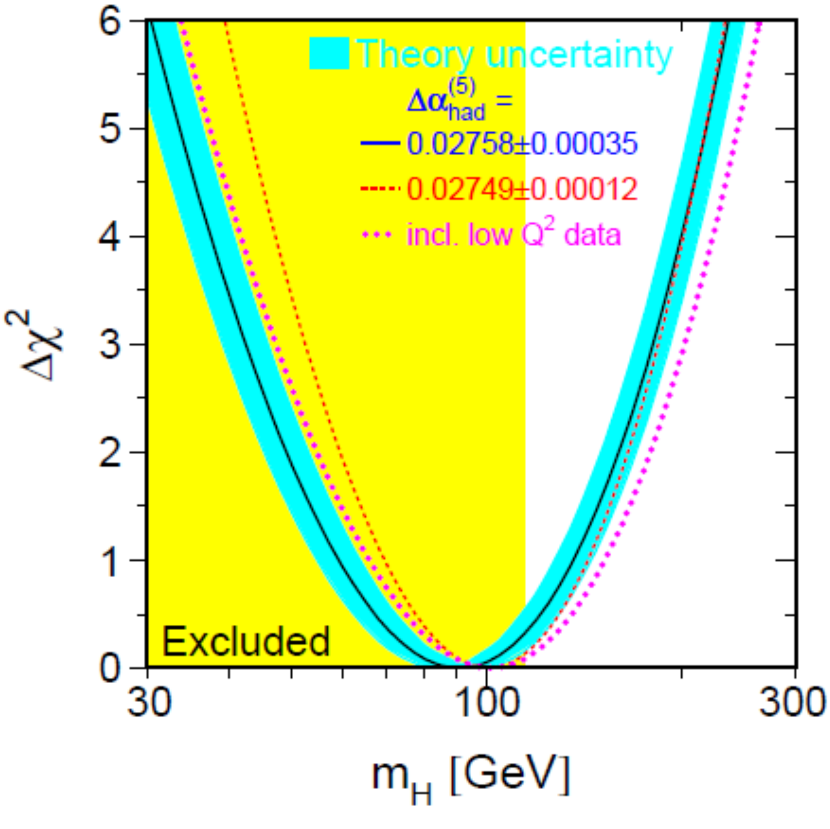

Fig. 2.2: $\Delta\chi^2(m_H) = \chi^2_{min}(m_H) - \chi^2_{min}$ as a function of the Higgs mass[7][8].

2.1.3 Higgs boson production

Figure 2.3 shows typical Feynman diagrams of Higgs boson production processes for the ATLAS experiment. Details for each process are mentioned below.

$gg \to H$

The gluon fusion processes (Fig. 2.3-(a)) proceed primarily through a top quark triangle loop[24][25][26], and is the dominant neutral Higgs boson production mechanism at LHC, with crosssections of roughly 200 - 0.1 pb for $M_{Higgs} = 100 - 1000\text{GeV}$. The dependence of the gluon fusion crosssection on different parton densities yields roughly an additional 15 % uncertainty in the theoretical prediction.

$\underline{qq \to qqV^*V^* \to qqH}$

The vector boson fusion (VBF, Fig. 2.3-(b)) is a shorthand notation for the full $qq \to qqH$ process, where both quarks radiate virtual vector bosons which then annihilate to produce the Higgs boson. The resulting Standard Model crosssections are in the range 5 - 0.01 pb for $M_{Higgs} = 100 - 1000\text{GeV/c}^2$.

$\underline{gg,\ qq \to t\bar{t}H}$

The process gg, $q\bar{q} \to t\bar{t}H$ (Fig. 2.3-(c)) is also relevant only for small Higgs masses. The analytical expression for the parton cross section, even at lowest order, is quite involved, so that just the final results for the LHC cross section are shown in Fig. 2.4.

$\underline{q\bar{q} \to V^* \to VH}$

The crosssection for $q\bar{q} \to W^{\pm}H$ (Fig. 2.3-(d), summed over both W charge states) reaches values of 2 - 0.001 pb for $M_{Higgs} = 100 - 1000\text{GeV/c}^2$. The corresponding $q\bar{q} \to ZH$ crosssection is roughly a factor of two lower over the same Higgs boson mass range. The theoretical uncertainty is estimated to be about 15 % from the remaining scale dependence. The dependence on different sets of parton densities is rather weak and also leads to a variation of the production crosssections by about 15 %. The signature of Higgs boson production in the VH channel are governed by the corresponding decays of the Higgs boson and vector boson.

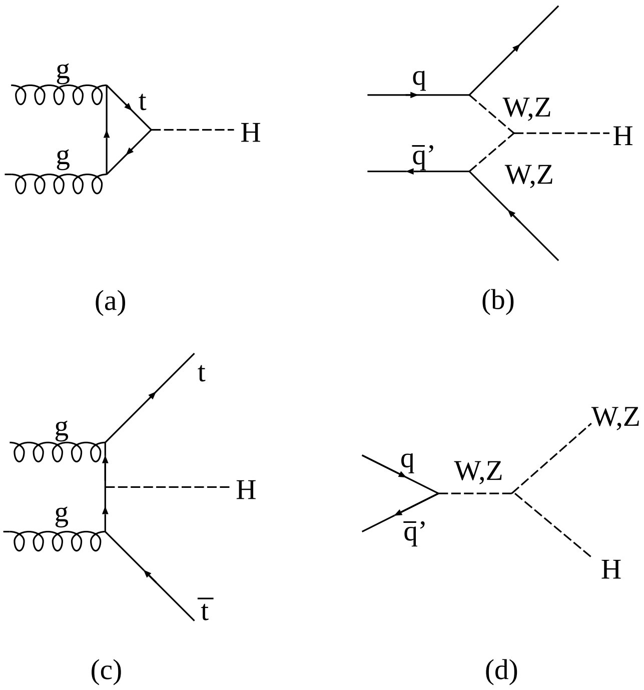

Fig. 2.3: Higgs production diagrams. (a) represents the gluon fusion process, (b) does the Vector Boson Fusion (VBF) process, (c) does the $t\bar{t}H$ production process and (d) does the W/Z associate production process.

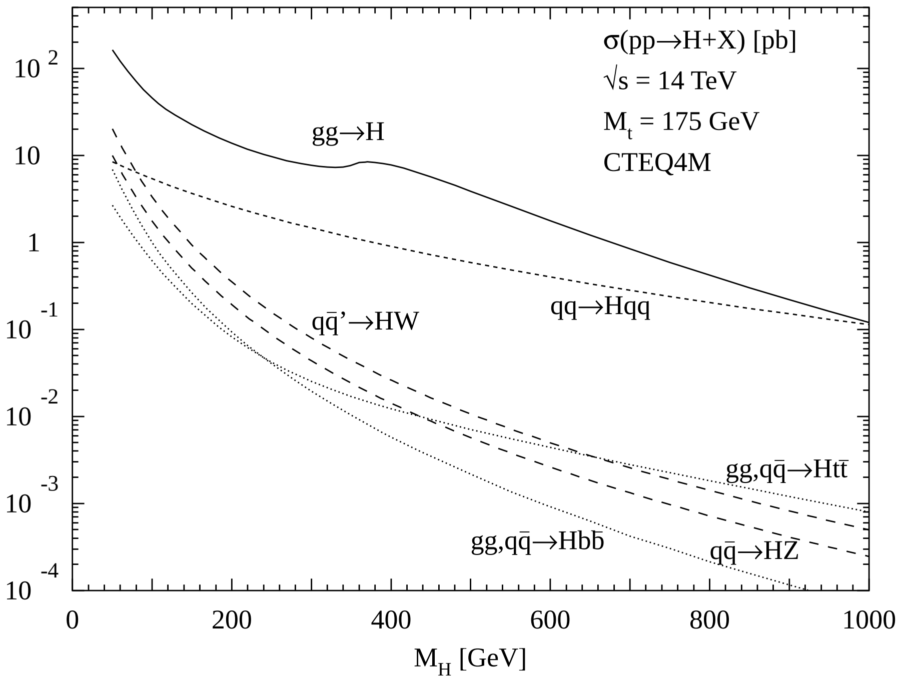

Fig. 2.4: Production crosssection of Higgs[9].

2.1.4 Higgs boson decay and search at ATLAS

For a given Higgs mass, the Standard Model precisely predicts the decay channels of the Higgs, which allows a precise assessment of the Higgs boson properties. The decay width of the Higgs boson as a function of Higgs mass is shown in Fig. 2.5. Here, Higgs decay processes for each Higgs mass M_H are detailed.

- **Low-Mass Higgs Boson ($M_H < 120\text{GeV/c}^2$):**
  Below the WW or ZZ threshold ($M_H < 2M_Z$), the dominant decay into the heaviest accessible pair of quarks
  $$H \to b\bar{b} \tag{2.10}$$
  is swamped by the QCD background (the direct $b\bar{b}$ crosssection is very high, see Fig. 2.5).
  The decay channel
  $$H \to \gamma\gamma \tag{2.11}$$
  suffers an enormous background from $q\bar{q} \to \gamma\gamma$, $gg \to \gamma\gamma$, $gq \to q\gamma\gamma$ and $Z \to e^+e^-$ processes, where the jets or $e^\pm$ fake a γ. These backgrounds can be reduced with excellent photon resolution and excellent γ/jet and $\gamma/e^\pm$ separation. Hence an electromagnetic calorimetry with excellent performance is required.

- **Search for VBF H $\to \tau\tau$ mode**
  When the mass of Higgs is relatively small ($115 < m_{Higgs} < 140$ GeV), a vector boson fusion process with
  $$H \to \tau^+\tau^- \tag{2.12}$$

plays an important role for this discovery. In this channel, $\tau\tau \rightarrow$ leptonic decay + hadronic decay (lepton-hadron mode) is as important as leptonic decay + leptonic decay (lepton-lepton mode) because a branching ratio of hadronic tau decay is larger than that of leptonic tau decay by a factor of ~ 2. It leads this channel to the first discovery of Higgs.

Since W and Z bosons are heavy, the out-going quarks have larger transverse momenta (p_T) than the QCD background processes. They will be observed in a forward region with high-p_T. Tagging these forward jets help us to suppress the background processes. Furthermore, there is no color exchange between two out-going quarks, the Higgs boson will be observed in large rapidity gap, where activities of QCD jets are small.

$H \rightarrow \tau\tau$ provides high-p_T lepton from a leptonic tau decay and it can be used as a trigger of this event. Momenta carried by ν's emitted from τ decays can be estimated using the missing E_T information.

Dominant background process is Drell-Yan with two high-p_T jets and the invariant mass distribution makes a peak at the Z^0 mass.

- **Intermediate-Mass Higgs Boson ($120\mathrm{GeV/c^2} < \mathrm{M_H} < 800\mathrm{GeV/c^2}$):** In this mass region the decay

  $$H \rightarrow ZZ^{(*)} \rightarrow l^+l^-l^+l^- \qquad (2.13)$$

  provides a very clean signature of the Higgs boson. For the range $M_H < 2M_Z$ one of the two Z bosons is virtual (off-shell). For a Higgs mass of 150 $\mathrm{GeV/c^2}$ one expects $\sim$ 550 such events per year. The four leptons have a high transverse momentum ($5\mathrm{GeV/c} < p_T < 50\mathrm{GeV/c}$). The background mainly comes from prompt muons, decay muons, hadronic punch-through, neutrons and muon induced electromagnetic secondaries. To achieve a good acceptance for such kind of events, the geometrical and kinematic acceptance for leptons has to be maximized, the significance of the signal will depend on the four-lepton mass resolution. Hence a good lepton energy and momentum resolution at the level of 1 % is necessary. For large Higgs boson masses the Higgs width increases rapidly and the signal will be rate limited, hence the accelerator luminosity becomes more important than the detector performance.

- **Heavy-Mass Higgs Boson ($M_H > 800\mathrm{GeV/c^2}$):** For a heavy Higgs boson the channel

  $$H \rightarrow ZZ \rightarrow l^+l^-\nu\bar{\nu} \qquad (2.14)$$

  becomes six times more frequent than $H \rightarrow ZZ \rightarrow l^+l^-l^+l^-$ and can be detected with the measurements of two high-p_T leptons and a high missing E_T due to the escaping neutrinos. Also the channels

  $$H \rightarrow WW,\ ZZ \rightarrow l^\pm + \nu + 2jets,\ 2l^\pm + 2jets \qquad (2.15)$$

  provide promising signatures for a heavy Higgs boson.

If these expectations are combined with a simulation of the detector response of the ATLAS experiment, it becomes possible to estimate how well the experiment will be able to find the Higgs boson. Figure 2.6 shows the sensitivity for the discovery of the Standard Model Higgs boson for several Higgs decay channels for the ATLAS experiment. The results shown here assume an integrated luminosity of 30 $\mathrm{fb^{-1}}$ which corresponds to the estimated data volume after the first three years of data taking.

The figure shows that if the Higgs boson exists, the ATLAS experiment will be able to observe it with a 5σ statistical significance over the full mass range from 100 GeV up to 1 TeV.

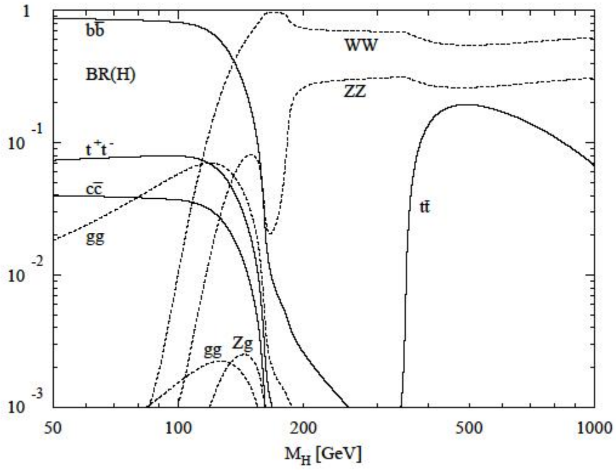

Fig. 2.5: Decay width of the Higgs boson as a function of the Higgs mass (M_H)[9].

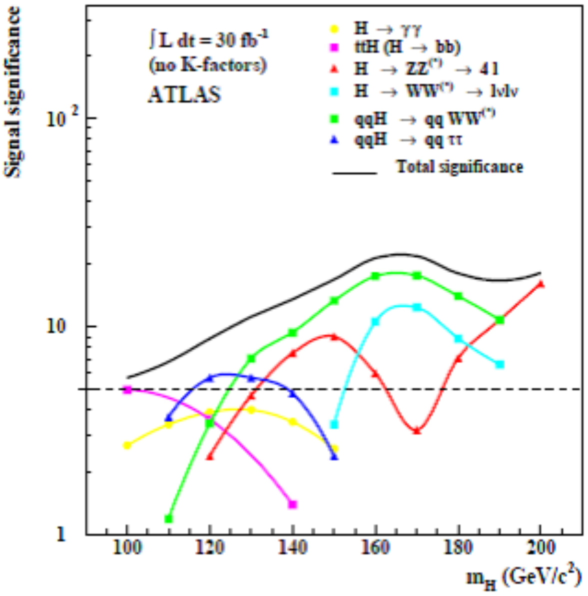

Fig. 2.6: ATLAS sensitivity for the discovery of the Standard Model Higgs boson[10].

2.2 Supersymmetry (SUSY)

Supersymmetry imposes a new symmetry between the fermions and bosons[12][12][13][14][15]. The supersymmetric extension of the Standard Model (SM) makes improvements to phenomenological problems in the physics of elementary particles. It provides a natural solution for the gauge hierarchy problem by introducing one super-partner (sparticle, summarized in Fig. 2.7) with mass at the TeV scale for each SM particle. Moreover, the extrapolation of LEP data within the framework of supresymmetric extension yields a precise unification of gauge couplings at a scale of $\sim 10^{16}$ GeV[16][17]. Due to these properties, SUSY is one of the most attractive alternatives beyond the SM and has been the subject of many studies in particle physics. However, up to now, no direct evidence for SUSY has been found. It is essential to examine the properties of any new states of matter at energy scales close to the threshold for the new phenomena, or in high energy collisions at the TeV energy scale.

2.2.1 Inclusive search for SUSY signature

Sparticle production of gluinos ($\tilde{g}$) and squarks ($\tilde{q}$) occurs dominantly via strong interactions and its rate may be expected to be considerably large at the LHC. Gluino production leads to a large rate for events with multijets via series of cascade decay and the neutral lightest supersymmetric particles (LSP) in the final state which remains stable and undetectable. Therefore, LSPs carry off apparently large missing E_T.

In SUSY, a new quantum number of R-parity is conserved. It is defined as:

$$R = (-1)^{3(B-L)+2S}, \tag{2.16}$$

where B, L and S are the baryon number, lepton number and spin, respectively. R-parity is $+1$ for all Standard Model particles and is -1 for all SUSY particles. This has the consequence that sparticles must be produced in pairs and the LSP is stable.

Since there are no third generation partons in the initial state, gluino and squark production rates are fixed by QCD in terms of the gluino and squark masses ($m_{\tilde{g}}$ and $m_{\tilde{q}}$). Thus, inclusive SUSY searches with the early data rely on excesses of events in the channel of "multijets + large missing E_T"[18], which is a model-independent feature.

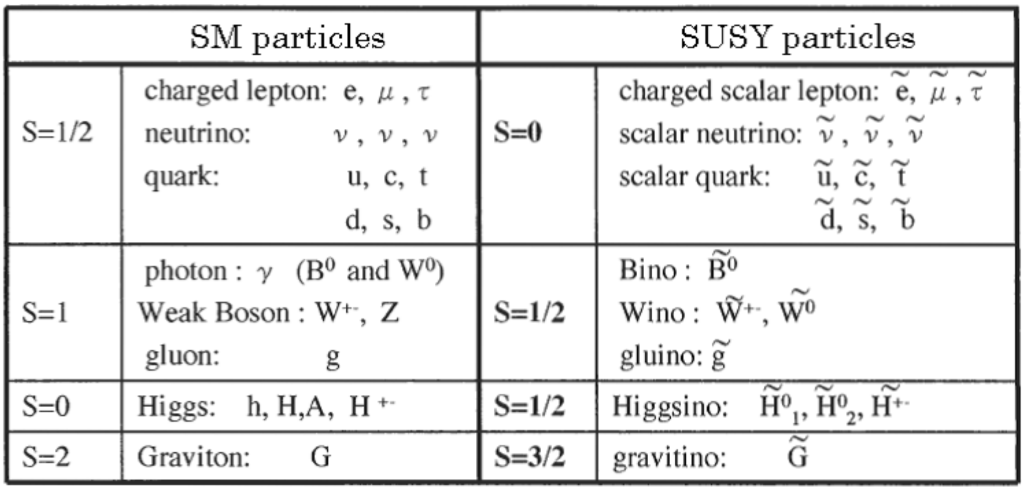

SM particles		SUSY particles	
S=1/2	charged lepton: e, μ , τ neutrino: ν , ν , ν quark: u, c, t d, s, b	**S=0**	charged scalar lepton: $\tilde{e}$, $\tilde{\mu}$, $\tilde{\tau}$ scalar neutrino: $\tilde{\nu}$, $\tilde{\nu}$, $\tilde{\nu}$ scalar quark: $\tilde{u}$, $\tilde{c}$, $\tilde{t}$ $\tilde{d}$, $\tilde{s}$, $\tilde{b}$
S=1	photon : γ (B^0 and W^0) Weak Boson : W^{+-}, Z gluon: g	**S=1/2**	Bino : $\tilde{B}^0$ Wino : $\tilde{W}^{+-}$, $\tilde{W}^0$ gluino: $\tilde{g}$
S=0	Higgs: h, H,A, H^{+-}	**S=1/2**	Higgsino: $\tilde{H}^0_1$, $\tilde{H}^0_2$, $\tilde{H}^{+-}$
S=2	Graviton: G	**S=3/2**	gravitino: $\tilde{G}$

Fig. 2.7: List of the supersymmetric particles.

Considering the features of sparticle production and its decay, the signal candidate events are selected by requiring high-p_T multijets and large missing E_T. Although, at a hadron collider, a pure jet + missing E_T signature is challenging due to the unknown tails of the large QCD background and due to jet mismeasurements. A large amount of missing E_T can be also produced by hard jets and often leptons. To have a better control of the background, one can require one or more additional isolated leptons in the final state. Some of the main ATLAS inclusive SUSY search modes classified by the lepton requirement follow.

- **No-lepton mode:** The presence of multiple jets together with large missing E_T forms the SUSY signature.
- **One-lepton mode:** Requiring one isolated lepton with p_T >20 GeV in addition to the event selection cuts above. It greatly reduces the QCD multijet background and also gives better control over the remaining backgrounds ($t\bar{t}$ and W+jets productions).
- **Two-lepton mode:** Requiring two isolated leptons in addition. Furthermore, same-sign di-leptons can be common in SUSY because the gluino is a self-conjugate Majorana fermion, while the rate is small in SM processes.

Muons, due to their clean experimental identifiability, are particularly suited for background subtraction and the channel of “muon(s) + jets + missing E_T” provides a robust signature for supersymmetry at the LHC.

Finally, SUSY events with large M_{eff} are searched. The effective mass M_{eff} is calculated as:

$$M_{eff} = \sum_{i=1}^{4} p_T^i + missingE_T, \tag{2.17}$$

where p_T^i is the transverse momentum of i-th leading jet.

The value of M_{eff} provides a first estimate of the sparticle masses. Fig. 2.8 shows the M_{eff} distributions for no- and one-lepton modes. If SUSY exists, it is expected that there is an excess over the SM background expectation in the distribution for each event topology with an integrated luminosity up to 1 fb^{-1}. Larger excess can be seen for one-lepton mode than no-lepton mode.

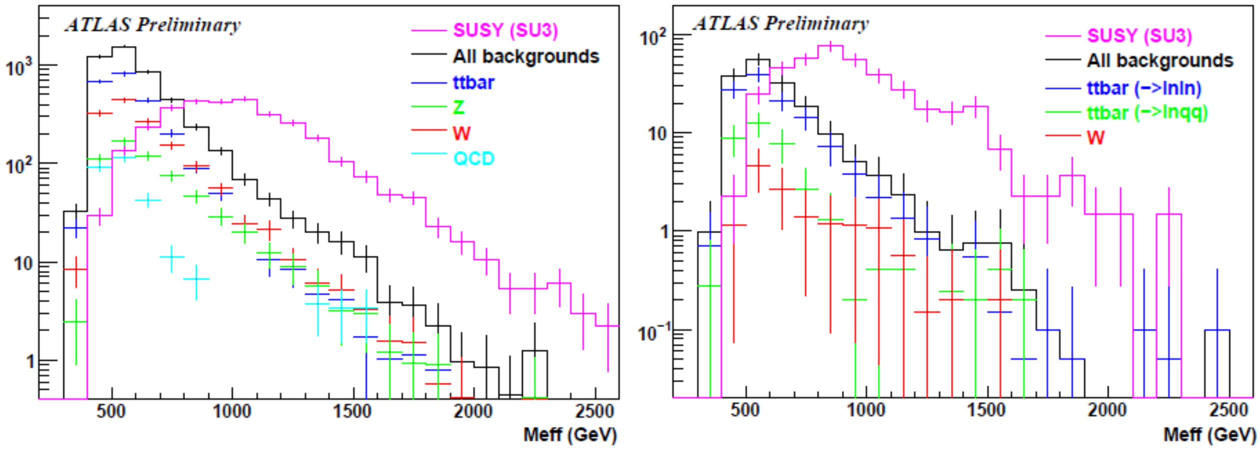

Fig. 2.8: The M_{eff} distributions for no-lepton (left) and one-lepton (right) modes. The histograms are normalized to the integrated luminosity of 1 fb^{-1}[23].

2.2.2 Discovery potential

Figure 2.9 shows 5σ discovery reach in the $m_{\tilde{g}}$-$m_{\tilde{q}}$ space for each event topology in the mSUGRA model[19][20][21][22]. Even for sparticle mass as heavy as ~1 TeV, discoveries are expected for an integrated luminosity of 1 fb^{-1}.

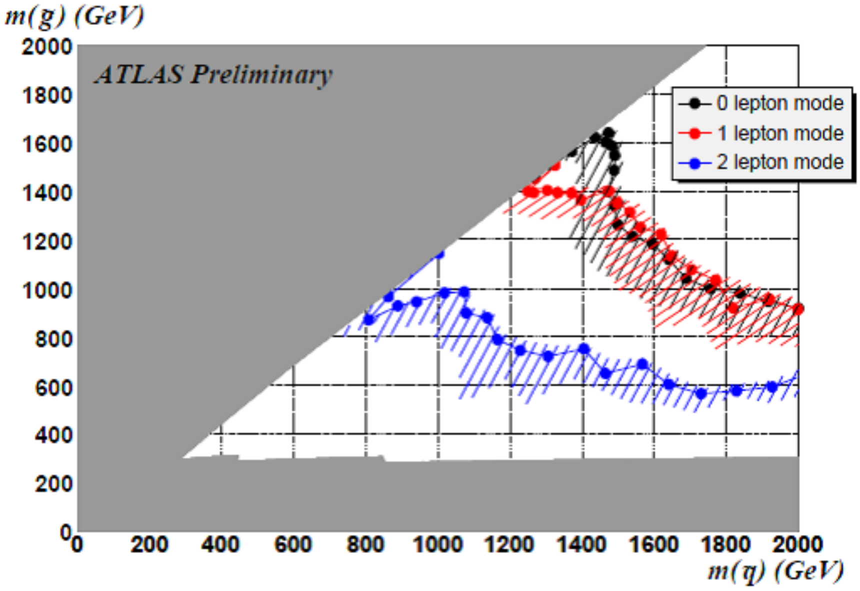

Fig. 2.9: 5σ discovery reaches in the $m_{\tilde{g}} - m_{\tilde{q}}$ space for each event topology[23].

3 Experimental setup

This chapter describes the Large Hadron Collider (LHC) and the ATLAS (A Toroidal LHC ApparatuS) detector. The LHC is a proton-proton collider with a center of mass energy of 14 TeV, which is the largest all over the world. Its design luminosity is $10^{34}\mathrm{cm}^{-2}\mathrm{s}^{-1}$. Bunch crossing rate is 25 ns and total event rate is up to 10^9 events per second. Thus, LHC can reach unexplored energy region for new physics studies. ATLAS is a general-purpose detector at the LHC, with which various physics studies, especially new particle search, will be performed.

3.1 The LHC Accelerator

The LHC is a synchrotron accelerator with a circumference of 26 km and protons are accelerated to 7 TeV there. Super Proton Synchrotron (SPS) is the pre-injector for the LHC and accelerates 26 GeV protons from Proton Synchrotron (PS) to 450 GeV. The beam line of the LHC is composed of accelerating cavities and super-conducting NbTi bending magnets and quadruples for the beam optics. These dipole magnets are placed along two separated beam lines and produce magnetic fields of 8.4 T strength in vertical direction. There are four collision points in the LHC and the following detectors are placed at each point.

1. ATLAS (A Toroidal LHC ApparatuS)
2. CMS (The Compact Muon Solenoid)
3. LHC-B
4. ALICE (A Large Ion Collider Experiment)

ATLAS and CMS are general-purpose detectors, while LHC-B is specialized for b-physics and ALICE is for heavy ion collision (1 PeV Pb-Pb collision at the maximum energy). Locations of these detectors and proton rings are shown in Fig. 3.1.

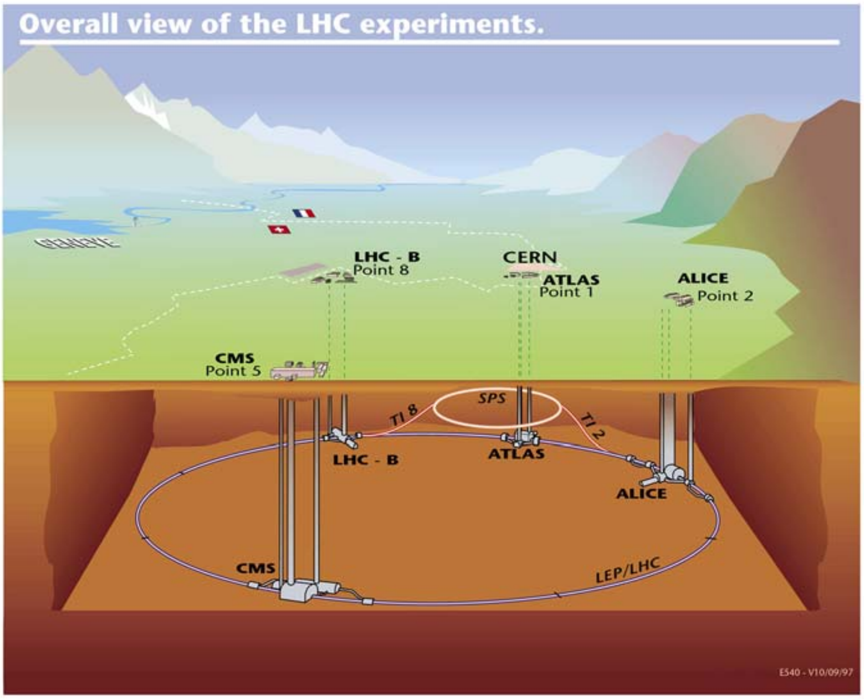

Fig. 3.1: Schematic view of the CERN accelerator complex.

3.1.1 Luminosity

One of the important parameters of a collider is the luminosity L. For a physical process with crosssection σ, the event rate ($\frac{dN}{dt}$) is given by:

$$\frac{dN}{dt} = \sigma \times L. \tag{3.1}$$

In the case of a collider like the LHC, the luminosity is given by:

$$L = \frac{N_{p1} N_{p2} f_{cross}}{4\pi \sigma_x^* \sigma_y^*}, \tag{3.2}$$

where N_{p1} and N_{p2} are the number of protons per each bunch and f_{cross} is the bunch crossing frequency. σ_x^* and σ_y^* are transverse beam sizes of horizontal and vertical direction at the interaction point respectively and $\sigma_x^* \sigma_y^*$ gives crosssection of the beam. It is clear that increase of N_{p1}, N_{p2} and f_{cross} and decrease of σ_x^* and σ_y^* produce high luminosity.

There are mainly two operation modes of luminosity at the LHC; one is called “high-luminosity mode” with design luminosity and the other is “low-luminosity mode” with the luminosity of 10^{33} cm^{-2}s^{-1}. The latter will be continued for the first 3 years. Another mode with the luminosity of 10^{31} cm^{-2}s^{-1} is also planned in the very early stage of the LHC. Parameters of the LHC for the high-luminosity mode are listed in Table 3.1.

Main ring	26658.87 m	Injector energy	450 GeV
Proton energy	7.0 TeV	Number of protons	1.1×10^{11}/bunch
Bunch Length	77 mm	Bunch interval	24.95 ns
beam radius	15.9 μm	beam crossing angle	300 μrad
Luminosity Lifetime	10 hours		

Table 3.1: Parameters of LHC[28].

3.1.2 Particle production rates

As a proton is a composite particle, the center of mass energy of 14 TeV is distributed to each elementary particle. At these energies, not only the valence-quarks but also the gluons holding them together can interact and additionally, a whole sea of quark-antiquark pairs that are allowed a fleeting existence under the law of quantum mechanics, too. Therefore, only mass states up to a few TeV can be created. Figure 3.2 shows the prediction of particle-production crosssection for the particles of the most interest at the LHC together with production rates at the high luminosity mode. One at the Tevatron, which is the proton-antiproton collider at Fermilab, is also shown for a comparison. It can be seen that the total crosssection is more than ten orders of magnitude larger than that of the Higgs production. Therefore, detectors must have capability to handle such an enormous total event rate and distinguish the signals of interest from other events such as proton-proton inelastic events and minimum bias events (QCD events), or backgrounds such as beam halo events and beam gas events.

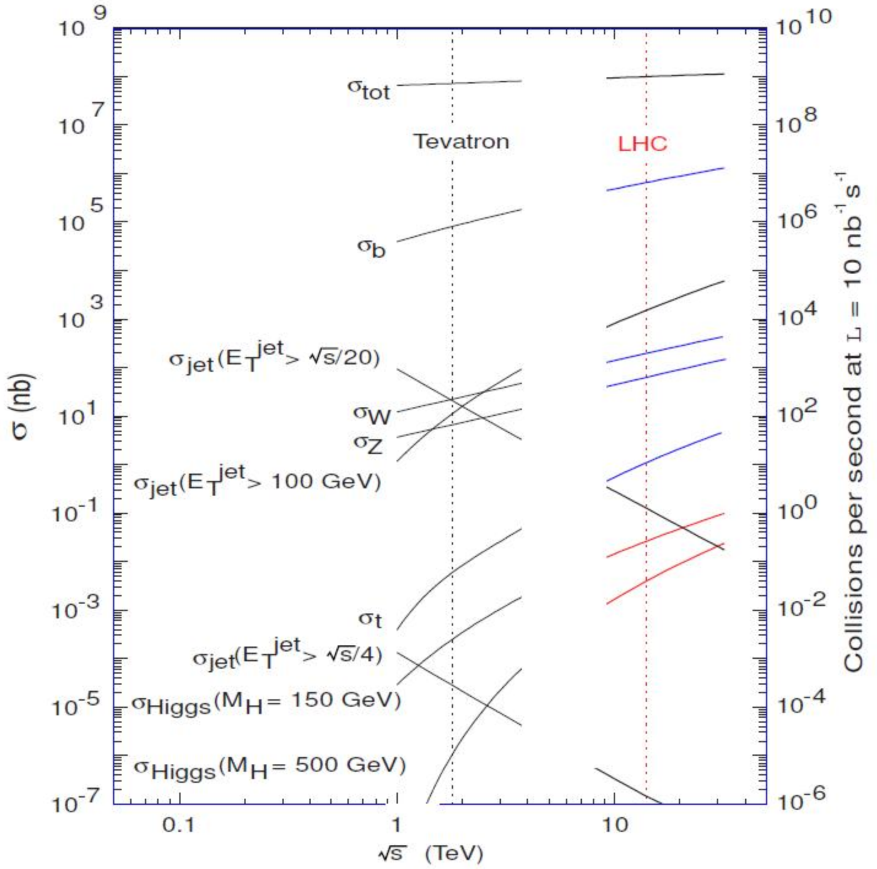

Fig. 3.2: Predicted crosssection of proton-proton interaction as a function of interaction energy as a function of center-of-mass energy. The energy at the Tevatron, Fermilab as well as for the LHC are indicated[33].

3.2 The ATLAS detector

Figure 3.3 shows a 3D view of the whole ATLAS Detector. The ATLAS Detector is characterized by its magnet configuration as follows: a superconducting solenoid is installed around the Inner Detector and large superconducting air-core toroids consisting of independent coils is arranged with an eight-fold symmetry outside the calorimetries. ATLAS is 22 m in height and 44 m in length and its weight is about 7000 tons.

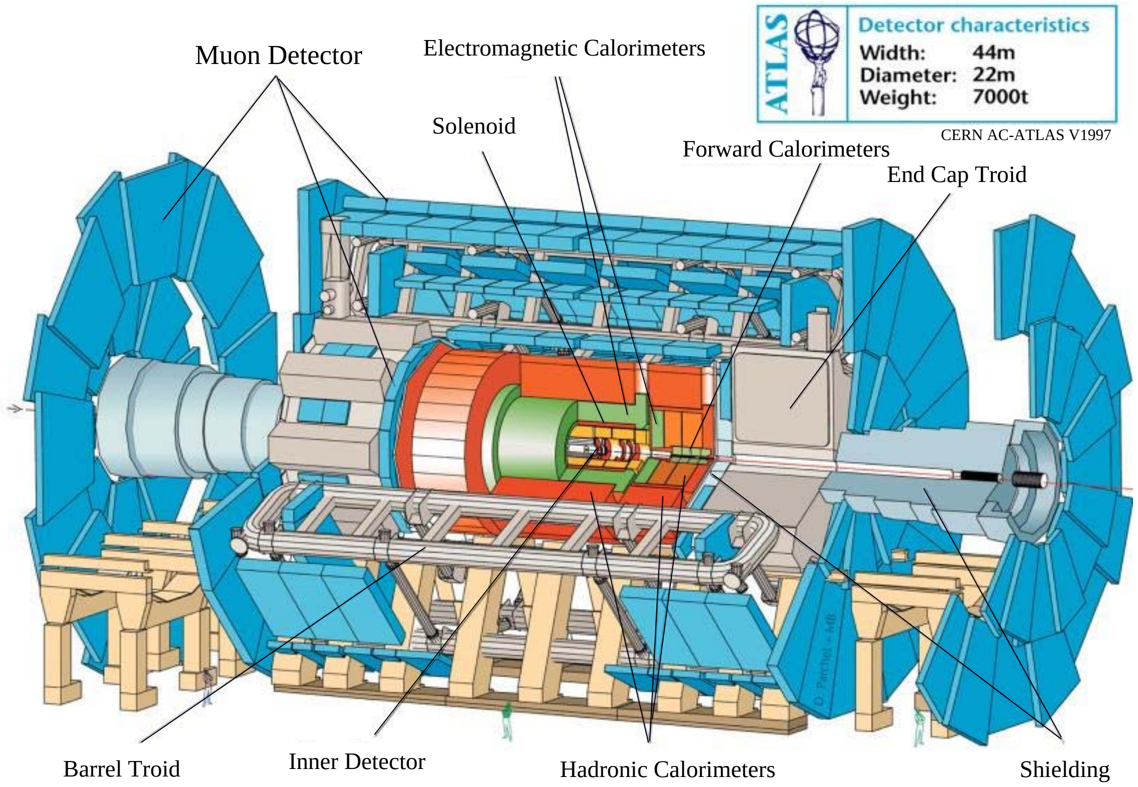

Fig. 3.3: ATLAS Detector[27]

For physics studies at the LHC, we need to know what kinds of particles are produced, by using combinations of various detectors. Particles' behavior in each detector is shown in Fig. 3.4. The produced particles can be distinguished by their differences of interaction with matters. For example, charged particles can be detected by a tracking detector and, by generating a magnetic field and detecting their trajectories there, their momenta can be measured. Particles with electric charge and photons can be detected by an electromagnetic calorimetry and electrons and photons can be identified there. Strongly interacting particles such as pions, neutrons and protons can be detected by a hadron calorimetry. Since muons deposit little energy in the calorimetry and have a long life time, they reach outside of the calorimetry and are detected by the muon spectrometer. Details of each detector are explained later.

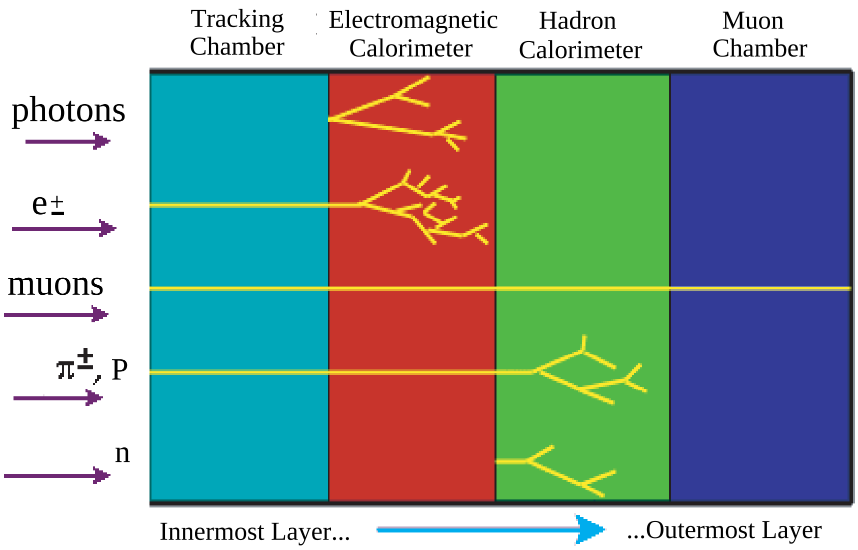

Fig. 3.4: Particles' behavior in each detector

For not only particle identification but also event selection, combined information from the detectors is very useful. For example, b quarks and c quarks can be identified by the following way. While t quarks immediately decay after its production, b hadrons and c hadrons have relatively long life time and fly for a moment. Then they decay far enough away from the primary vertex and make the secondary vertices. Therefore, b and c hadrons can be identified by finding the secondary vertices.

To exploit the full physics potential of the LHC, the ATLAS detector was designed to fulfill the following requirements;

- large acceptance and maximum angular coverage for hermetic jet and missing E_T calorimetry.
- very good electromagnetic calorimetry for electron and photon measurements;
- very good tracking efficiency for lepton-momentum measurements, secondary vertex findings and enhancement of the accuracy of electron and photon identification. Here, tracking in jets have to be done;
- stand-alone muon-momentum measurements at high luminosity;
- very low-p_T trigger and reconstruction capability at low luminosity.

Definition of coordinates

The coordinates are defined as follows. The beam line is defined as z-axis whose positive direction points in the direction of LHC-B. The plane transverse to the z-axis is defined as the x-y plane. The positive x-axis is pointing from the interaction point to the center of the LHC ring and the positive y-axis is pointing to upwards.

While the Cartesian coordinate system is defined, basically cylindrical coordinates are used because of the detectors being cylindrically symmetric. In this case, the z-axis is the same as for the Cartesian coordinate system. The azimuthal angle ϕ is defined as the angle from positive x-axis in x-y plane with the $-\pi$ to π range. The polar angle θ is also defined as the angle from the positive z-axis, and then, pseudorapidity η is defined as $\eta = -\ln\tan\frac{\theta}{2}$. For hadron colliders, η is often used because the particle distribution in pseudorapidity ($\frac{\Delta N}{\Delta\eta}$) is basically flat.

3.2.1 Inner Detector

The ATLAS Inner Detector is contained within a cylinder with a length of 7 m and a radius of 1.15 m, in a solenoidal magnetic field of 2 T. Momentum and vertex measurements are achieved with a combination of discrete high-resolution semiconductor pixel and strip detectors in the inner part of the tracking volume. Electron identification is performed by continuous straw-tube tracking detectors with transition radiation capability in the outer part. Overall inner detector layout is shown in Fig. 3.5 and details for each detector are mentioned below.

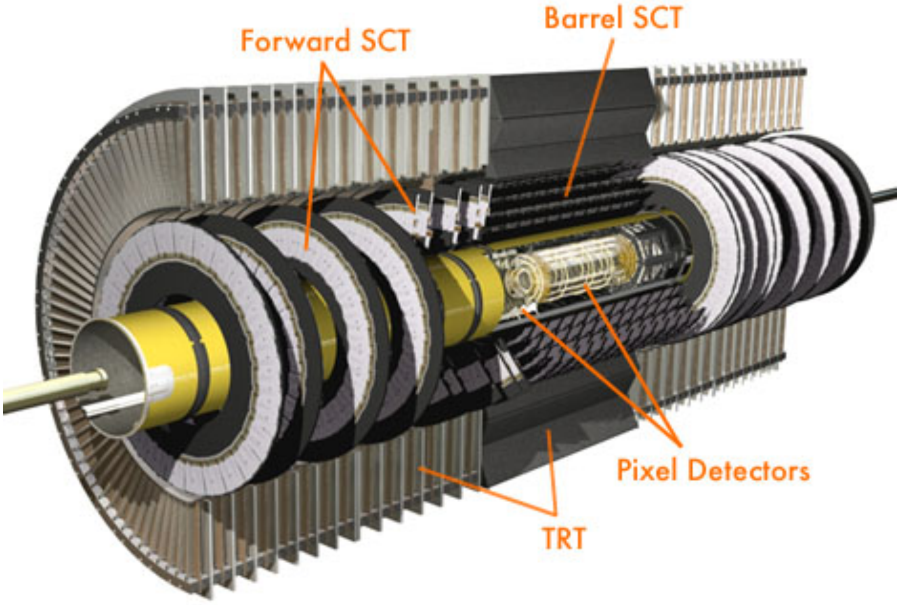

Fig. 3.5: 3D overall inner detector layout[27].

3.2.1.1 Silicon-pixel vertex-detector (Pixel)

ATLAS Pixel Detector provides a very high granularity and high precision set of measurements as close to the interaction point as possible. A Pixel sensor is a 16.4 × 60.8 mm^2 wafer of silicon with 46,080 pixels, 50 × 400 μm^2 each. Each sensor is read out by 16 chips, each serving for an array of 18 by 160 pixels. The 80 million pixels cover an area of 1.7 m^2. The system consists of three barrels at average radii of $\sim$ 5, 9 and 12 cm (1456 modules) respectively, and three discs on each side between radii of 9 and 15 cm (288 modules) as shown in Fig. 3.6. The modules are overlapped on the support structure to give hermetic coverage. The thickness of each layer is expected to be about 2.5 % of a radiation length at normal incidence. Typically three pixel layers are crossed by each track.

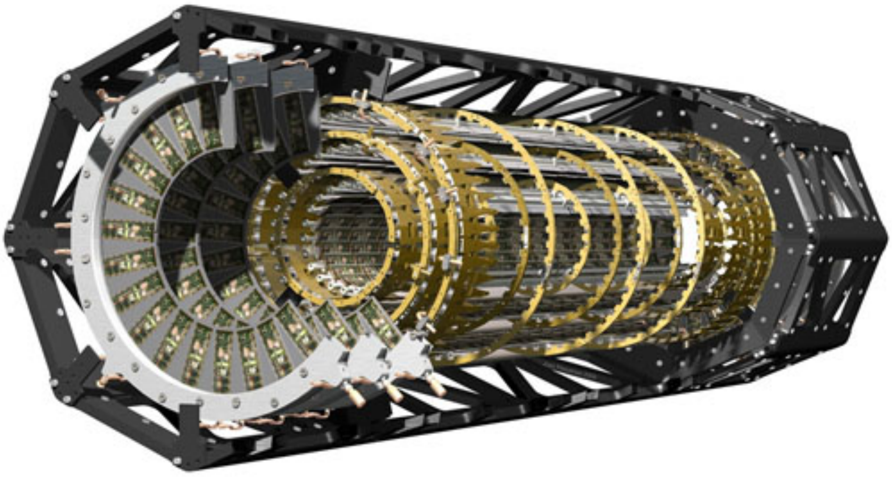

Fig. 3.6: Pixels Detector[27]

3.2.1.2 Semi Conductor Tracker (SCT)

The SCT system is designed to provide four precision measurements per track in the intermediate radial range, contributing to the measurement of momentum, impact parameter and vertex position, as well as providing good pattern recognition by the use of high granularity. The system is an order of magnitude larger in surface area than previous generations of silicon microstrip detectors, and, in addition, must face radiation levels which will alter the fundamental characteristics of the silicon wafers themselves.

Figure 3.7 shows 3D view of the SCT system, which covers $|\eta| < 2.5$. The barrel SCT uses four layers of silicon microstrip detectors to provide precision points in the r-ϕ and z coordinates. Each silicon detector is 6.36×6.40 cm^2 with 768 readout strips each with 80 μm pitch. Each module consists of four detectors. On each side of the module, two detectors are wire-bonded together to form 12.8 cm long strips. Two such detector pairs are then glued together back-to-back at a 40 mrad angle, separated by a heat transport plate, and the electronics is mounted above the detectors on a hybrid. The readout chain consists of a front-end amplifier and discriminator, followed by a binary pipeline which stores the hits above threshold until the first level trigger decision. The forward modules are very similar in construction but use tapered strips, with one set aligned radially. Forward modules are made with both $\sim$ 12 and 7 cm lengths. The detector contains 61 m^2 of silicon detectors with 6.2 million readout channels. The spatial resolution is 16 μm in r-ϕ and 580 μm in z. Tracks can be distinguished if separated by more than $\sim$200 μm.

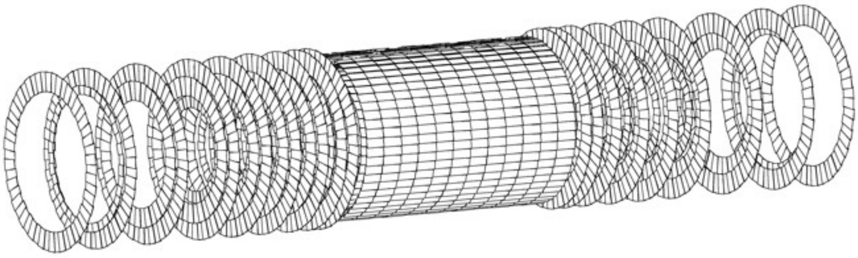

Fig. 3.7: SCT

3.2.1.3 Transition Radiation Tracker (TRT)

TRT is based on the use of straw detectors, or tubes, which can operate at the expected high rates due to their small diameter and the isolation of the sensitive wires within individual gas volumes. Electron identification capability is added by employing Xenon gas to detect transition radiation photons created in a radiator between the straws. The nonflammable gas mixture is Xe (70 %)/CO_2 (27 %)/O_2 (3 %) with a total volume. The barrel section is built of individual modules covering the radial range from 56 cm to 107 cm. Each end-cap consists of 18 wheels. Each channel provides a drift time measurement that gives a spatial resolution of 170 μm par straw.

3.2.2 Calorimeters

In contrast to other detectors, such as magnetic spectrometers, intrinsic resolution of calorimeters improves with energy, which makes themselves very suitable detectors at high-energy machines.

The task of the calorimeters at hadron colliders are the followings:

- accurate measurement of the energy and position of electrons and photons;
- measurement of the energy and direction of jets and measurement of the missing transverse energy (E_T) of the event;
- particle identification, for instance separation of electrons and photons from hadrons and jets, and of tau hadronic decays from jets;
- event selection at the trigger level.

The overall detector layout is shown in Fig. 3.8. Highly granular liquid-argon (LAr) electromagnetic sampling calorimetry, with an emphasis on energy and position resolution, covers the pseudorapidity range $|\eta| < 3.2$. At larger rapidities, higher radiation resistance is needed and the intrinsically-hard LAr technology is used. In the end-cap, the LAr technology is also used for the hadronic calorimeters. There are special LAr forward calorimeters which extend the pseudorapidity coverage to $|\eta| = 4.9$. The LAr calorimetry is contained in a cylinder with an outer radius of 2.25 m and extends longitudinally to ±6.65 m along the beam axis. The bulk of the hadronic calorimetry is provided by scintillator-tile calorimeter, which is separated into a large barrel and two smaller extended barrel cylinders, one on each side of the barrel. The outer radius of the scintillator-tile calorimeter is 4.25 m and its half length is 6.10 m. The overall calorimeter system provides good jet and missing E_T performance of the detector.

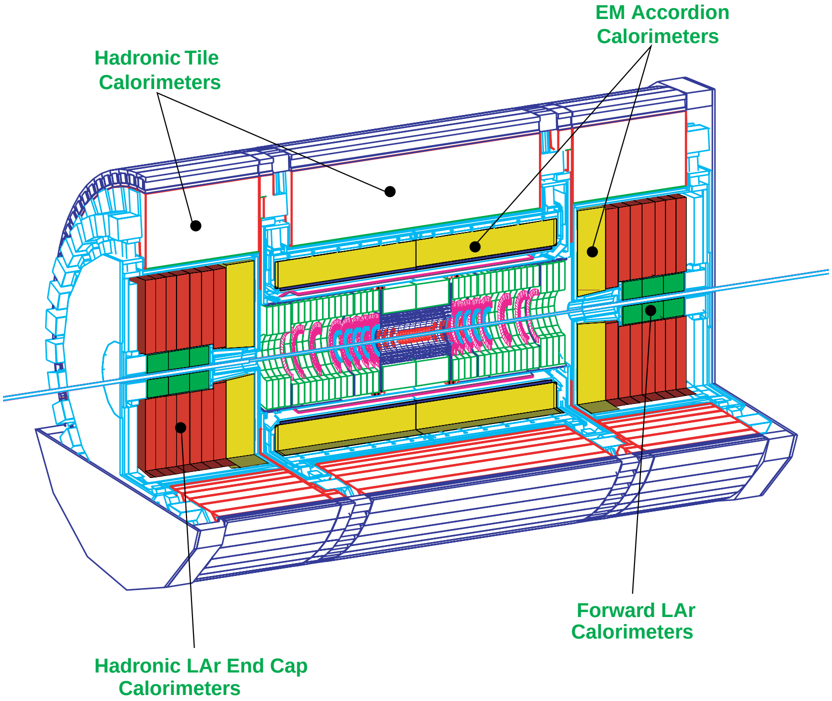

Fig. 3.8: 3D overall calorimeter layout[29].

3.2.2.1 Electromagnetic Calorimeter

The electromagnetic calorimeter is a sampling calorimeter which uses lead as absorber and liquid argon as sampling material. It covers the rapidity range up to $|\eta| < 3.2$. Its accordion geometry (shown in Fig. 3.9) provides a complete ϕ coverage without azimuthal cracks. The system is divided into a barrel ($|\eta| < 1.475$) and two end-caps ($1.375 < |\eta| < 3.2$). The barrel calorimeter consists of two identical half-barrels, separated by a small gap (6 mm) at $\eta = 0$. Each end-cap calorimeter is mechanically divided into two coaxial wheels: an outer wheel covering the region $1.375 < |\eta| < 2.5$ and an inner wheel covering the region $2.5 < |\eta| < 3.2$. The lead thickness in the absorber plates has been chosen as a function of rapidity as shown in Table 3.2, so as to optimize the calorimeter performance in terms of energy resolution. The LAr gap has a constant thickness of 2.1 mm in the barrel. In the end-cap, the shape of the Kapton electrodes and lead converter plates is more complicated, since the amplitude of the accordion waves increases with radius. The absorbers have constant thickness, and therefore the LAr gap also increases with radius. The total thickness of the electromagnetic calorimeter, which is shown in Fig. 3.10 as a function of η, is above 24 radiation lengths in the barrel and above 26 radiation lengths in the end-caps. The typically achieved energy resolution is:

$$\frac{\Delta E}{E} = \frac{11.5\%}{\sqrt{E}} \oplus 0.5\%, \tag{3.3}$$

and the resolution on the polar direction of a shower is:

$$\Delta\theta = \frac{50mrad}{\sqrt{E}}, \tag{3.4}$$

where E is represented in GeV.

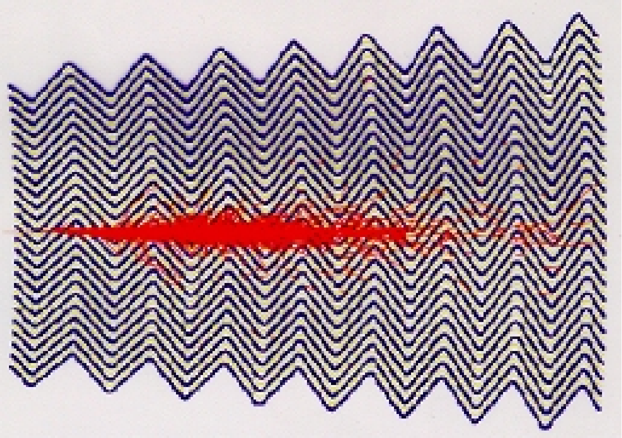

Fig. 3.9: Schematic view of the accordion shaped electrodes[27].

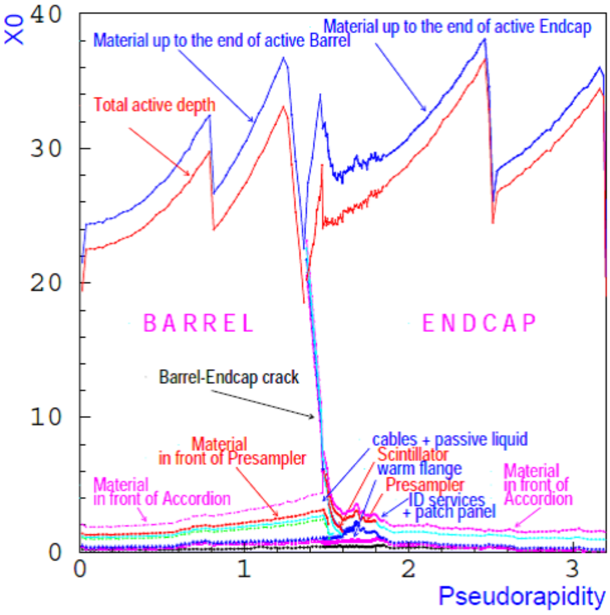

Fig. 3.10: Total thickness in radiation lengths of the ATLAS EM calorimeter as a function of η[30].

	η range	Pb thickness	Gap thickness
Barrel	$\|\eta\| < 0.8$	1.5 mm	2.1 mm
	$0.8 < \|\eta\| < 1.475$	1.1 mm	2.1 mm
End-cap	$1.375 < \|\eta\| < 2.5$	1.7 mm	2.8-0.9 mm
	$2.5 < \|\eta\| < 3.2$	2.2 mm	3.1-1.8 mm

Table 3.2: Lead thickness in the absorber plates and LAr gap thickness in the EM calorimeter as a funcfion of η.

3.2.2.2 Hadronic Calorimeter

The ATLAS hadronic calorimetry covers the range $|\eta| < 5$ using different techniques and devices as best suited for the different requirements and radiation environment. The system is divided into three sub detectors.

In the range $|\eta| < 1.6$, the iron-scintillating-tile technique (its schematic is illustrated in Fig. 3.11) is used for the barrel and extended barrel Tile calorimeters and, for partially instrumenting the crack between them, with the Intermediate Tile calorimeter. This gap provides space for cables and services from the innermost detectors. The tiles are placed perpendicular to the colliding beams and are staggered in depth, and the structure is periodic along z. The tiles are 3 mm thick and the total thickness of the iron plates in one period is 14 mm. Both sides of the scintillating tiles are read out by wavelength shifting (WLS) fibers into two separate Photo Multi Tubes (PMT). The resulting granularity of the detector is $\Delta\eta \times \Delta\phi = 0.1 \times 0.1$. It has a longitudinal segmentation of three samplings.

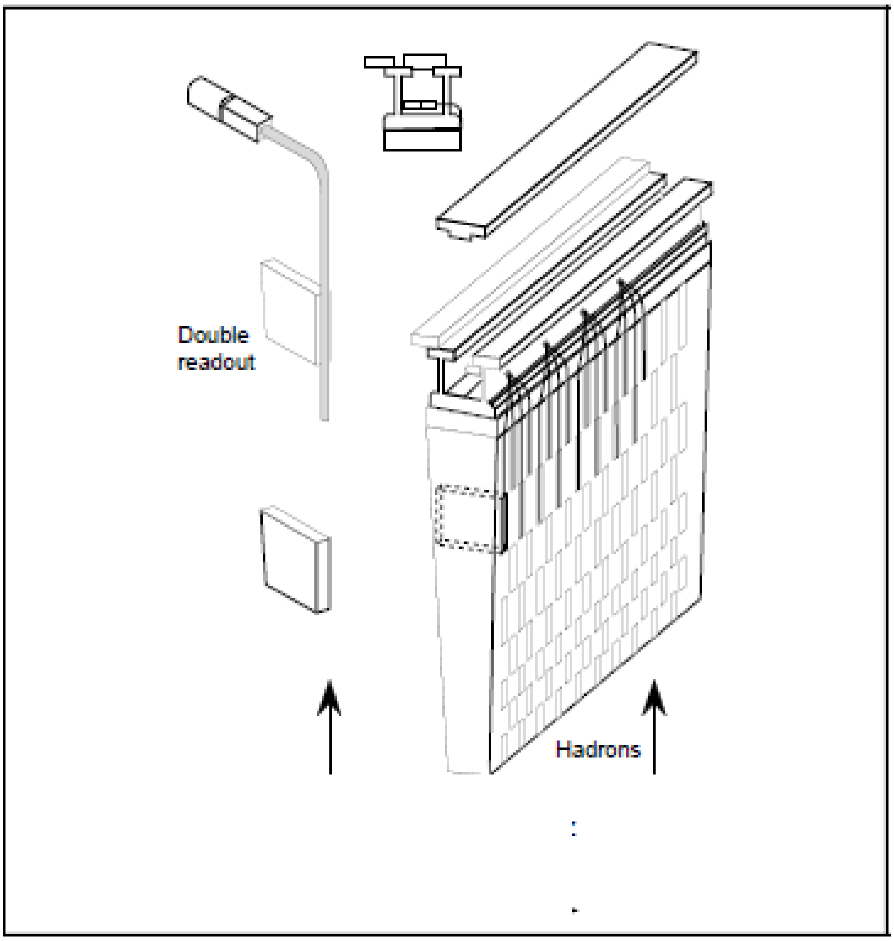

Fig. 3.11: A schematic of the Tile calorimeter[30].

In the range $1.5 < |\eta| < 4.9$, the LAr calorimetry takes over: the end-cap hadronic calorimeter extends to $|\eta| < 3.2$, while the range $3.1 < |\eta| < 4.9$ is covered by the high-density forward calorimeter. Each hadronic end-cap calorimeter consists of two, equal diameter, independent wheels. The first wheel is built out of 25 mm copper plates, while the second one use 50 mm plates. The end-cap hadronic calorimeter has a $\Delta\eta \times \Delta\phi = 0.1 \times 0.1$ segmentation in the range up to $|\eta| < 2.5$ and a segmentation of $\Delta\eta \times \Delta\phi = 0.2 \times 0.2$ in the range up to $2.5 < |\eta| < 3.2$. The forward calorimeter consists of three sections. The first is made out of copper, while the others are made out of tungsten. In each of them, the calorimeter consists of a metal matrix with regularly spaced longitudinal channels filled with rods. The sensitive medium is LAr which fills the gap between the rod and the matrix. Both the hadronic end-cap and forward calorimeters are integrated in the same cryostat housing also the electromagnetic end-cap calorimeters.

The total thickness is 11 interaction lengths at $\eta = 0$, including 1.5 interaction lengths of the outer support. It is sufficient to reduce the punch-through below the irreducible level of prompt or decay muons. Thickness of active calorimeter being close to 10 interaction lengths is also adequate to provide good performance on resolution for high energy jets. Over the full η range, four longitudinal samples are available. The average jet energy resolution is:

$$\frac{\Delta E}{E} = \frac{50\%}{\sqrt{E}} \oplus 3\%, \tag{3.5}$$

where E is represented in GeV.

3.2.3 Muon Spectrometer

While muons interact weakly and electromagnetically like electrons, they can reach outside of the calorimeter because the muon mass is about 200 times heavier than the electron mass. Therefore, the muon spectrometer is placed at the outermost of the detectors.

High-momentum final-state muons are one of the most promising and robust signatures of physics at the LHC. To exploit this potential, the ATLAS is equipped with a high-resolution muon spectrometer with stand-alone triggering and momentum measurement capability over a wide range of transverse momentum (p_T), pseudorapidity (η) and azimuthal angle (ϕ). Muon measurement at ATLAS is based on the magnetic deflection measurement of muon tracks in a system of the large superconducting air-core toroids instrumented with tracking chambers. Figure 3.12 shows the 3D overall layout of the muon spectrometer and Figure 3.13 is the sectional view of a quarter of the system. There can be seen four detectors, two of them, Thin Gap Chambers (TGC) and Resistive Plate Chambers (RPC) are trigger chambers and the others, Monitored Drift Tube chambers (MDT) and Cathode Strip Chambers (CSC) are for precision measurement. In the range $|\eta| < 1.0$, bending fields are provided by a large barrel magnet consisting of eight coils surrounding the hadron calorimeter. For $1.4 < |\eta| < 2.7$, muon tracks are bent in two smaller end-cap magnets inserted into both ends of the barrel toroid. In the interval $1.0 < |\eta| < 1.4$, magnetic deflection is provided by a combination of barrel and end-cap fields. This magnet configuration provides a field that is mostly orthogonal to the muon trajectories, while minimizing the degradation of resolution due to multiple scattering.

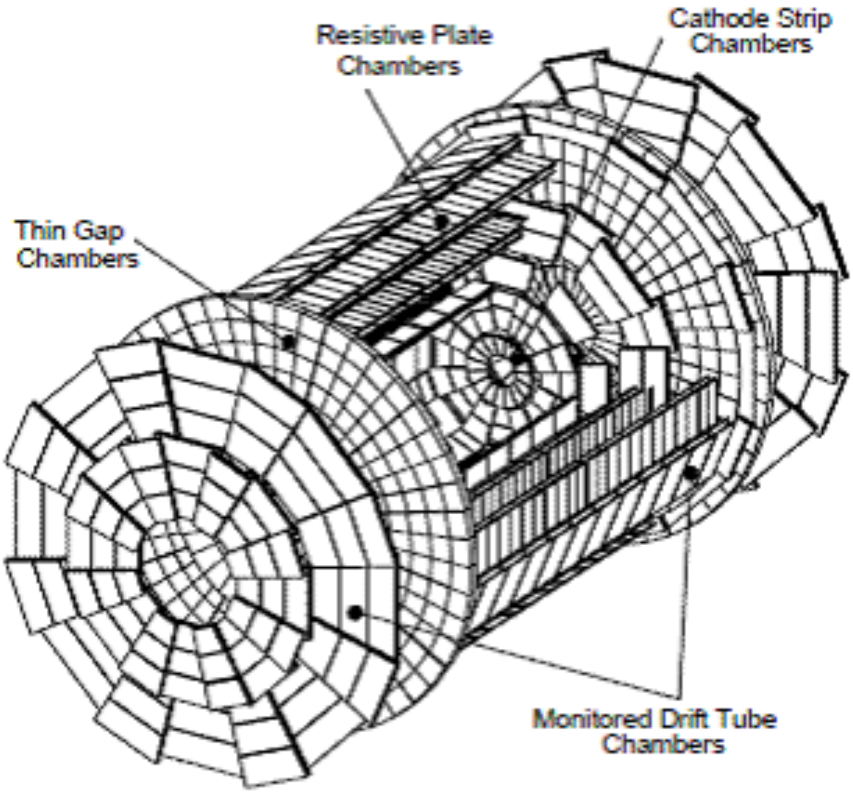

Fig. 3.12: 3D muon spectrometer layout[31].

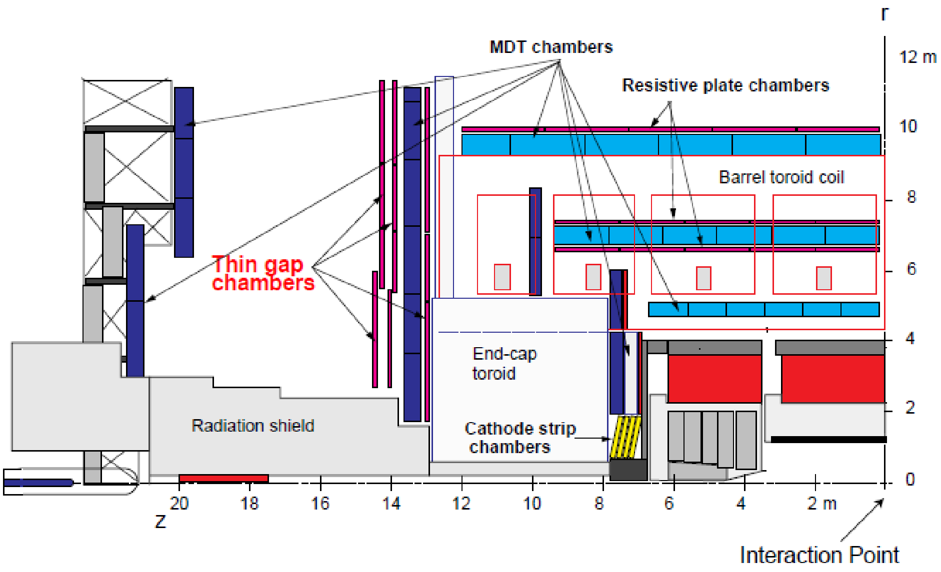

Fig. 3.13: A sectional plan of the muon spectrometer layout[31].

3.2.3.1 Physics requirements

While high-p_T muons are expected to be produced from the new particle production, physics of CP violation through B-meson decays can be studied by requiring low-p_T muons. Therefore, performance of the spectrometer should be optimized on the basis of selected benchmark processes like above. Important parameters to be optimized for maximum physics reach are:

- Resolution: momentum and mass resolutions at the level of 1 % should be achieved for muons with $p_T >\sim$ 6GeV against high background levels;
- Second-coordinate measurement: a measurement of muon tracks in the non-bending projections with a spatial resolution of about 1cm is required for the track reconstruction and reliable momentum determination;
- Rapidity coverage of track reconstruction: all physics channels need a pseudo-rapidity coverage up to $|\eta| \sim 3$ and good hermeticity, in particular rare high-mass processes;
- Trigger selectivity: a transverse momentum threshold of around 20 GeV is adequate for high-mass states, which is focused on physics at the LHC at nominal luminosity. Lower thresholds of 6 GeV are also required for CP violation in the B sector;
- Trigger coverage: adequate trigger efficiencies can be obtained with η coverage smaller than that of the precision chambers. The actual requirements are mostly determined by processes at opposite ends of the LHC mass scale: the need for good acceptance for rare high-mass Higgs particles, and the need for very high statistics to study small rate asymmetries due to CP violation in the B sector. Trigger coverage of $|\eta| < 2.4$ is found to be sufficient;
- Bunch-crossing identification: the LHC bunch-crossing interval of 25 ns sets the scale for the required time resolution of the first-level trigger system;

3.2.3.2 Magnet system

The magnet system consists of three air-core superconducting toroids designed to produce a large-volume magnetic field covering the rapidity range $0 < |\eta| < 2.7$, with an open structure that minimizes the contribution of multiple scattering to the momentum resolution. Geometry of the magnet is shown in Fig. 3.14. The barrel toroid extends over a length of 25 m, with an inner bore of 9.4 m and an outer diameter of 20.1 m. The two end-cap toroids are inserted in the barrel at each end. They have a length of 5.0 m, an inner bore of 1.65 m and an outer diameter of 10.7 m. Each toroid consists of eight flat coils assembled radially and symmetrically around the beam axis. The end-cap toroid coils are rotated in azimuth by an angle of 22.5 degree with respect to the barrel toroid coils to provide for radial overlap, and to optimize the bending power in the transition region between the two toroids. The barrel toroid coils are contained in individual cryostats and are held rigidly together by means of eight rings of voussoirs and struts that contain the gravitational and magnetic forces. The eight coils of each end-cap toroid are assembled in a single large cryostat. The magnetic field provides for typical bending powers of 3 Tm in the barrel and 6 Tm in the end-cap regions. Owing to the finite number of coils, the field configuration is not perfectly toroidal and presents a regularly rippled profile (see Fig. 3.15). These effects are most visible in the transition region between the barrel toroids and the end-cap toroids, where there exist significant radial field components, as well as small regions with degraded momentum resolution. The bending power is shown in Fig. 3.16.

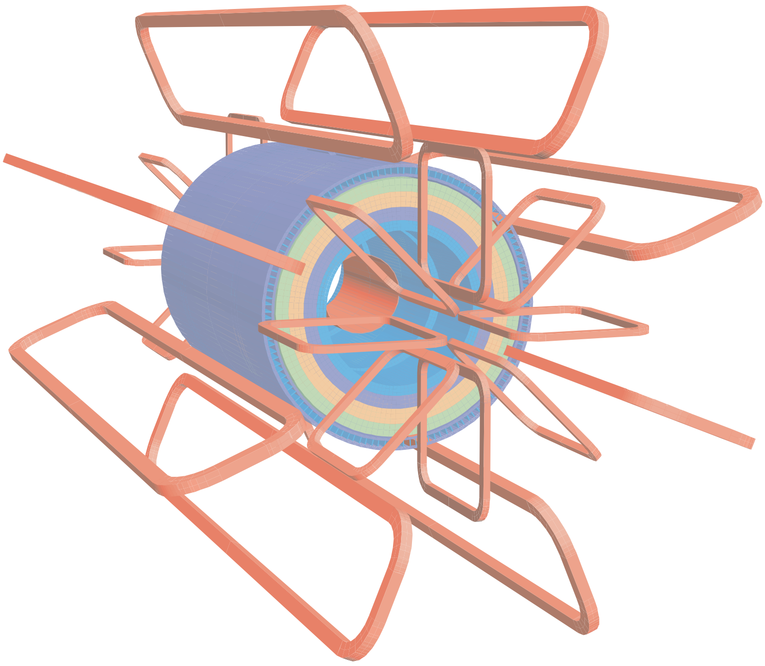

Fig. 3.14: Geometry of the toroid magnet[29].

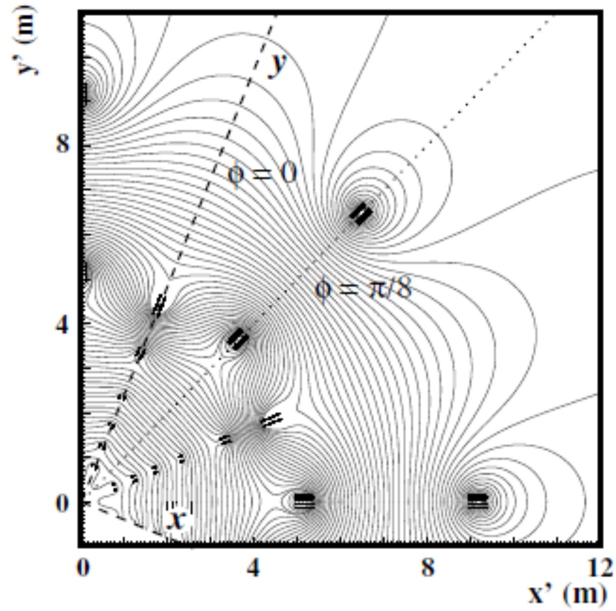

Fig. 3.15: Magnetic field map in the transition region between the barrel and the end-cap. The field lines in the transverse plane are shown. The coordinate system of the magnetic field is rotated by $\frac{\pi}{8}$ with respect to the ATLAS coordinate system[31].

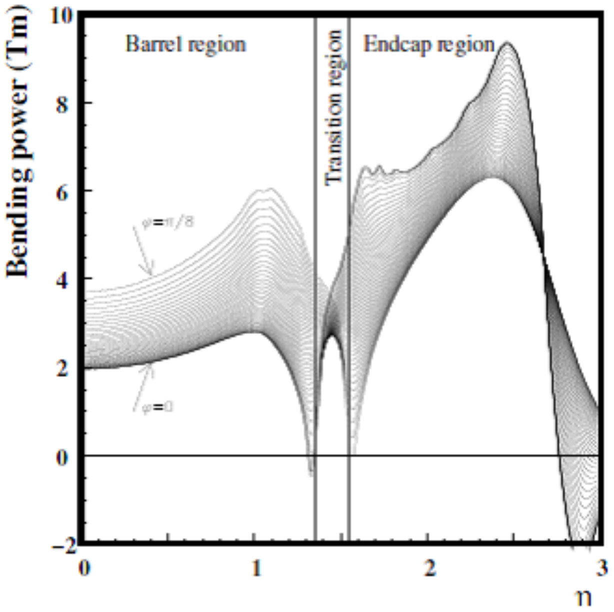

Fig. 3.16: Toroid bending power $\int Bdl$ of the azimuthal field component, integrated between the inner and outer muon station as a function of η[31].

3.2.3.3 Momentum measurement

The momenta of charged particles can be calculated by detecting their trajectories in the magnetic field. Assuming that a track is detected at three equally-spaced points, the sagitta s of the circular orbit is defined as shown in Fig. 3.17 and calculated as

$$s = R(1 - \cos\frac{\alpha}{2}) \sim \frac{R\alpha^2}{8} (\alpha << 1). \tag{3.6}$$

At the same time, the momentum P of a charged particle in magnetic field B [T] is calculated as

$$P = 0.3BR, \tag{3.7}$$

where R [m] is the measured radius of the orbit. Then, concerning α to be

$$\alpha = 0.3\frac{BL}{P}, \tag{3.8}$$

the sagitta is represented as

$$s = 0.3\frac{BL^2}{8P}. \tag{3.9}$$

Thus, the momentum can be obtained from the sagitta.

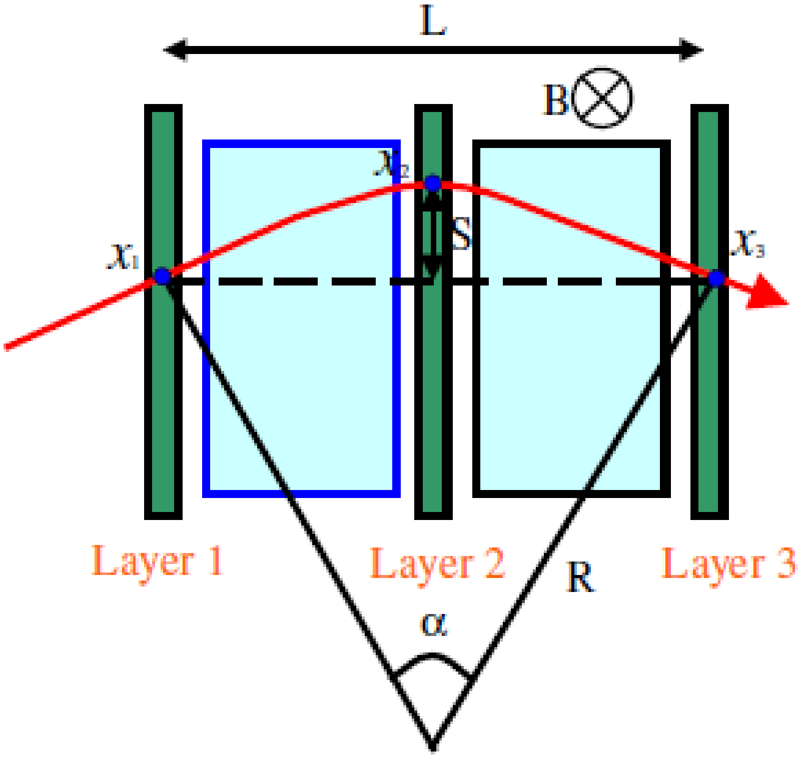

Fig. 3.17: Measurement of sagitta.

3.2.3.4 Muon precision chambers

Monitored Drift Tubes (MDT) cover 99.5 % of the area and Cathode Strip Chambers (CSC) cover the remaining forward area near the beam pipe where particle fluxes are high. Although this area is physically small, it covers a large range in pseudorapidity ($2 < |\eta| < 2.7$). The precision chambers measure the track coordinates in the bending plane with high precision. For the MDTs, no information on the non-bending coordinate exists. The CSCs, however, do measure both quantities.

MDT (Monitored Drift Tube)

The Monitored Drift Tube Chambers perform the precision coordinate measurement in the bending direction of the air-core toroidal magnet and provide the muon momentum measurement. They cover enough area needed for a good momentum determination of the muons with $|\eta| < 2.7$.

The basic detection element is a cylindrical aluminum drift tube of 30 mm diameter and a Tungsten-Rhenium central wire of 50 μm diameter. It is operated with nonflammable gas composed of Ar(93 %) and CO_2(7 %) at 3 bar absolute pressure for reduced diffusion and ionization fluctuation. The wire is at a potential of 3080 V. These operating conditions are optimum with regard to the requirements of linearity in the drift space time relation, a small occupation time (about 700 ns maximum drift time) and a small Lorentz angle of $\sim$9.3 degree. The amplification factor is set to be very low, 2×10^4, to minimize the aging effect.

The operating parameters are summarized in Table 3.3. The relation between the drift time and the drift distance is shown in Fig. 3.18 without a magnetic field. In the magnetic field the wires are oriented essentially parallel to the field lines. The magnetic effect on the drift distance-drift time (r-t) relation gives a small deviation away from the radial drift (see Fig. 3.19) and a small reduction of the apparent drift velocity. The size of the equivalent coordinate shift depends on the gas and the fields.

The precise r-t relation is obtained by fitting tracks to the six measured drift times of a chamber in an 'auto calibration' procedure on the basis of the staggered wire arrangement. Corrections to the coordinates of an individual tube are applied beforehand. The drift signal is processed with a current-sensitive amplifier followed by a shaper and a discriminator set at a threshold which corresponds to the 20th electron when the avalanche amplification is 2×10^4. With these parameters the average single tube resolution is 80 μm.

A Monitored Drift Tube Chamber is an assembly of six parallel layers of drift tubes on a support frame, and three layers on each side, see Fig. 3.20. The tubes with their diameter of 30 mm are closely spaced so that each 'triple layer' or 'multilayer' has a thickness of about 82 mm. By registering the drift times of the ionized electrons in the gas, one determines six coordinates of a typical track in the plane of the layer and in the direction across the tubes. This results in a measurement of effectively one coordinate with 40 μm precision and one angle with 3×10^{-4} precision.

To obtain such precision with a light weight construction, the chambers are assembled on their support or spacer frame using precision mechanics during production. Their deformations are monitored by built-in optical systems once they have left the flat granite table on which they have been assembled. This explains the 'Monitored' of the MDTs.

The physical reference for the coordinate measurement is the wire position. It is determined by the two anchor points and by the gravitational sag of the wire in the presence of an electric field. For a determination of the momentum of a muon track in the spectrometer magnet, the sagitta, explained above, is used with the measured track coordinates of typically three MDT chambers. This requires the relative chamber positions to be known with a precision better than the achievable measurement accuracy of one chamber. The achievable accuracy is to be 30 μm, which gives significant contribution to the precision at very high-p_T. The stand-alone muon momentum resolution of the spectrometer is shown in Fig. 3.21 for the barrel part, and in Fig. 3.22 for the end-cap part. The different contributions to the resolution are indicated: multiple scattering, relative chamber alignment uncertainties, the drift tube measurement uncertainty, as well as the energy loss fluctuations in the calorimeter.

Parameter	Value
Tube material	Al
Outer tube diameter	29.970 mm
Tube wall thickness	0.4 mm
Wire material	gold-plated W (97 %)/Re (3 %)
Wire diameter	50 μm
Gas mixture	Ar (93 %)/CO_2 (7 %)
Gas gain	2×10^4
Wire potential	3080 V
Maximum drift time	~700 ns
Average drift velocity	30 μm/ns
Effective threshold	20th electron
Average resolution per tube	~80 μm

Table 3.3: Summary of the operating parameters of MDT chambers[32].

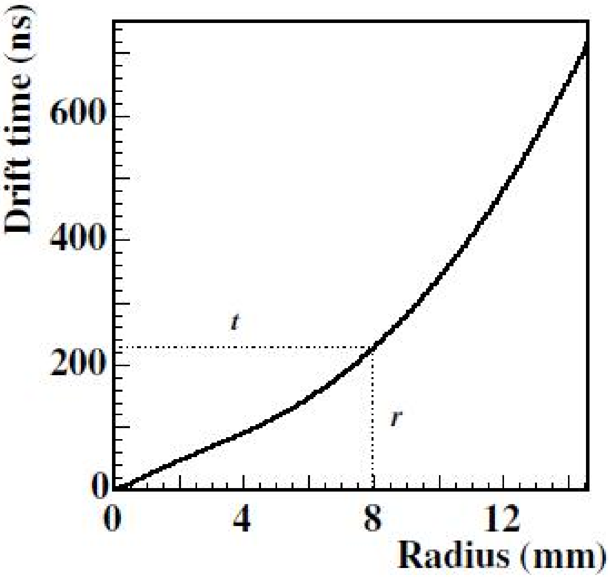

Fig. 3.18: Relation between measured drift time and corresponding drift length in the absence of a magnetic field [29].

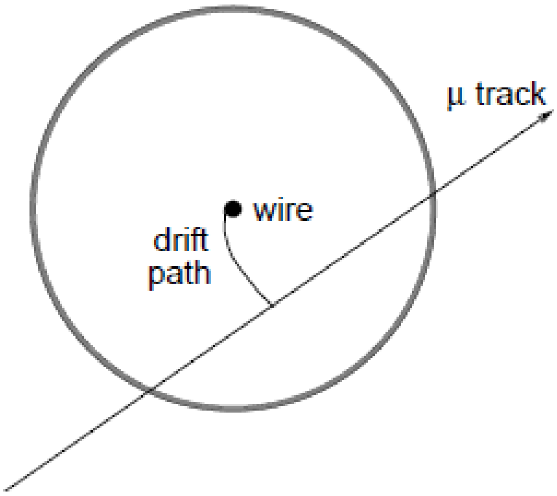

Fig. 3.19: Drift tube operation in a magnetic field with curved drift pass[29].

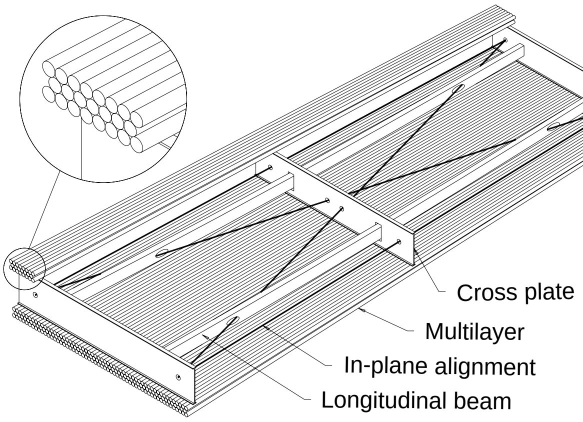

Fig. 3.20: Schematic view of the MDT chamber[29].

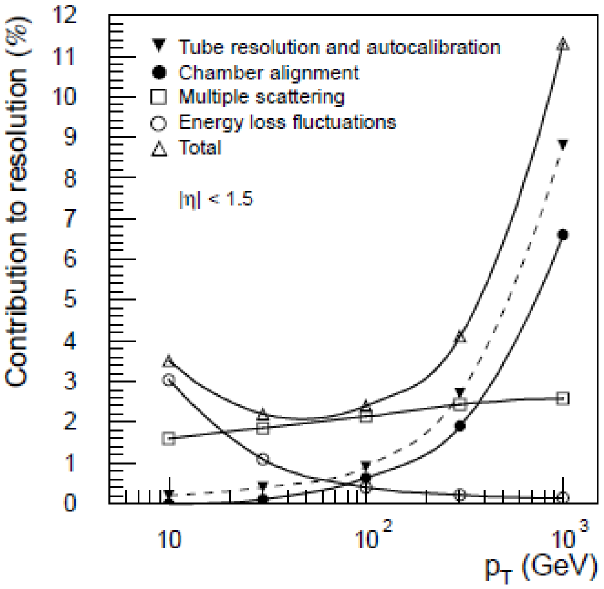

Fig. 3.21: $\Delta p_T/p_T$ as a function of p_T for muons reconstructed in the barrel region $\eta < 1.5$[29].

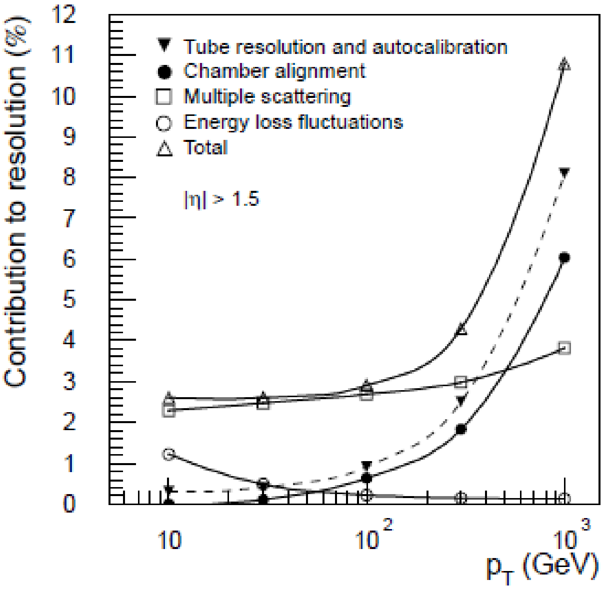

Fig. 3.22: $\Delta p_T/p_T$ as a function of p_T for muons reconstructed in the end-cap region $\eta > 1.5$[29].

CSC (Cathode Strip Chamber)

MDTs well satisfy the requirements for the precision measurement of muons in ATLAS. However, their relatively large diameter and high operating pressure make themselves unsuitable for use in areas where high (> 200 Hz/cm^2) counting rates are expected. Such high background rates are encountered in the first muon measuring station at $|\eta| > 2.0$. In this region, CSCs are used and covering up to $|\eta| < 2.7$. Their operation is considered safe up to counting rates of about 1000 Hz/cm^2. They are multiwire proportional chambers with a cathode strip readout providing the required spatial resolution of ~ 60 μm by charge interpolation, . The schematic view of CSC is shown in Fig. 3.23 and the basic characteristics of the CSCs are summarized below:

- Excellent single layer track resolution; a sigma of ~ 60 μm has been measured;

- Good two-track resolution; nominal single-track resolution is achieved for each of a pair of tracks separated in the bend direction by more than 5 mm corresponding to one-strip width;
- Electron drift time less than 40 ns resulting in a time resolution of 7 ns. By detecting the earliest arrival from four or more of the eight layers, the resolutions of 3.5 ns have been measured in a test beam providing a fully efficient bunch-crossing identification;
- Low neutron sensitivity; because of the small gas volume and the absence of hydrogen in the operating gas (Ar (80 %)/CO_2 (20 %) mixture), the measured neutron sensitivity is less than 10^{-4}. The sensitivity to photons was also measured and found to be of the order of 1 %.
- The transverse coordinate is derived by reading orthogonal strips on the second cathode of the chamber.

The operating parameters of the CSC are shown in Table 3.4.

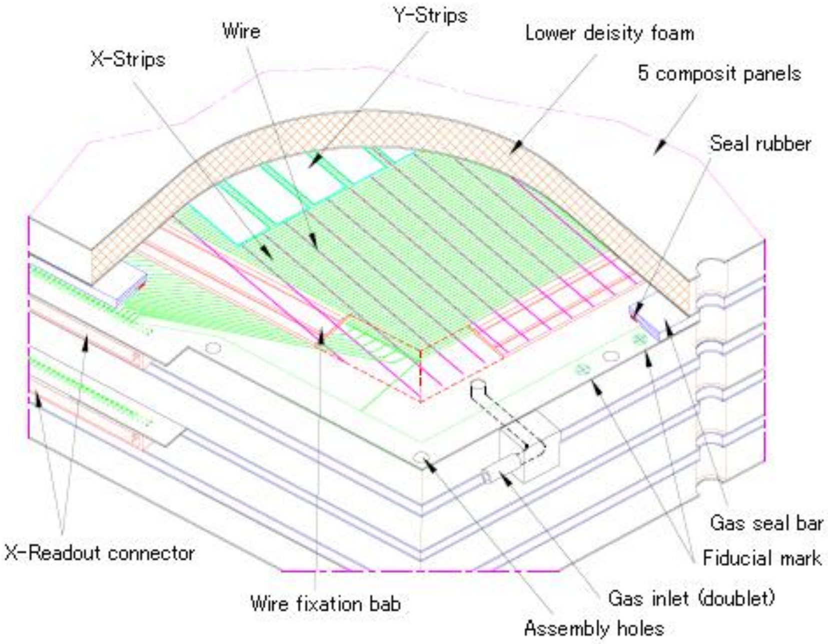

Fig. 3.23: Schematic view of CSC[32].

Parameter	Value
Operating voltage	1900 V
Anode wire diameter	30 μm
Gas gain	6×10^4
Gas mixture	Ar (80 %)/CO_2 (20 %)
Total ionization	90 ion pairs

Table 3.4: Summary of the operating parameters of the CSC[32].

3.2.3.5 Muon trigger chambers

Because of the high background rates at the LHC, the muon drift chambers will have to operate at high levels of occupancy. For this reason, it was decided to use an dedicated, fast and hence low-occupancy chamber system for the trigger purpose.

The main tasks required to the ATLAS muon trigger system are:

- coarse measurement of and discrimination on the muon transverse momentum;
- bunch crossing identification;
- fast and coarse tracking to identify the hits of the precision chambers that are related to the detected muon track at the level-1 trigger;
- second-coordinate measurement with a required resolution of 5∼10 mm.

Resistive Plate Chambers (RPC) are used for the barrel region and Thin Gap Chambers (TGC) are used for the end-cap region. They are covering the spectrometer acceptance up to $|\eta| \sim 2.4$. Both types of chambers generate fast signals with a time resolution of a few ns and are used for the level-1 trigger where bunch crossing identification is needed. A spatial resolution of a few mm is adequate for these chambers. It is also used in the pattern recognition algorithm and provides the only measurement of the track coordinate in the non-bending plane.

TGC (Thin Gap Chamber)

Thin Gap Chambers operating in a saturated mode have a structure similar to Multi-Wire Proportional Chambers (MWPC), except that the anode-to-anode, i.e. wire-to-wire, distance is larger than the cathode-to-anode distance (see Fig. 3.24 and 3.25). With the use of a highly quenching gas mixture of CO_2 (55 %) and n-C_5H_{12} (45 %), this type of cell geometry allows operation in saturated mode. The mode has an advantage of small sensitivity to mechanical deformations, which is important for large detectors. Furthermore, operating in saturated mode leads to other beneficial properties of TGCs, for example:

- small parallax: the signal obtained by the passage of a minimum-ionizing particle has only a small dependence on the incident angle up to 40 degree.
- small Landau tails: less than two of the pulse-height distribution for a minimum-ionizing particle is contained in the tails (amplitudes more than 2σ above the mean of a Gaussian fit) of the pulse-height distribution.

The high electric field around the TGC wires (see Fig. 3.25) and the small distance between wires strongly reduce the drift component of ionization clusters, leading to very good time resolution. Figure 3.24 shows a crosssection of a TGC triplet and of a doublet. The basic structure consists of 50 μm wires spaced every 1.8 mm. The anode plane is sandwiched between two graphite cathode planes at a distance of 1.4 mm. The cathode plane consists of a 1.6 mm FR4 plate on which the graphite is deposited. Behind the interior cathode plane, etched copper strips provide the readout of the azimuthal coordinate. In order to prevent the wire from sagging and to keep the anode-cathode distance constant, two types of the mechanical support parts are used; called "wire-support" and "button support". Each support part is intrinsically inefficient. On the outside, 1.6 mm FR4 plates with copper cladding, which provide the outside ground, are covered with a 5 mm thick low-cost paper honeycomb, to provide the needed protection from gas over-pressure. The outer honeycomb is covered by 500 μm of FR4. In the interior the two 1.6 mm FR4 plates are separated by a 20 mm thick paper honeycomb. The operating parameters are summarized in Table 3.5. Note that the triplet has three wire-planes, but only two strip-planes.

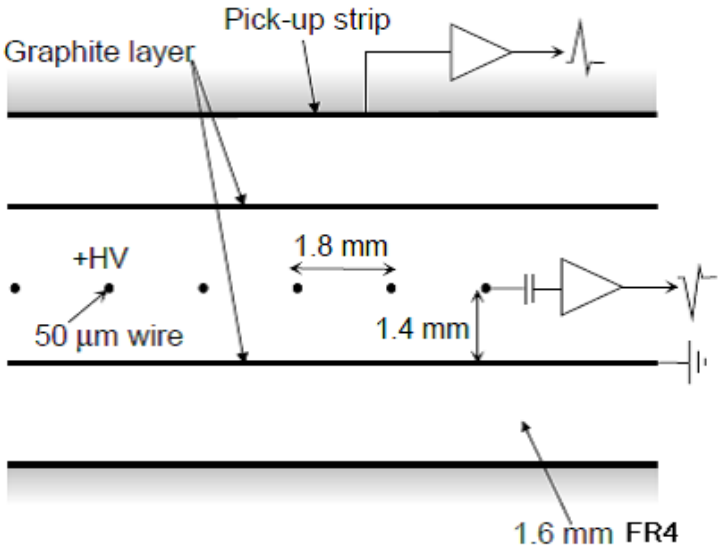

Fig. 3.24: TGC structure[29].

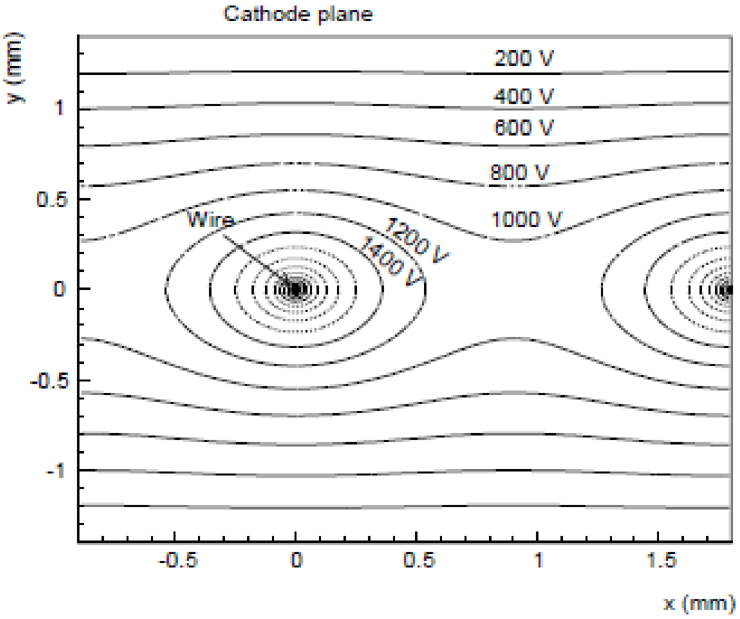

Fig. 3.25: Equipotential lines in TGCs[29].

Parameter	Value
Gas gap	2.8±0.10 mm
Wire pitch	1.8±0.05 mm
Wire diameter	50 μm
Wire potential	2900±100 V
Operating plateau	200 V
Gas mixture	CO_2 (55 %)/n-C_5H_{12} (45 %)
Gas amplification	3×10^5

Table 3.5: Summary of the operating parameters of the TGC[32].

There are three stations with seven layers in the middle station around z∼15 m. Each station is called "M1", "M2" or "M3" from the inner side, respectively. The layers are arranged in one triplet (M1 station) and two doublets (M2 and M3 station). These three stations are mainly used for the muon trigger. There are another station in the inner station around z∼8 m. There is a station with two layers arranged in one doublet. The layout geometry, chamber overlapping and channel wiring have been arranged so that there are, to first order, no overlaps and no holes in this plane. (Where wire-groups or strips do overlap, only one is read out.) The farthest plane from the interaction point is referred to as the "pivot" plane. Tracks passing through this plane can be given a unique η-ϕ coordinate. Because any track segment in the other planes must be in coincidence with this plane, double counting can be avoided in the level-1 trigger. The level-1 trigger looks for tracks in a cone opening backwards from the pivot plane (details in chapter 4).

RPC (Resistive Plate Chamber)

RPC is a gaseous detector providing a typical space-time resolution of 1 cm and 1 ns with digital readout. The basic RPC unit is a narrow gas gap formed by two parallel resistive Bakelite plates, separated by insulating spacers. The primary ionization electrons are multiplied into avalanches by a high, uniform electric field of typically 4.9 kV/mm. Amplification in avalanche mode produces pulses of typically ∼ 1 pC. RPCs will be operated with a gas mixture of $C_2H_2F_4$ (94.7 %)/Iso-C_4H_{10} (5 %)/SF_6 (0.3 %), a non-flammable gas that allows for a relatively low operating voltage. The signal is read out via capacitive coupling by metal strips on both sides of the detector. A trigger chamber is made from two rectangular detector layers, each one is read out by two orthogonal series of pick-up strips. The one is the 'η strips' parallel to the MDT wires and provide the bending view of the trigger detector. The other is the 'ϕ strips' orthogonal to the MDT wires and provide the second-coordinate measurement also required for the offline pattern recognition.

The RPC has a simple mechanical structure, using no wires and, are therefore simple to manufacture. The 2 mm-thick plastic laminates are separated by a series of insulating spacers of 2 mm thickness, which define the size of the gas gap. The spacers are glued on both plates at 10 cm intervals. A 7 mm wide frame of the same material and thickness as the spacers is used to seal the gas gap at all four edges. The mechanical structure of an RPC is shown in Fig. 3.26. The outside surfaces of the resistive plates are coated with thin layers of graphite paint, which are connected to the high voltage supply. These graphite electrodes are separated from the pick-up strips by 190 μm thick PET films glued on both graphite surfaces. The readout strips are arranged with a pitch varying from 28 to 38 mm. Each chamber is made from two detector layers and four readout strip panels. These elements are rigidly held together by two support panels which provide the required mechanical stiffness of the chambers. The panels are made of light-weight paper honeycomb (40 kg/m^3) sandwiched between two copper sheets. One panel is flat, 50 mm thick, with 0.5 mm thick aluminum coatings. The other panel is 10 mm thick with 0.3 mm coatings and is preloaded with a 1 cm sagitta. The two panels are rigidly connected by 2 mm thick aluminum profiles, such that the preloaded support panel provides uniform pressure over the whole surface of an RPC module. The principal RPC parameters are summarized in Table 3.6. To preserve the good intrinsic time resolution of RPCs, the readout strips are optimized for good transmission properties and are terminated at both ends to avoid signal reflections. The front-end electronics are based on a three-stage voltage amplifier followed by a variable-threshold comparator. The amplifier frequency response is optimized for the typical time structure of RPC avalanches.

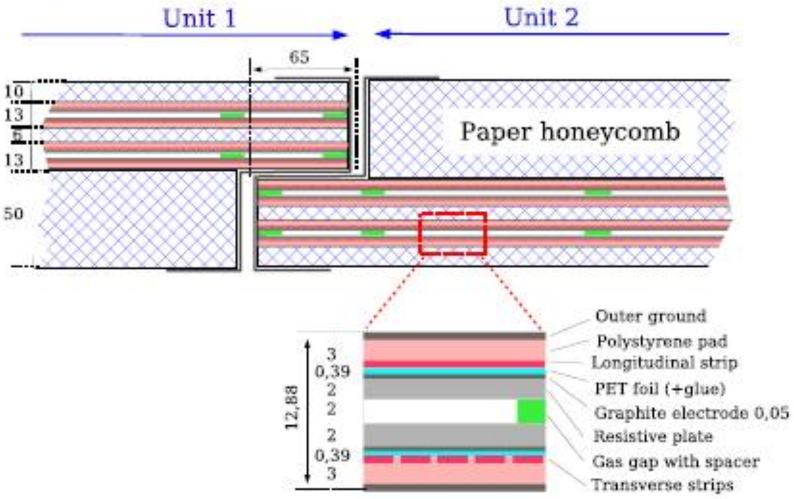

Fig. 3.26: RPC structure[32].

Parameter	Value
E-field in gap	4.9 kV/mm
Gas gap	2 mm
Gas mixture	$C_2H_2F_4$ (94.7 %)/Iso-C_4H_{10} (5 %)/SF_6 (0.3 %)
Readout pitch of η and ϕ strips	23–35 mm
Detection efficiency per layer	$\geq$98.5 %
Efficiency including spacers and frames	$\geq$97 %
Intrinsic time jitter	$\leq$1.5 ns
Jitter including strip propagation time	$\leq$10 ns
Local rate capability	$\sim$1 kHz/cm^2
Streamer probability	$\leq$1 %

Table 3.6: Summary of the operating parameters of the RPC[32].

The middle plane is called the pivot plane, where the level-1 trigger procedure starts. Details are mentioned in chapter 4.

4 Trigger and data-acquisition system at ATLAS

The ATLAS trigger and data-acquisition (DAQ) system is based on three levels of online event selection. Each trigger level refines the decisions made at the previous level and, where necessary, applies additional selection criteria. Starting from initial bunch-crossing rate of 40 MHz (interaction rate of $\sim 10^9$ Hz at a luminosity of $10^{34}\mathrm{cm}^{-2}\mathrm{s}^{-1}$), the rate of selected events must be reduced to ~200 Hz for permanent storage. While this requires an overall rejection factor of 10^7 against so-called minimum-bias events, very good efficiencies must be retained for the rare new physics processes, such as Higgs boson decays.

4.1 Overview of the system

Figure 4.1 shows a simplified functional view of the Trigger/DAQ system. In the following, a brief description is given for some of the key aspects in the event-selection process.

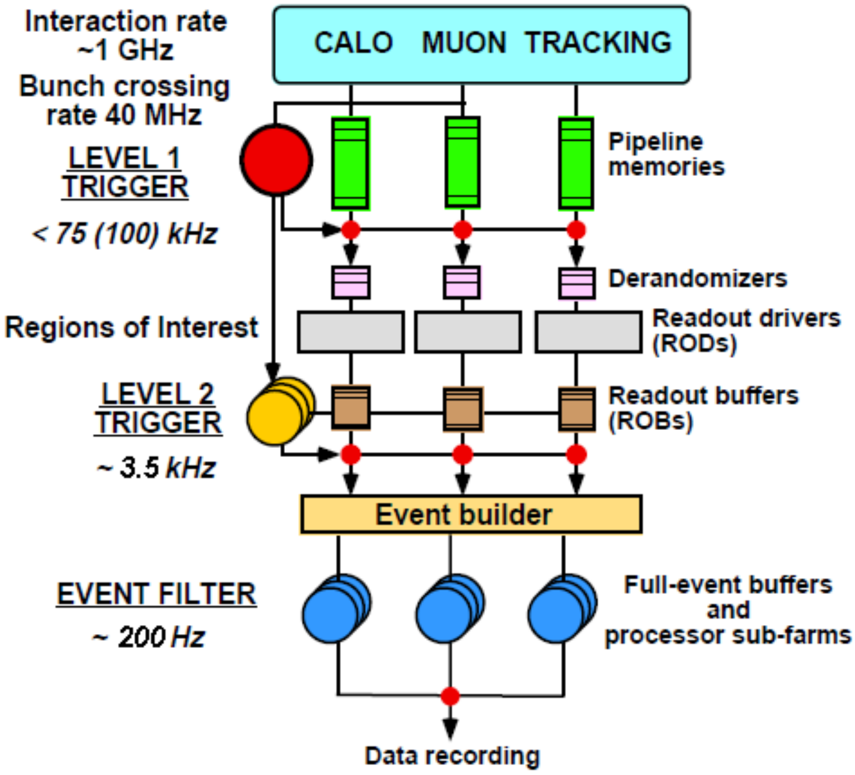

Fig. 4.1: Block diagram of the Trigger and DAQ system[34].

The level-1 trigger makes an initial selection based on reduced-granularity information from a subset of detectors. It consists of the muon trigger and the calorimeter trigger. In the muon trigger, high transverse-momentum (high-p_T) muons are identified using only the trigger chambers, RPCs in the barrel, and TGCs in the end-caps. Detailed description of the level-1 muon trigger is in the next section. The calorimeter selections are based on reduced-granularity information from all the calorimeters (EM and hadronic; barrel, end-cap and forward). Objects searched for by the calorimeter trigger are high-p_T electrons and photons, jets, and τ-leptons decaying into hadrons, as well as large missing and total transverse energies. In the case of the electron/photon and hadron/τ-triggers, energy isolation cuts can be applied. Trigger information is provided for a number of sets of p_T thresholds (generally 6-8 sets of thresholds per object type). The missing and total scalar transverse energies used in the level-1 trigger are calculated by summing over the trigger towers. In addition, a trigger on the scalar sum of jet transverse energies is also available.

The level-1 trigger decision is based on combinations of objects required in coincidence or veto. Most of the physics requirements of ATLAS can be met by using, at the level-1 trigger level, fairly simple selection criteria of a rather inclusive nature. However, the trigger implementation is flexible and it can be programmed to select events using more complicated signatures. The maximum rate at which the ATLAS front-end systems can accept the level-1 triggers is limited to 75 kHz (upgradable to 100 kHz). The rates are expected to be less than this limit but, in case, rates could be significantly reduced without major consequences for the physics programs, for example by increasing the thresholds on some of the inclusive (single-object) triggers when operating at the highest luminosities and by relying more heavily on multi-object triggers.

An essential requirement on the level-1 trigger is that it should uniquely identify the bunch-crossing of interest. Given the short (25 ns) bunch-crossing interval, this is a non-trivial consideration. Therefore, it is important to keep the level-1 latency (time taken to form and distribute the level-1 trigger decision) to a minimum. During this time, information for all detector channels has to be conserved in 'pipeline' memories. These memories are generally contained in custom integrated circuits, placed on or nearby the detectors. The level-1 latency is required to be less than 2.5 μs.

All the detector data for the bunch crossing selected by the level-1 trigger are held in the read-out buffers, either until the event is rejected by the level-2 trigger, in which case the data are discarded, or, in case the event is accepted by level-2, until the data have been successfully transferred by the DAQ system to storage associated with the event filter, which makes the third level of event selection.

The level-2 trigger makes use of 'region-of-interest' (RoI) information provided by the level-1 trigger. This includes information on the position, η and ϕ, and p_T of candidate objects (high-p_T muons, electrons/photons, hadrons/τ, jets), and energy sums (missing-E_T vector and scalar E_T value). The RoI data are sent from level-1 to level-2 for all events selected by the level-1 trigger. Using the RoI information, the level-2 trigger selectively accesses data from the read-out buffers, moving only the data required to make the level-2 decision. It is expected that level-2 will reduce the rate less than 3.5 kHz and the latency of the level-2 trigger is variable from event to event and is expected to be 40 ms average.

After level-2, the last stage of the online selection is performed by the event filter. It employs offline algorithms and methods, adapted to the online environment, and use the most up to date calibration and alignment information and the magnetic field map. The event filter will make the final selection of physics events written to mass storage for subsequent full offline analysis. The output rate from level-2 should then be reduced by an order of magnitude, giving less than 200 Hz, corresponding to an output data rate less than 300 MB/s if the full event data are to be recorded.

4.2 The level-1 muon trigger

This section describes the segmentation of the system in the trigger, the muon trigger algorithm and data flow mechanism to deliver the trigger result to the level-2 trigger.

4.2.1 System segmentation

The muon trigger system is logically divided into small regions in η and ϕ. The way of the segmentation is described in this section.

Segmentation for the end-cap

Figure 4.2 shows the pivot plane octant. The pivot plane is divided into two regions, End-cap ($|\eta| < 1.9$) and Forward ($|\eta| > 1.9$). The End-cap region of each octant is divided into six trigger sectors in ϕ, where a trigger sector is a logical unit that is treated independently in the trigger. Similarly the Forward region of each octant is divided into three trigger sectors. Thus, there are 48 End-cap trigger sectors and 24 Forward sectors in each end-cap. The smallest regions shown in Fig. 4.2 are trigger subsectors which correspond to the smallest unit area of the trigger segmentation. A trigger subsector corresponds to eight channels of wire-groups and eight channels of read-out strips. An End-cap trigger sector contains 37 η rows by 4 ϕ columns of trigger subsectors, a total of 148 trigger subsectors. A Forward trigger sector contains 16 η rows by 4 ϕ columns of trigger subsectors, a total of 64 trigger subsectors. Each η-ϕ trigger subsector corresponds to one Region of Interest (RoI).

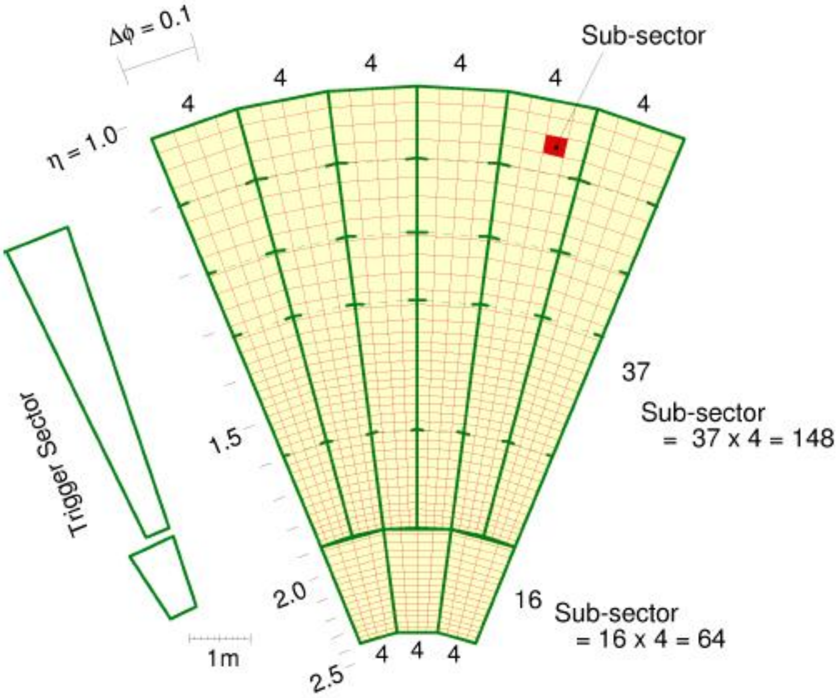

Fig. 4.2: TGC level-1 trigger segmentation for an octant[32]. One octant is divided into six End-cap sectors and three Forward sectors. Bold lines in the figure indicate individual trigger sectors. They are further subdivided into trigger subsectors.

Segmentation for the barrel

In the trigger, the barrel is divided into two parts, $\eta < 0$ and $\eta > 0$. Within each half barrel, 32 sectors are defined. The Barrel Large (BL) chambers and the Barrel Small (BS) chambers of both middle and outer RPC stations (shown in Fig. 4.3) are logically divided in the two to produce two large sectors and two small sectors per half-barrel octant. A sector is segmented in Pads. A large sector contains six Pads, while a small sector contains seven Pads. The region covered by a Pad is $\sim 0.2 \times 0.2$ in $\Delta\eta \times \Delta\phi$. A Pad is divided into RoIs. An RoI covers $\sim 0.1 \times 0.1$ in $\Delta\eta \times \Delta\phi$. The total number of Pads is 448 for the small sectors and 384 for the large sectors. Since one Pad covers four RoIs, the total number of RoIs is 1664.

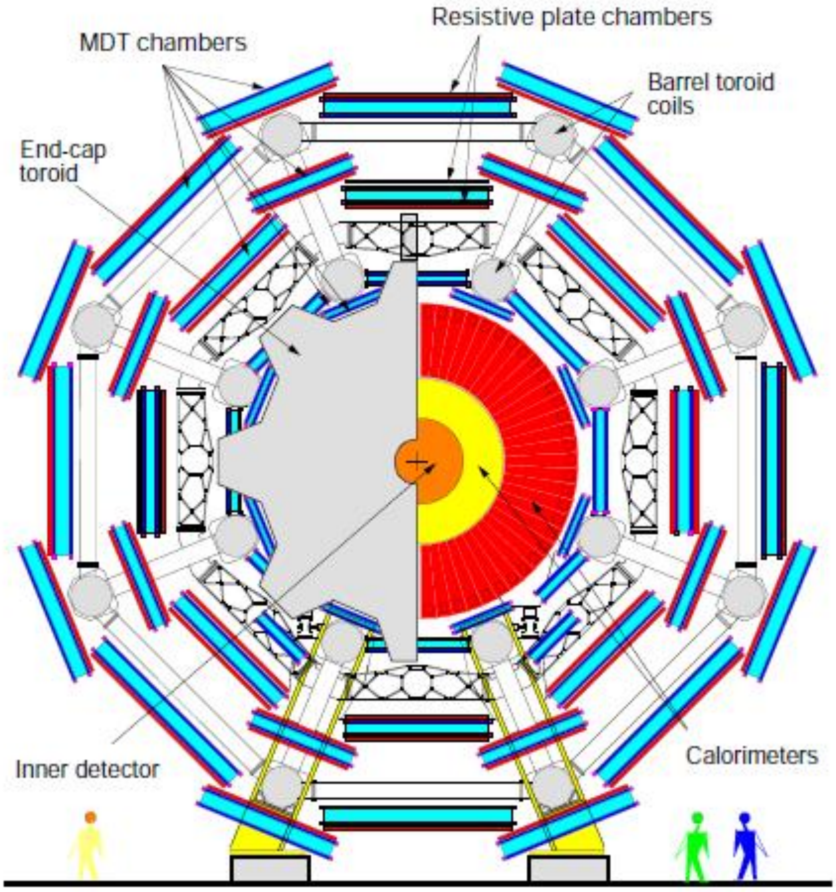

Fig. 4.3: Transverse view of the muon spectrometer, where RPCs are colored in red. RPCs around the barrel toroid coils are the BS chambers and the others are the BL chambers.

4.2.2 Muon trigger algorithms

The level-1 muon trigger is based on the measurement of muon trajectories in three stations. Muons are bent by the magnetic field generated by the toroids and the curvature depends on their momentum and the field integral along their trajectories. Multiple scattering in the material traversed and the energy-loss fluctuation for low-p_T muons are also sources of bending.

The trigger plane the farthest from the interaction point in the end-cap or the second farthest in the barrel, is called the pivot plane (TGC3 or RPC2 in Fig. 4.4). Starting from the hits in the pivot plane, the position difference from a straight-line trajectory of an infinite-momentum track connecting the nominal interaction point and the hit in the pivot plane are measured at the other two trigger stations. There are two steps called "low-p_T coincidence" and "high-p_T coincidence" in the level-1 muon trigger. First, the low-p_T coincidence is examined and if satisfied, the high-p_T coincidence is processed. The low-p_T coincidence uses the pivot plane and the nearer one (TGC2 or RPC1), while the high-p_T coincidence uses the pivot plane and the farther one (TGC1 or RPC3). In the low-p_T coincidence, each hit found in the pivot plane is extrapolated to TGC2 or RPC1 along the infinite-momentum track, and then a "coincidence window" (mentioned below) is defined around the extrapolated point, where the window size depends upon the required p_T threshold. Then, the low-p_T coincidence is satisfied if there is at least one hit within the window for both projections of η and ϕ and at least one of the two low-p_T stations has hits in both trigger planes satisfying the three-out-of-four logic. A similar procedure is performed for the high-p_T coincidence using the next planes (TGC1 or RPC3). The high-p_T coincidence is satisfied if the track has at least one hit in the two trigger planes of RPC3 within the coincidence window in the barrel, or at least two of the three planes of TGC1 in the η view and one of the two planes of TGC1 in the ϕ view have a hit within the coincidence window.

Thus, the level-1 muon trigger is performed and the trigger information including trigger positions and thresholds is sent to the level-2 trigger.

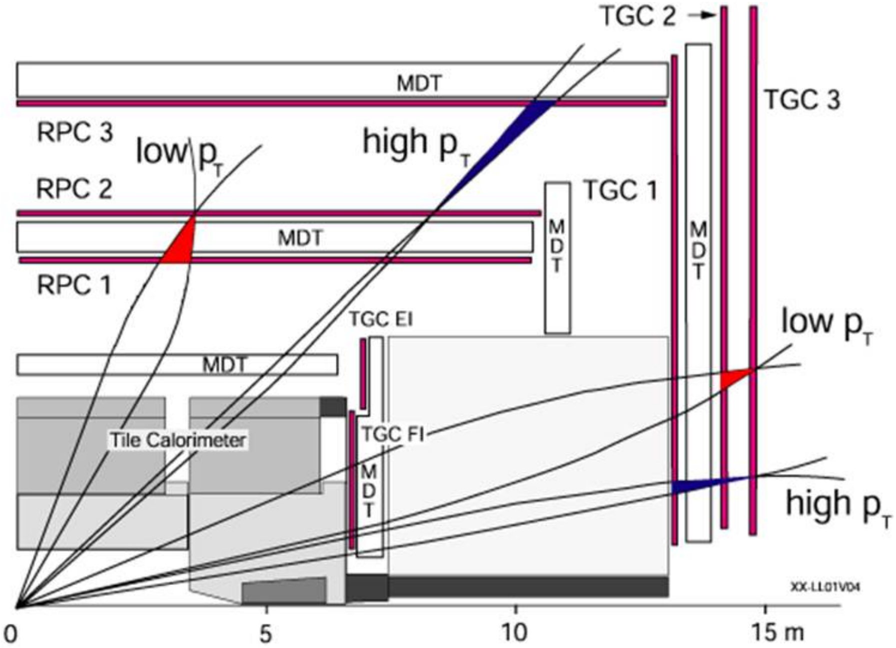

Fig. 4.4: Level-1 muon trigger system layout.

Coincidence window

The trigger windows are created separately for each trigger unit in order to take into account the fact that the magnetic field and material thickness are different in each region. The size of the windows are computed by tracking single muons through the ATLAS detector using Monte Calro simulation.

For the end-cap, the coincidence windows are defined as areas in two dimensions on the surface of the target plane in the two projections of η and ϕ. Then, the size of the window is defined such that 95 % of the muons of each charge within the detector acceptance, generated with transverse momentum equal to the threshold, are accepted. Here, the effect of multiple scattering is taken into account.

For the barrel, the coincidence windows are defined separately in the projections of η and ϕ. The size of the window is defined in the similar way of the end-cap, where the value 95 is replaced by 90.

In both case, the coincidence windows divide tracks into six p_T levels by the distance between the infinite-momentum track and the exact hit positions if exist in the window. An example of the window is shown in Fig. 4.5 and 4.6. Such a window is created for each RoI following the way above, and will be re-created using collision data.

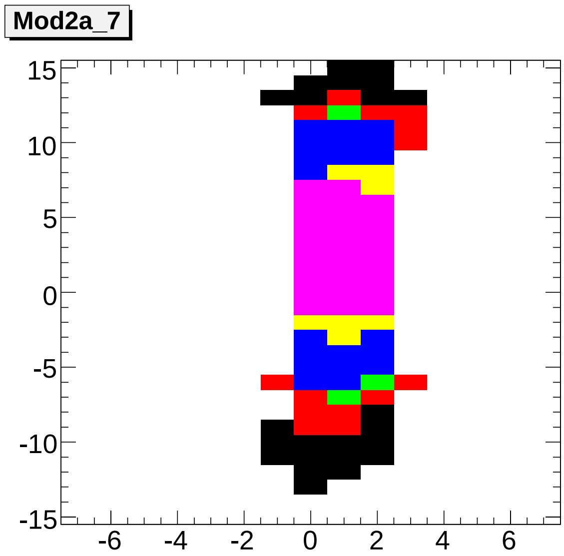

Fig. 4.5: One of the coincidence windows in the end-cap. Black region represents the window for 6 GeV threshold. In the same way, red/green/blue/yellow/magenta region represents the window for 8/10/11/20/40 GeV threshold. If there are overlaps between windows for different thresholds, the overlap region is defined as for the higher threshold. The x-axis represents $\Delta\phi$ and the y-axis represents ΔR.

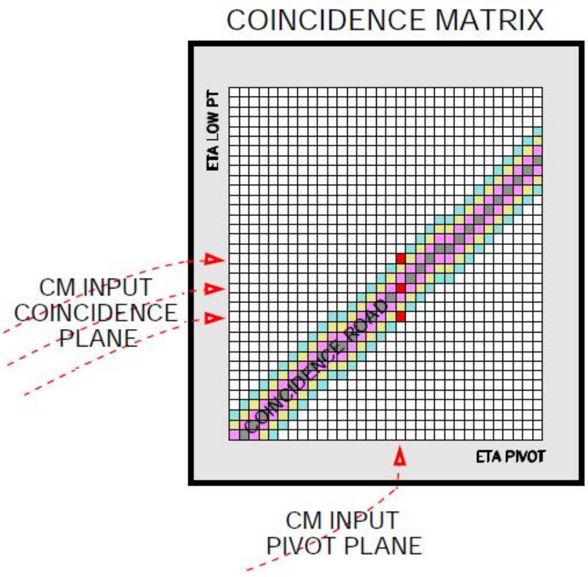

Fig. 4.6: One of the coincidence windows in the barrel.

4.2.3 Data flow in the muon trigger

A block diagram of the level-1 muon trigger system is shown in Fig. 4.7. The muon trigger system is divided into three subsystems. Two of them are associated with the RPC detector and TGC detector. The MUCTPI combines information from the two subsystems and forms the interface to the Central Trigger Processor (CTP). In this section, data flow in these three trigger subsystems are described.

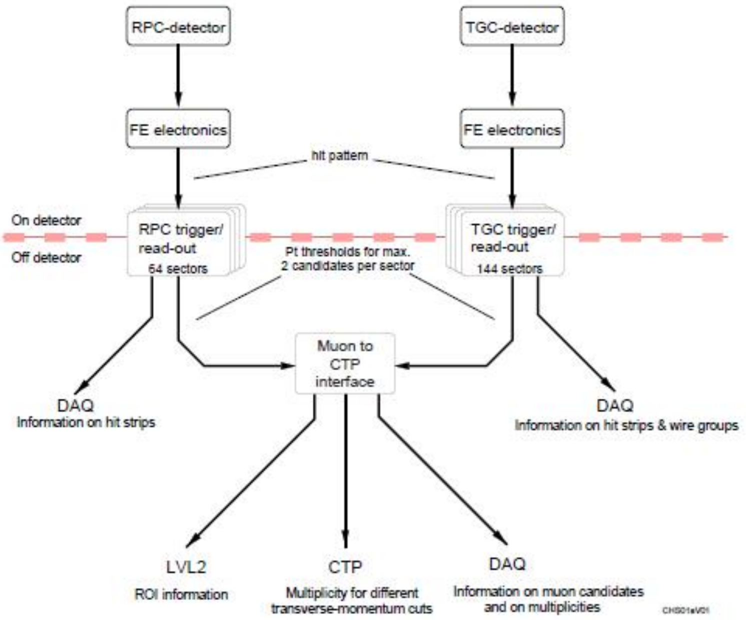

Fig. 4.7: Block diagram of the level-1 muon trigger system. The left three parts from the top represent the RPC subsystem, the right three parts from the top represent the TGC subsystem and the center one is MUCTPI.

4.2.3.1 Data flow in the TGC system

The signals generated by the TGCs are amplified, discriminated and shaped on the detector. On-detector electronics first identify the bunch-crossing and then find coincidences independently in r and ϕ projections. The coincidences provide the position in the pivot plane, r and ϕ and the track's deviation from the infinite-momentum track, Δr and $\Delta\phi$. Electronics placed outside the ATLAS cavern combines r and ϕ measurements to make trigger signals passed to the MUCTPI. The chamber hits and coincidence outputs are read out by the on- and off-detector electronics.

Figure 4.8 shows an overview of the TGC level-1 trigger electronics scheme and the placement of these electronics relative to the trigger chambers. The wire and strip signals emerging from the TGCs are fed into a two-stage amplifier in an Amplifier Shaper Discriminator (ASD) circuit. Four such circuits are built into a single ASD chip and four ASD chips are incorporated into an ASD board. The ASD board is physically attached to the edge of a TGC and enclosed inside the TGC electrical shielding.

Signals from the ASD Boards are sent to a PS-Board where Patch-Panel (PP) ASICs and Slave Board (SLB) ASICs are implemented. PS-Boards are placed on the accessible outer surfaces of the TGC wheels except for EI/FI PS-Boards. Thus, electronics for the two doublets are mounted on the outside of the outer doublet wheel and those for the triplets on the inner surface of the triplet wheel. The PP ASIC has 32 channels of Bunch-Crossing Identification (BCID) circuits. Outputs from PP are fed to the on-board logic to take care of physical overlap in the TGCs and fan-outs. The processed signals are sent to corresponding SLB ASICs where the coincidence and read-out circuits are placed. There are five different types of PS Boards; wire and strip boards for each of the triplet and doublets and a board for the EI/FI chamber. They differ in their number of inputs, the kind of coincidence made and the maximum window width. Information from the SLBs for the triplet and doublets is encoded to produce more compact signals and the encoded coincidence information is passed to a High-p_T coincidence Board located near the outer rim of the triplet wheel. Signals from the doublet and triplet SLBs are combined here to find high-p_T track candidates. Wire (R-coordinate) and strip (ϕ-coordinate) information is treated separately.

Signals from the High-p_T Boards are sent to Sector Logic Boards containing an R-ϕ coincidence unit and track selectors, to select the highest-p_T candidates. In the Sector Logic, hit information from EI/FI SLBs is incorporated to the trigger logic. This provides good robustness against soft charged particles due to the very large field integral produced by the forward toroids located between the big wheel and the innermost muon station. The Sector Logic boards are located in the counting room "USA15" outside the main ATLAS cavern. The resulting trigger information is sent to the MUCTPI in a standard format. The total latency of the system, from the bunch-crossing in which the interaction occurs until the delivery of the LVL1 track candidates to the MUCTPI is 1.20 μs.

Full-information data sets are read-out through the DAQ system in parallel with the primary trigger-logic. For read-out purposes, each PS-Board is connected to the Star Switch (SSW) which manages the data collection for a Local DAQ Block. Data from the SSW is transferred to the Read Out Drivers (ROD) via S-LINK (using optical fiber) in USA15.

The DCS has been developed on a ATLAS wide system to control and monitor detectors. The DCS is a slow path primarily for monitoring the environment, power, gas flow, etc. TGC DCS is implemented by using the CAN-bus system.

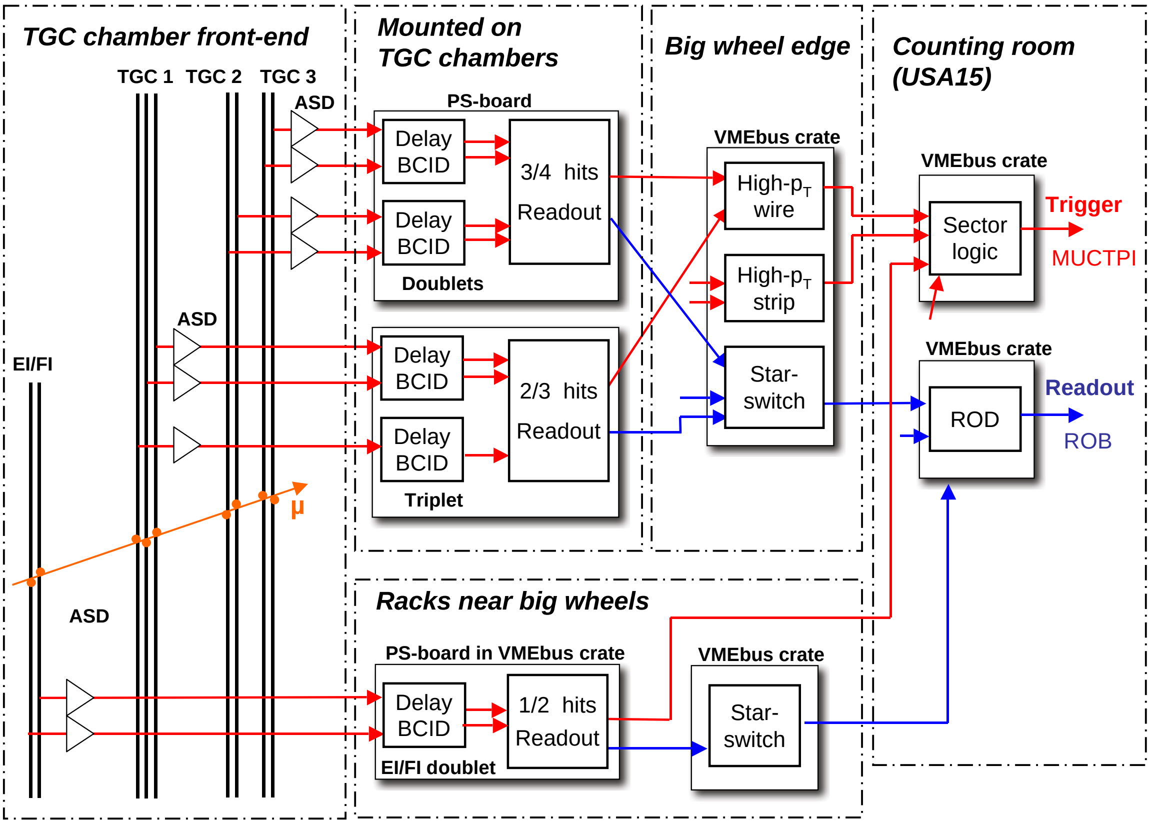

Fig. 4.8: Overview of the TGC level-1 trigger scheme[32].

4.2.3.2 Data flow in the RPC system

The barrel level-1 muon trigger system is divided in an on-detector and an off-detector part. The RPC detector front-end electronics resides in the detector itself, and is connected to the on-detector trigger electronics via flat cables. Each RPC has got two sets of 8-channels connectors, one per each strip layer, on both the bending (η) and the non-bending (ϕ) sides. The on-detector electronics is made of splitter boxes and trigger processors boxes (also called PAD). Because of overlapping coincidence windows in the confirm RPC detector planes, signals coming from the inner and outer RPCs need to be sent to more than one trigger processor box. A splitter box, mounted near each PAD box, is used to split detector signals and to fan-out them to more than one trigger processor box. One PAD box is mounted on top of each half-RPC station (each half-RPC belongs to a distinct trigger sector). A trigger tower is composed of one low-p_T PAD box mounted on top of one middle RPC station, reading-out the inner and the pivot RPC chambers, and one high-p_T PAD box mounted on top of the outer station, reading-out the low-p_T trigger result and the outer RPC chamber signals. Each PAD box hosts four Coincidence Matrix ASICs, two per each view. One CMA contains both trigger and RPC readout logic, it processes signals coming from up to four detector layers, tags hit information to time bins of 3.125 ns (1/8 of a bunch crossing period), and tags events to the corresponding bunch crossing number. The ASIC has got a pipeline based architecture working at a clock speed of 320 MHz. The CMA trigger algorithm looks for hit coincidences within up to four different RPC detector layers inside the programmed geometrical road. A 1/4, 2/4, 3/4 or 4/4 majority logic can be applied. The trigger logic is replicated three times inside one CMA, so that three different threshold cut can be simultaneously applied. Trigger and readout results coming out from the CMAs are collected together in the local PAD logic (which resides into a FPGA chip), which assembles event data and calculates the RoIs. Low-p_T trigger and readout results are sent via flat cables to the high-p_T trigger box, which applies the high-p_T algorithm and sends results to the off-detector electronics via an optical fiber. Six or seven optical fibers coming from one trigger sector go to one VME Sector-Logic/RX module, which elaborates the collected trigger and readout data, and sends readout and trigger data respectively to the ROD and to the MUCTPI. A schematic view of the system is shown in Fig. 4.9.

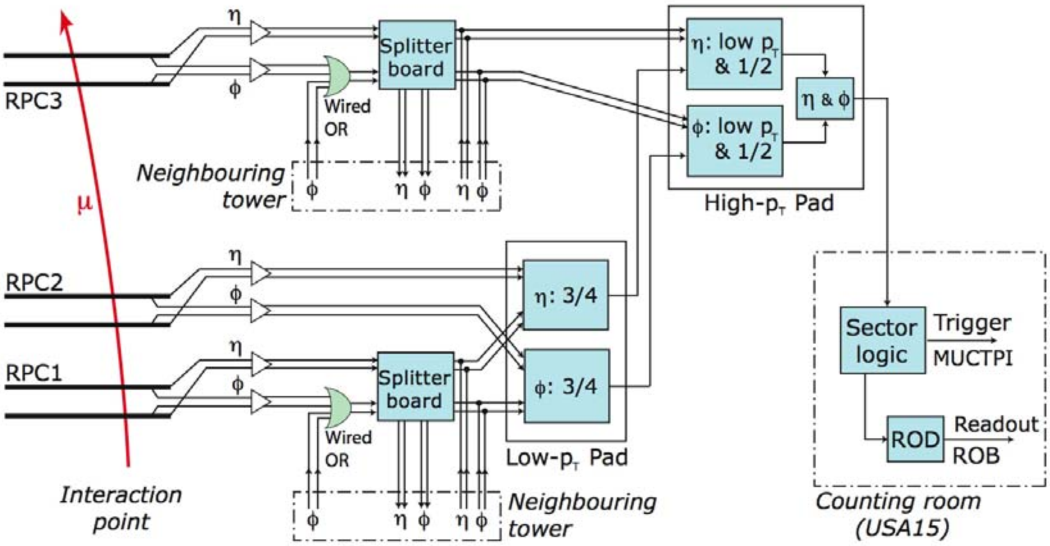

Fig. 4.9: Overview of the RPC level-1 muon trigger scheme[32].

4.2.3.3 Muon trigger interface to the CTP (MUCTPI)

The results from the Detector-Specific Logic (DSL) associated with the RPC and TGC systems form the input to the MUCTPI as mentioned above and provide on up to two muon track candidates per sector. The information includes the position and p_T range of the track candidates. The MUCTPI combines the information from all of the sectors and calculates total multiplicity values for each of the six p_T thresholds. These multiplicity values are sent to the CTP. Here, the maximum overall multiplicity is seven candidates and larger multiplicity values are rounded down to seven. In forming the multiplicities, care has to be taken to avoid double-counting single muons in regions where trigger chambers overlap. In such regions, some muons cross overlapping trigger chambers and hits are produced in both chambers. If the chambers belong to different sectors, the DSL may produce two muon candidates. Doubly-counted single muons could dominate the low-p_T dimuon trigger, giving an unacceptably high rate.

Since the data received by the MUCTPI come from different parts of the detector, the MUCTPI have to align the input data in time, compensating for different times of flight and signal propagation delays, so that only data corresponding to the same bunch crossing are used to form multiplicities and for defining RoIs.

Additional functions of the MUCTPI are to provide data to the level-2 trigger and to the DAQ system for events selected at the level-1 trigger. The level-2 trigger is sent a formatted copy of the information on candidate muon tracks. This information is used to define regions of interest (RoIs) that drive the level-2 muon-trigger processing. The DAQ system receives a more complete set of information. The information sent to the level-2 trigger is ordered, according to decreasing in p_T.

4.3 Handling of triggered data

The following datasets corresponding to different stages of reconstruction are available in the ATLAS experiment:

- **Byte-stream Data:** The event data flowing from the detectors through the event filter;
- **Raw Data Object (RDO):** A C++ object representation of the byte-stream information;
- **Event Summary Data (ESD):** The detailed output of the reconstruction produced from the RDO;
- **Analysis Object Data (AOD):** A summary of the reconstructed event.

The ATLAS detector will produce about a few PB of raw data per year, a vast amount of information which prohibits the simple distribution to worldwide collaborators. To enable physicists to analyze the data at remote sites, these types of datasets above are produced.

At the first step of the reconstruction, the byte-stream data is converted to the raw data object to apply the reconstruction algorithms written in C++ or FORTRAN. In the tracking system, another data type “prepared raw data” (PrepRawData) is used, which is created from the RDO to find tracks in the algorithms. It contains clusters from the pixel detector or drift circles from the MDTs. After the reconstruction, ESDs and AODs are created.

The ESD includes the PrepRawData. Therefore, it contains sufficient information to allow particle identification, track re-fitting, jet calibration and so on, thus allowing for the rapid tuning of reconstruction algorithms and calibrations. The target file size of ESD is 500 kB/event.

While the ESD contains the persistifiable output of the reconstruction, the AOD contains information for common analysis. For example, track information (four-momentum at the interaction point, track fit result, charge, etc.), results of particle identification and trigger information are included. The target file size of AOD is 100 kB/event, five times smaller than that of ESD. The AOD is generally used for physics analysis and, if more detailed information is needed, the ESD is analyzed.

In the ATLAS collaboration, these operations are performed using a common frame work called "Athena". All tools for the data preparation and the physics analysis are implemented according to this frame work. Simulation studies can also be done. A large amount of AODs were produced using the Monte Calro simulation for both detector and physics studies ahead of the data taking. Various physics events are generated using several event generators. After applying the detector simulation, the byte-stream data is created and, in the same way as used in the data taking, ESDs and AODs are created.

5 Muon reconstruction at ATLAS

The design of the ATLAS Muon Spectrometer is unprecedented for its size and precision. The fact remains that muons leave their mark in all of the detector subsystems: in the inner detectors, in the electromagnetic and hadronic calorimeters and in the muon spectrometer. Therefore, optimal muon identification and measurements is obtained when information from each subsystem is fully incorporated into the reconstruction algorithms. In this chapter, the tracking algorithms for the inner detector and the muon spectrometer are described and the expected performance of the muon reconstruction is represented.

5.1 Reconstruction of charged particles in the inner detector

Track reconstruction in the inner detector is logically sub-divided into three stages:

- A pre-processing stage, in which the raw data from the pixel and SCT detectors are converted into clusters and the TRT raw timing information is turned into calibrated drift circles. The SCT clusters are transformed into space-points, using a combination of the cluster information from opposite sides of a SCT module.

- A track-finding stage, in which different tracking strategies, optimized to cover different applications, are implemented. The default tracking exploits the high granularity of the pixel and SCT detectors to find prompt tracks originating from the vicinity of the interaction region. First, track seeds are formed from a combination of space-points in the three pixel layers and the first SCT layer. These seeds are then extended throughout the SCT to form track candidates. Next, these candidates are fitted, outlier clusters are removed, ambiguities in the cluster-to-track association are resolved, and fake tracks are rejected. This is achieved by applying quality cuts, e.g. on the number of associated clusters, with explicit limits set on the number of clusters shared between several tracks and the number of holes per track (a hole is defined as a silicon sensor crossed by a track without generating any associated cluster). The selected tracks are then extended into the TRT to associate driftcircle information in a road around the extrapolation and to resolve the left-right ambiguities. Finally, the extended tracks are refitted with the full information of all three detectors and the quality of the refitted tracks is compared to the silicon-only track candidates and hits on track extensions resulting in bad fits are labeled as outliers (they are kept as part of the track but are not included in the fit). A complementary track-finding strategy, called back-tracking, searches for unused track segments in the TRT. Such segments are extended into the SCT and pixel detectors to improve the tracking efficiency for secondary tracks from conversions or decays of long-lived particles.

- A post-processing stage, in which a dedicated vertex finder is used to reconstruct primary vertices. This is followed by algorithms dedicated to the reconstruction of photon conversions and of secondary vertices.

Common components and modules of the inner detector tracking is spread widely into the tracking algorithm for the muon system and combined reconstruction. The common ATLAS tracking Event Data Model (EDM) is also established as the input event data format of all track reconstruction algorithms of the muon system.

5.2 Reconstruction in the muon spectrometer

Muons with momenta from ∼3 GeV to 3 TeV are identified and measured with optimal acceptance and efficiency through the use of a combination of the following three track reconstruction strategies:

- Stand-alone: muon track reconstruction based solely on the muon spectrometer data over the range $|\eta| < 2.7$ (defined by the spectrometer acceptance).
- Combined: combination of a muon-spectrometer track with an inner-detector track over the range $|\eta| < 2.5$ (defined by the inner-detector acceptance).
- Segment tag: combination of an inner-detector track with a muon-spectrometer segment, i.e. a straight-line track, in an inner muon station.

Track reconstruction in the muon spectrometer is logically sub-divided into the following stages: preprocessing of raw data to form drift-circles in the MDT's or clusters in the CSC's and the trigger chambers (RPC's and TGC's), pattern-finding and segment-making, segmentcombining, and finally track-fitting. Track segments are defined as straight lines in a single MDT or CSC station. The search for segments is seeded by a reconstructed pattern of drift-circles or clusters or by drift-circles or clusters lying in a region of activity, which is defined by the trigger chambers and has a size of the order of 0.4×0.4 in η-ϕ space. Full-fledged track candidates are built from segments, starting from the outer and middle stations and extrapolating back through the magnetic field to the segments reconstructed in the other stations. Each time a reasonable match is found, the segment is added to the track candidate. The final track-fitting procedure takes into account, in full detail, the geometrical description of the traversed material and the magnetic field inhomogeneities along the muon trajectory. The muon-spectrometer track parameters are determined at the inner stations, which yield the first set of measurements in the muon spectrometer. The track is then propagated back to the interaction point and the momentum is corrected for the energy loss in the calorimeters (and in the inner detector). The energy lost by dE/dX in the calorimeters is estimated by an algorithm, which uses either the parameterized expected energy loss or the measured calorimeter energy. The measured energy is used only if it exceeds significantly the most probable energy loss and if the muon track is isolated. The combination of the stand-alone tracks reconstructed in the muon spectrometer with tracks reconstructed in the inner detector is performed in the region $|\eta| < 2.5$, which corresponds to the geometrical acceptance of the inner detector. This combination will considerably improve the momentum resolution for tracks with momenta below 100 GeV, but will also suppress to a certain extent backgrounds from pion punch-through and from pion or kaon decays in flight. In the case of segment tags, inner-detector tracks are extrapolated to the inner muon stations and either associated directly to reconstructed muon segments or used to select muon drift-circles and clusters in a cone with typically a size of 100 mrad, from which track segments are then reconstructed. The muons reconstructed through this procedure provide an important improvement to the stand-alone muon reconstruction for three main reasons:

- at momenta below typically 6 GeV, muon tracks do not always reach the middle and outer muon stations;
- in the barrel/end-cap transition region with $1.1 < |\eta| < 1.7$, the middle stations are missing for the initial data-taking (EES and EEL chambers in table 6.4) and the stand-alone reconstruction efficiency is reduced in this region;
- in the difficult regions at $|\eta| \sim 0$ and in the feet, the geometrical acceptance of the muon stations is considerably reduced.

5.3 Performance of the muon reconstruction

This section presents the expected performance of the muon tracking algorithm. The main quantities, the momentum resolution and the reconstruction efficiency, are measured using the Monte Calro simulation.

The expected momentum resolution as a function of η, averaged over ϕ, for single muon with $p_T = 100$ GeV is shown in Fig. 5.1, where the results obtained for stand-alone tracks and combined tracks are shown. The resolution as a function of ϕ in the region $0.3 < |\eta| < 0.65$ is also shown in Fig. 5.2. Over a large fraction of the acceptance, the stand-alone resolution is close to 3 %. The small degradations appearing at $\phi = 240$ and 300 degree are due to the experimental structures. The large degradation in $1.1 < |\eta| < 1.7$ is due to several effects. In $1.1 < |\eta| < 1.3$, the degradation is due to the absence of the middle muon stations in the barrel/end-cap transition region. At large $|\eta|$, the degradation is due to the combination of the low bending power of the magnetic field in the transition region between the barrel and the end-cap toroids and of the large amount of material in the coils of the end-cap toroid in limited regions in ϕ.

The stand-alone momentum resolution of muons with $p_T = 100$ GeV as a function of η and ϕ is shown in Fig. 5.3. Momentum measurement is impossible at $|\eta| < 0.1$ and $|\eta| = 1.3$ because of holes in the acceptance of the muon spectrometer. The resolution is degraded at $|\eta|$ =0.2, 0.3 and 0.7 due to support structures of the barrel toroid magnet coils. The degradation in $1.2 < |\eta| < 1.7$ and regions corresponding to ϕ-values multiples of 22.5 degree is caused by the small bending power of the magnetic field in these regions.

In Fig. 5.4 and 5.5, the single muon reconstruction efficiency is shown, respectively as a function of η for muons with $p_T = 100$ GeV and as a function of p_T. The results are shown for stand-alone reconstruction, for combined reconstruction and for the overall combination of these with the segment tags. The degradation in Fig. 5.4 is due to the same reason above.

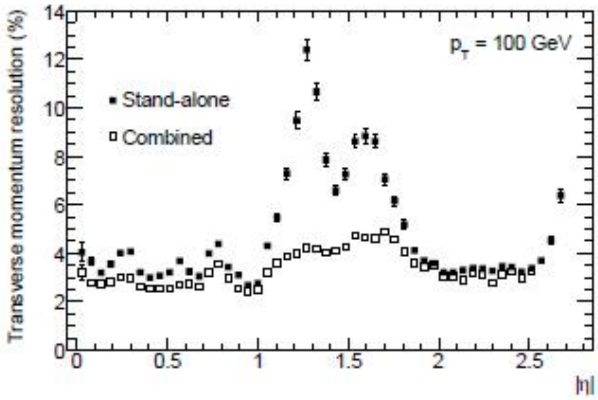

Fig. 5.1: Expected momentum resolution for muons with $p_T = 100$ GeV as a function of $|\eta|$. The results for stand-alone and combined reconstruction are shown.

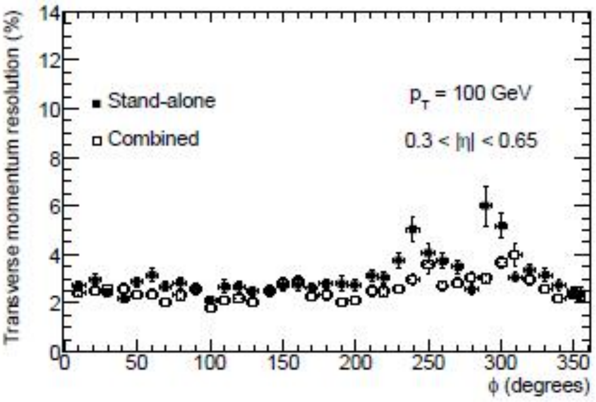

Fig. 5.2: Expected momentum resolution for muons with $p_T = 100$ GeV as a function of ϕ. The results for stand-alone and combined reconstruction are shown.

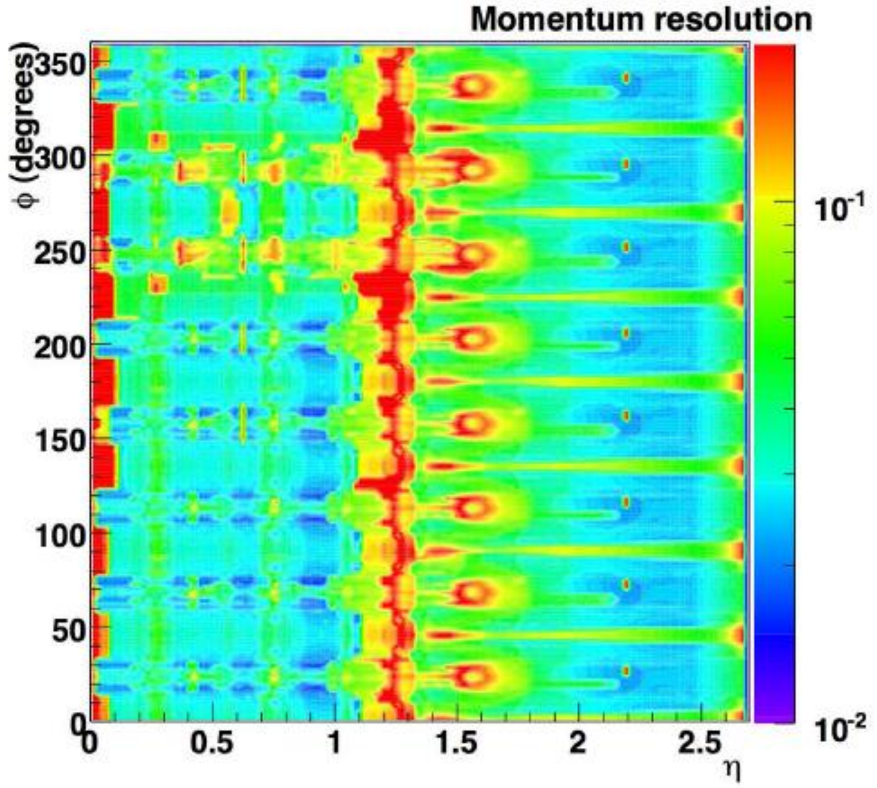

Fig. 5.3: Expected momentum resolution as a function of $|\eta|$ and ϕ for muons with $p_T = 100$ GeV.

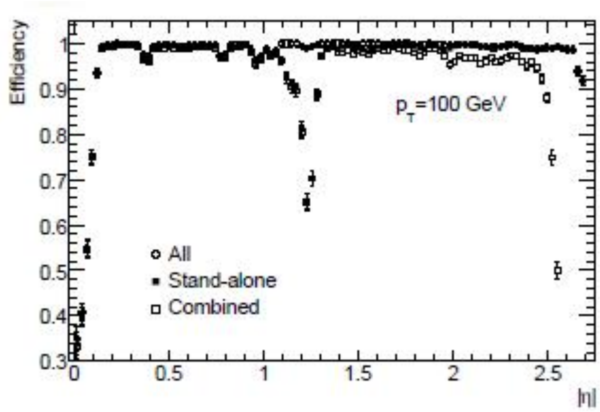

Fig. 5.4: Reconstruction efficiency as a function of $|\eta|$ for muons with $p_T = 100$ GeV.

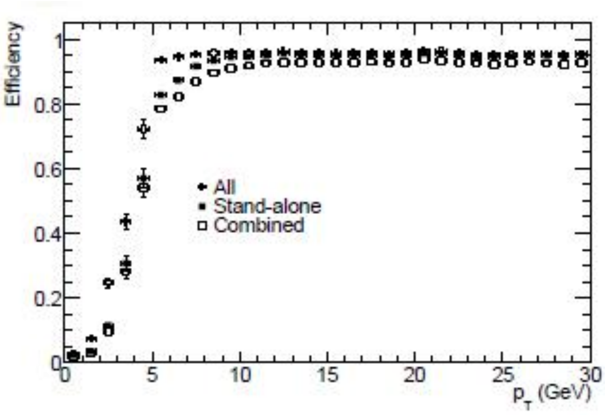

Fig. 5.5: Reconstruction efficiency as a function of p_T for muons with $p_T = 100$ GeV.

6 Expected performance of the level-1 muon trigger

The purpose of the level-1 muon trigger is to collect events with muons with p_T over the threshold at high efficiency. It is also very important to avoid mis-selection of events in order to keep fair trigger rate. Since a large amount of low-p_T muons are expected from QCD events, it is required to have a good rejection power for low-p_T muons below the threshold. The allowed rate for the level-1 muon trigger is about 30 kHz. Pre-scaled trigger can not be avoided if the trigger rate exceeds the limit.

The performance of the system is studied using Monte Carlo simulation in terms of the efficiency and trigger rate. In this study, single muon samples, having only one muon in each event, are used to calculate expected trigger efficiencies and rates, which are independent from event selection and track reconstruction. Detailed studies are demonstrated in this chapter.

6.1 Performance of Single Muon Trigger

First the performance of the single muon trigger, which requires one or more muons with p_T over threshold in an event, is studied. The muon trigger efficiency and the muon trigger rate are calculated to evaluate the single muon trigger.

6.1.1 Muon Trigger Efficiency

The muon trigger efficiency is defined as the ratio of the number of triggered muons ($N_\mu^{triggered}$) to the number of all muons (N_μ^{all}):

$$\varepsilon_{trigger} = \frac{N_\mu^{triggered}}{N_\mu^{all}}. \tag{6.1}$$

Muons are defined as triggered if a muon has a corresponding level-1 RoI information. Because the single muon samples are used, existence of level-1 RoI information in an event means that the muon in the event is triggered. Therefore, N_μ^{all} is equal to the number of events and $N_\mu^{triggered}$ is equal to the number of events having an RoI information. Here, muons from the interaction point with a fixed p_T is simulated in the single muon samples. The muon direction at the interaction point is generated randomly in η and ϕ direction.

First the muon trigger efficiency is calculated as a function of p_T. The results are shown in Fig. 6.1 where “MU06” is one of the trigger menus with 6 GeV threshold and “MU20” is that with 20 GeV threshold. The former is mainly used at the low-luminosity runs and the latter is used at the high-luminosity runs. It can be seen that, in both cases, the efficiencies rise around the threshold and become stable at the plateau. The inefficiency of $\sim$ 10 % at the plateau is due to the way of the coincidence window creation (mentioned in Section 4.2.2). The trigger efficiency curves are fitted by the following function to evaluate the detailed efficiency at the threshold and the plateau. The results are shown in Table 6.1:

$$\epsilon_{1\mu} = \frac{A}{1 + e^{-a(p_T^{\mu} - b)}}, \tag{6.2}$$

where A, a and b are fitting parameters. As a result, the trigger system can achieve high efficiency over the threshold, while a little tail and slope can be seen in the low-p_T region, where a large number of muons are expected. In the next section, the tail and slope are evaluated in terms of the trigger rate.

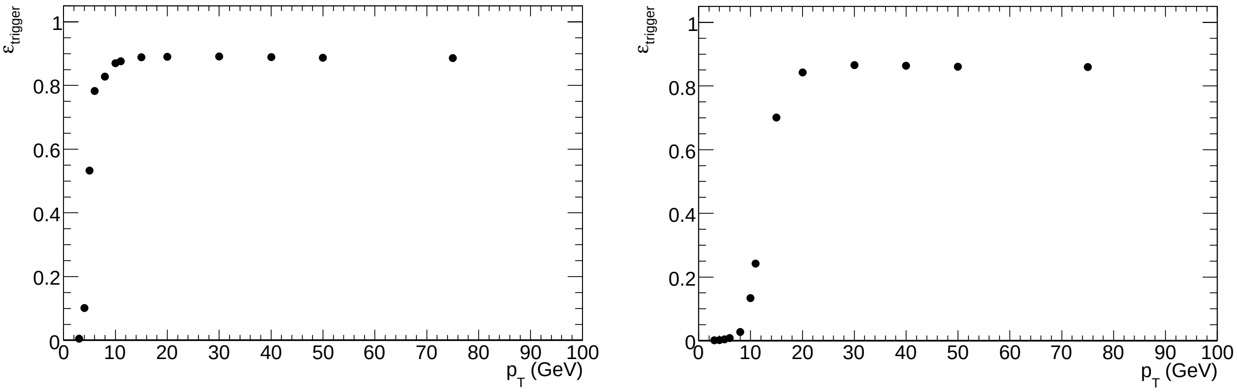

(a) MU06 (b) MU20

Fig. 6.1: Trigger efficiency as a function of p_T.

Trigger menu	$\varepsilon_{trigger}^{threshold}$	$\varepsilon_{trigger}^{plateau}$
MU06	78.3 %	88.9 %
MU20	84.3 %	86.3 %

Table 6.1: Fit results of the muon trigger efficiency vs. p_T.

Next, the trigger efficiency as a function of η and ϕ are calculated to see the position dependence of the muon trigger efficiency. The results are shown in Fig. 6.2. To remove p_T dependence of the efficiency, only muons with p_T higher than 20 GeV are used. At the end-cap region ($1.05 < |\eta| < 2.4$), there are little ϕ dependence and a few % of η dependence. The efficiency is kept to be high all over the end-cap and muons can effectively be triggered there. On the other hand, the efficiency drops significantly in several regions at the barrel ($|\eta| < 1.05$), where support structures go through the muon spectrometer and no muon detector is installed. However, except for such regions, high efficiency is achieved and the system can satisfy the requirements as a whole.

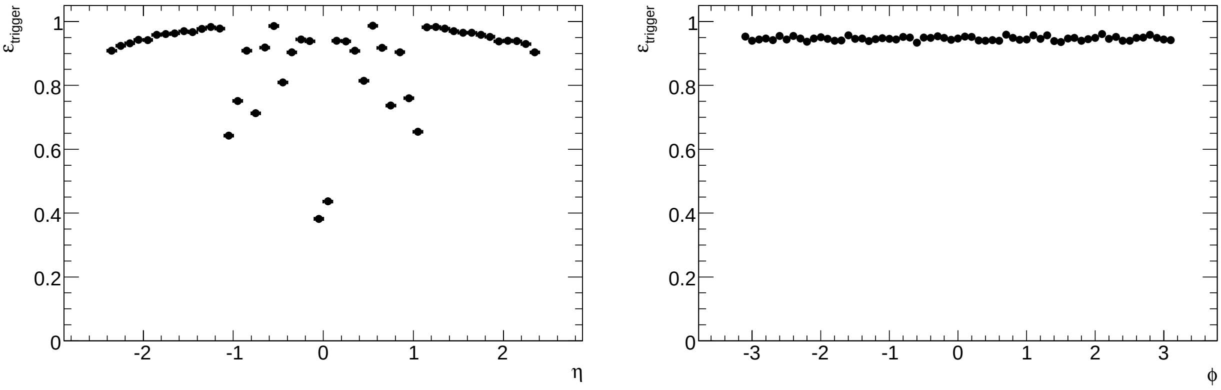

(a-1) $\epsilon_{trigger}$ vs. η (MU06)

(a-2) $\epsilon_{trigger}$ vs. ϕ at the end-cap (MU06)

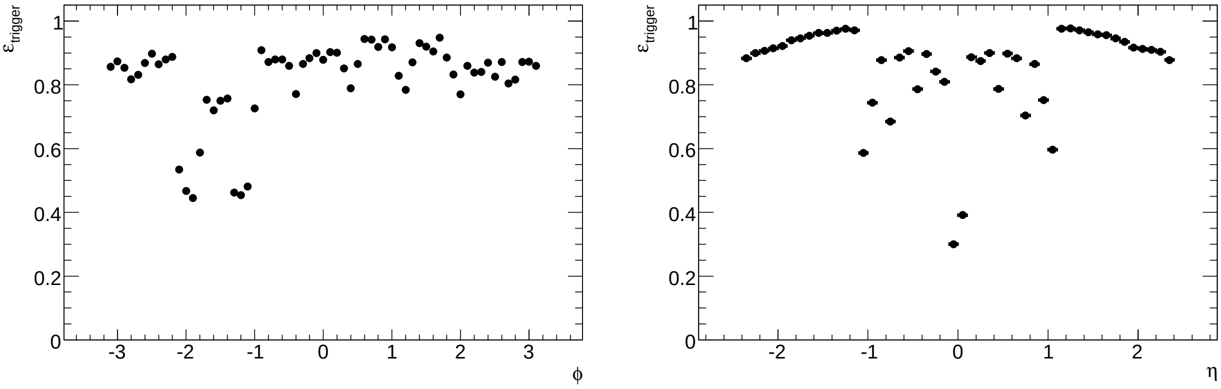

(a-3) $\epsilon_{trigger}$ vs. ϕ at the barrel (MU06)

(b-1) $\epsilon_{trigger}$ vs. η (MU20)

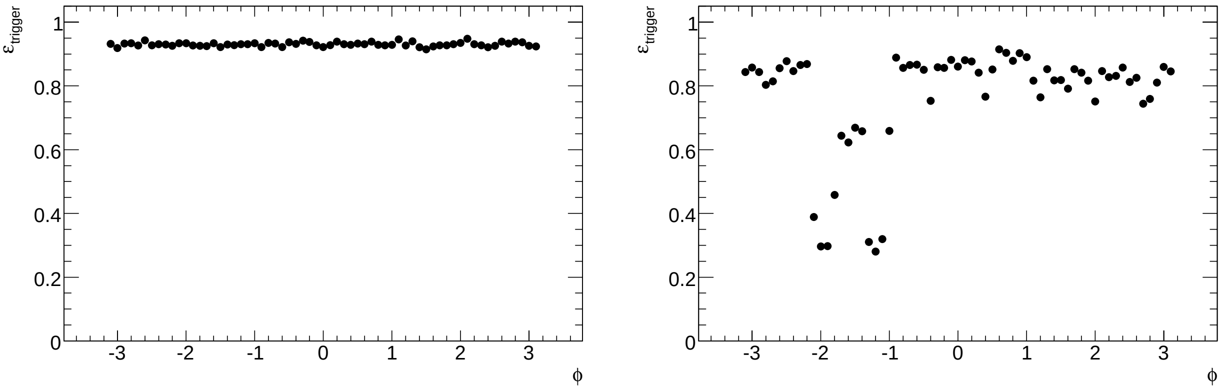

(b-2) $\epsilon_{trigger}$ vs. ϕ at the end-cap (MU20)

(b-3) $\epsilon_{trigger}$ vs. ϕ at the barrel (MU20)

Fig. 6.2: Trigger efficiencies as a function of η for overall and those as a function of ϕ at the barrel and the end-cap, respectively. Top three figures are the case of MU06 and bottom three figures are that of MU20.

6.1.2 Muon Trigger Rate

Another important parameter of the muon trigger system is the trigger rate. The muon trigger rate (R) is calculated roughly as;

$$R = \sigma_\mu \times \epsilon_\mu, \tag{6.3}$$

where σ_μ is the muon production cross-section and ϵ_μ is the muon trigger efficiency. A lot of muons from QCD events are expected, especially in very low-p_T regions. The level-1 muon trigger rate is calculated using the trigger efficiencies and the muon production cross-section obtained above and summarize the results in Table 6.2. It can be found that the effect from muons from QCD events is not negligible. It is because the muon trigger efficiency for very low-p_T regions is quite low but not zero, while the muon production cross-section is quite large. However, the expected rate at both luminosities well satisfy the requirements with respect to the Monte Carlo simulation, while we have to be careful to the contributions from the backgrounds.

Trigger menu	MU06	MU20
Trigger rate (kHz)	36.4	19.3

Table 6.2: Expected trigger rate of MU06/MU20 at the low/high luminosity run, respectively.

7 Measurements of the level-1 muon trigger efficiency from data

The level-1 muon trigger system plays an important role in the first step of the data acquisition as mentioned in Chapter 4. In addition, performance of the system affects physics analysis. For example, good efficiency with high background rejection at the level-1 trigger is crucial for rare production processes. Good understanding of the trigger efficiencies is necessary for cross-section measurements. In Chapter 6, estimation of trigger efficiencies is discussed by using Monte Carlo simulation. However, these estimated values will be affected by various factors; changes of chamber efficiencies and hit rates, mis-cabling and malfunction of trigger electronics. Therefore, it is very important to measure trigger efficiencies in situ, i.e. using real collision data. One of the key points is what kind of events with muon tracks are used for the measurements. Event selection should be as independent as possible from the muon trigger efficiency. In addition, quality of muon reconstruction depends on event topologies. In this chapter, two methods to measure the muon trigger efficiency are discussed.

7.1 Matching of reconstructed muons and trigger information

In this section, how to decide whether a muon is triggered or not is explained. Note that there is no direct information to associate a reconstructed track with a trigger information in AOD. The trigger information given by MUCTPI contains the position at the pivot plane, while reconstructed tracks have momentum direction at the interaction point. As for high momentum tracks, their trajectories are almost straight and the position at the pivot plane can be calculated easily by using their momentum direction at the interaction point. On the other hand, the trajectories of low-p_T muons have large curvature in the toroidal magnetic fields. If we approximate all tracks to be straight, distribution of distance between an extrapolated position and an associated RoI at the pivot plane is measured as shown in Fig. 7.1-(a), where the distance is represented by $\Delta R = \sqrt{\Delta\eta^2 + \Delta\phi^2}$, where $\Delta\eta$ and $\Delta\phi$ are the differences of η and ϕ. In Table 7.1-(a), mean value of each distribution and the value which includes 99.9 % of all entries are shown. It can be seen that the distance is a few times larger than the size of RoIs shown in Table 7.2. This position shift may cause mismatching for lower p_T muons. In order to avoid the mismatching, trajectories of the muons are calculated by taking into account the magnetic fields. This can be achieved by a tool called "Extrapolator", which extrapolates a reconstructed track from the interaction point to a point of any detector component taking into account the effects of the magnetic field. By using the tool, ΔR between the two at the pivot plane becomes smaller as shown in Fig. 7.1-(b). Especially the average distance is reduced by a half for low-p_T muons.

Distribution of the matching ΔR as a function of p_T using Extrapolator is shown in Fig. 7.2 for the end-cap and the barrel, respectively. As you can see, the remaining distance observed for high-p_T muons are mainly from the following reason: not the exact position but the center of RoI is recorded as the triggered position. In this analysis, a muon track is regarded as triggered if it has a matching ΔR within 3σ, where σ is given by the error of Extrapolator and the size of RoI.

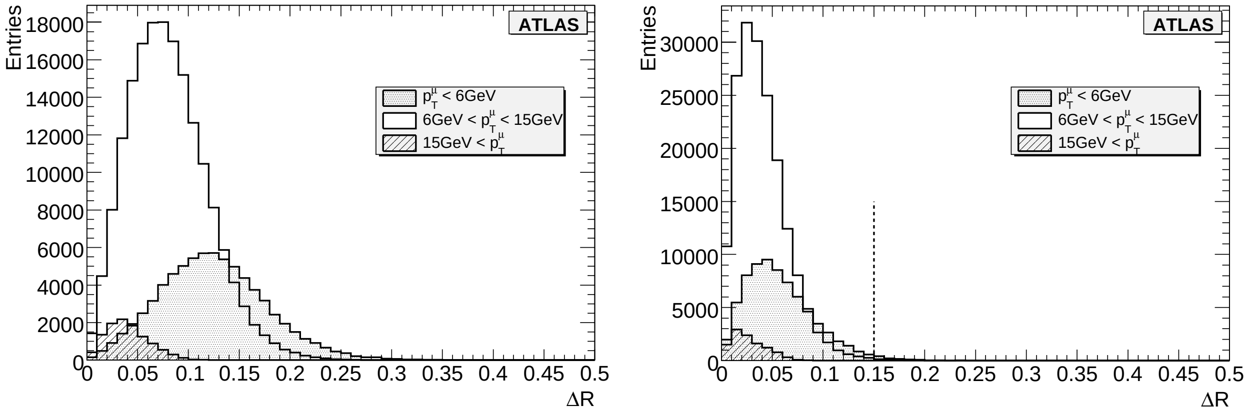

(a) (b)

Fig. 7.1: Matching ΔR distributions for each p_T region without and with the extrapolation in (a) and (b)

Range	mean	99.9 % included
p_T <6 GeV	0.12	0.34
6 GeV< p_T <15 GeV	0.080	0.23
15 GeV< p_T	0.040	0.12

(a)

Range	mean	99.9 % included
p_T <6 GeV	0.058	0.235
6 GeV< p_T <15 GeV	0.040	0.17
15 GeV< p_T	0.027	0.095

(b)

Table 7.1: The mean values and the values including 99.9 % of entries integrated from lower end in Fig. 7.1. (a)/(b) is associated with Fig. 7.1-(a)/(b).

	Barrel ($\lvert\eta\rvert < 1.05$)	End-cap 1 ($1.05 < \lvert\eta\rvert < 1.95$)	End-cap 2 ($1.95 < \lvert\eta\rvert$)
η	~ 0.1	~ 0.024	~ 0.032
ϕ	~ 0.1	~ 0.028	~ 0.065

Table 7.2: The size of RoI at each region.

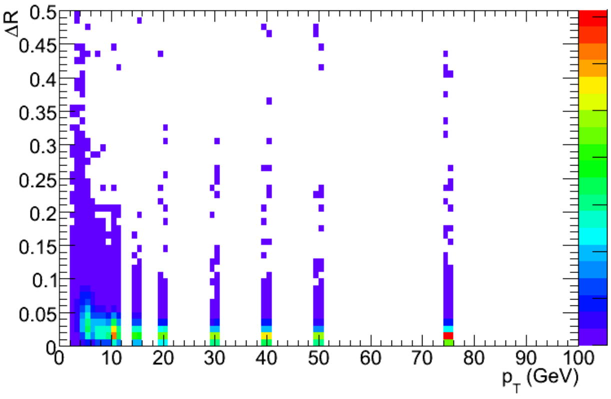

(a) At the end-cap.

(b) At the barrel.

Fig. 7.2: ΔR distributions for matched tracks as a function of p_T for the end-cap and the barrel in (a) and (b).

The error estimation of Extrapolator is checked by distributions of z defined as;

$$z = \frac{x - \mu}{\sigma}, \tag{7.1}$$

where x is the extrapolated position, μ is the exact hit position and σ is the standerd deviation given by "Extrapolator". If the error estimation is correct, z distribution should be Gaussian with the mean of zero and the variance of one. Both η and ϕ are used as the position to be tested. Figure 7.3 shows z distributions for η and ϕ with a fitted Gaussian function. In both cases, z distributions approximately represent the expected Gaussian distribution. Therefore, the estimated error given by Extrapolator is appropriate.

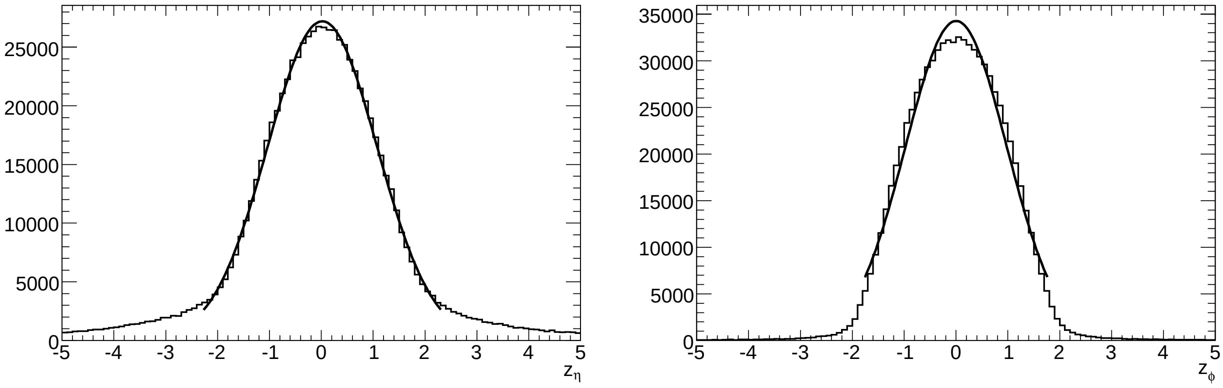

(a) Mean : 0.020, Sigma : 1.1

(b) Mean : 0.0028, Sigma : 0.98

Fig. 7.3: z distributions of η and ϕ respectively. Fit results are shown under each figure.

7.2 Measurement using calorimeter-triggered events

By using the calorimeter trigger, muons associated with hadron production can be obtained independently from the muon trigger. In this method, it is possible to obtain large number of muons.

The sample, however, contains a large fraction of background tracks in the environment at the LHC. The sources of the background are decay-in-flight muons, punch-through pions, beam halo muons and cavern background, which could cause mis-reconstruction and fake muon tracks. They could affect the efficiency measurement and optimization is necessary to increase the muon purity.

Assuming that the effect to the efficiency from such background events are negligible, the muon trigger efficiency, $\epsilon_{1\mu}$ is calculated as the ratio of the number of triggered muons ($N_{triggered}$) among the total number of reconstructed muons (N_{all}),

$$\epsilon_{1\mu} = \frac{N_{triggered}}{N_{all}}. \tag{7.2}$$

7.2.1 Performance study

In order to study the performance of this method, di-jet events passing the single jet triggers are used as both the signal and background events. The single jet trigger selects events with at least one jet with E_T over the threshold.

Monte Carlo di-jet samples

These Monte Carlo samples are produced separately in seven energy ranges of the jets. Their energy scales and crosssections are listed in Table 7.3. The average numbers of reconstructed muons per event for each sample are calculated from the Monte Carlo samples and listed in the same table. About 4.0×10^5 reconstructed muons are expected per 1 nb^{-1}. Since number of particles included in a jet typically increases with the jet energy, number of muons produced from a jet also increases with the energy.

Data set name	Jet E_T (GeV) scale	Crosssection (nb)	$N_\mu^{reconstructed}$/event
J0	10-17	17490000	0.019
J1	17-35	1377000	0.042
J2	35-70	96300	0.074
J3	70-140	6135	0.13
J4	140-280	316.8	0.20
J5	280-560	12.47	0.34
J6	560-1120	0.3445	0.58

Table 7.3: Energy scales and crosssections of di-jet samples

Jet trigger will be pre-scaled severely because the total trigger rate is limited. The number of muons expected for an integrated luminosity of 1 nb^{-1} is calculated with the pre-scale factor for the following four jet trigger menus, L1J5, L1J10, L1J18 and L1J23, where “L1” means the level-1 and the number after “J” means the E_T threshold of the jet. The planned pre-scale factor for each trigger menu is listed as in Table 7.4, where the number of muons expected for 1 nb^{-1} with pre-scale factors are also shown.

Trigger menu	L1J5	L1J10	L1J18	L1J23
Pre-scale factor	300000	42000	6000	2000
Number of muons expected at 1 nb^{-1}	2.2×10^5	1.4×10^5	2.4×10^4	1.3×10^4

Table 7.4: Pre-scale factors applied to each trigger menu and the number of muons expected at the integrated luminosity of 1 nb^{-1} after pre-scales.

Even though the pre-scale factors are very large, enough number of muons can be obtained in the case of L1J5 and L1J10. In the following study, these two trigger branches are used.

Event selection

In order to see the effect of the background, the muon trigger efficiency is evaluated by using all reconstructed muons in collected events. All di-jet samples are merged taking into account their crosssections. The result is shown in Fig. 7.4. Differences can be seen between measured trigger efficiencies and exact values from the single muon study in Section 6.1.1. The difference becomes larger with jet energy scale as shown in Fig. 7.5. One of the possible reasons of the difference is mis-reconstructed tracks in the inner and/or muon spectrometer. Since track multiplicity becomes larger with jet energy scale, it can be considered that the probability of mismatching between tracks reconstructed in the inner detector and the muon spectrometer increases. If a muon is wrongly reconstructed, the matching between the reconstructed muon and the associated RoI can not be established even if the muon is triggered. If any other particle or random hits are reconstructed as a muon, they make the muon trigger efficiency lower. So, we evaluate the probabilities of mis-reconstruction using Monte Carlo information. Here, muons are defined as mis-reconstructed unless they meet the following requirements:

$$\begin{aligned} \Delta R &\equiv \sqrt{\Delta\eta^2 + \Delta\phi^2} < 0.1, \\ \Delta p_T &\equiv |\frac{p_T^{rec} - p_T^{true}}{p_T^{true}}| < 0.2, \end{aligned} \tag{7.3}$$

where ΔR is the opening angle of the reconstructed muon and the nearest true muon, which can be found in Monte Carlo information. Figure 7.6 shows distributions of ΔR and Δp_T between the reconstructed muon and the true muon obtained using single muon Monte Carlo samples. It can be seen that most of the muons are within the range given by the equation above.

Then, the mis-reconstruction ratio (ϵ_{miss}) is defined as the ratio of the number of mis-reconstructed muons (N^{μ}_{miss}) among all reconstructed muons (N^{μ}_{all}) as:

$$\epsilon_{miss} = \frac{N^{\mu}_{miss}}{N^{\mu}_{all}}. \tag{7.4}$$

The results are summarized in Table 7.5. It can be seen that the ratio becomes larger with the jet energy scale and this result well explains the result in Fig. 7.5.

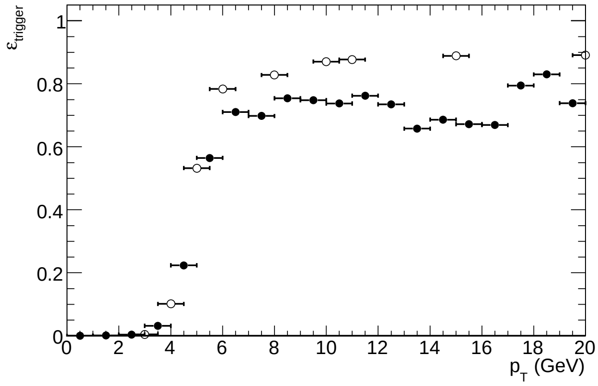

Fig. 7.4: Trigger efficiency as a function of p_T using all reconstructed muons in the events collected by the single jet trigger. Filled plots represent the efficiency from this method and open plots represent the exact one.

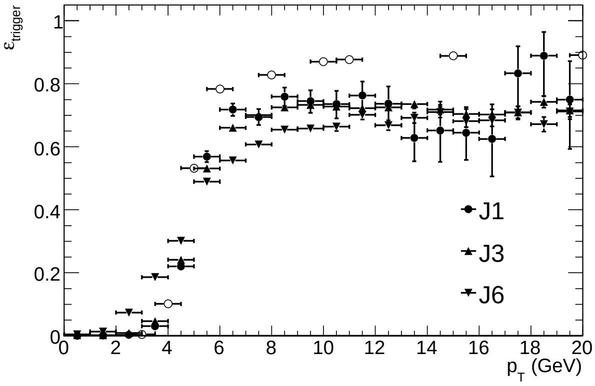

Fig. 7.5: Trigger efficiency as a function of p_T. Filled points represent the efficiency from J1, J3 and J6 samples, respectively. The exact values are also plotted.

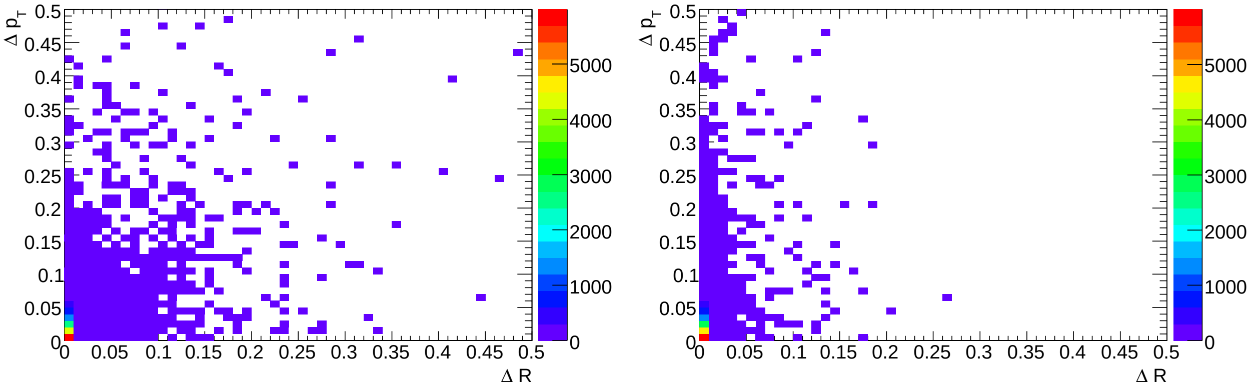

Fig. 7.6: Distributions of ΔR and Δp_T between a reconstructed muon and a true muon obtained using the single muon Monte Carlo samples. The left figure is for muons with p_T =6 GeV and the right one is for muons with p_T = 20 GeV.

Data set name	J0	J1	J2	J3	J4	J5	J6
ε_{miss} [%]	53.8	54.6	54.3	56.3	61.5	69.8	80.1

Table 7.5: The mis-reconstruction ratio in each di-jet sample.

To get rid of the mis-reconstructed muons, the following three variables are used. The first is a boolean flag indicating whether the reconstructed track is combined or not. Here, a “combined” track is defined as the track reconstructed in both the muon spectrometer and the inner detector with a connected trajectory. The second is the reduced χ^2 in the track fitting. These two parameters describe the quality of reconstruction. The last variable is the isolation energy of tracks. It is calculated by summing momentum of tracks within a cone around the muon track at the interaction point. The size of the cone is set to be 0.4 for the η-ϕ space. Distributions of these three variables are shown in Fig. 7.7, where J1, J3 and J6 samples are used for comparison. In each figure, distributions of well reconstructed muons and mis-reconstructed muons are compared. Clear difference can be seen between two distributions. As a result, reconstructed tracks are used for the measurement only if they are combined tracks with reduced $\chi^2 < 10$ and the isolation energy < 10 GeV. After applying these selections, the mis-reconstruction ratio is reduced by about a half as shown in Table 7.6.

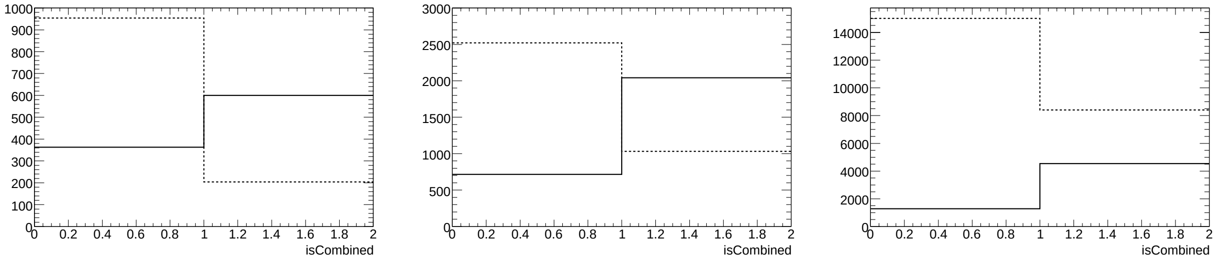

(a) "isCombined" from J1 sample. (b) "isCombined" from J3 sample. (c) "isCombined" from J6 sample.

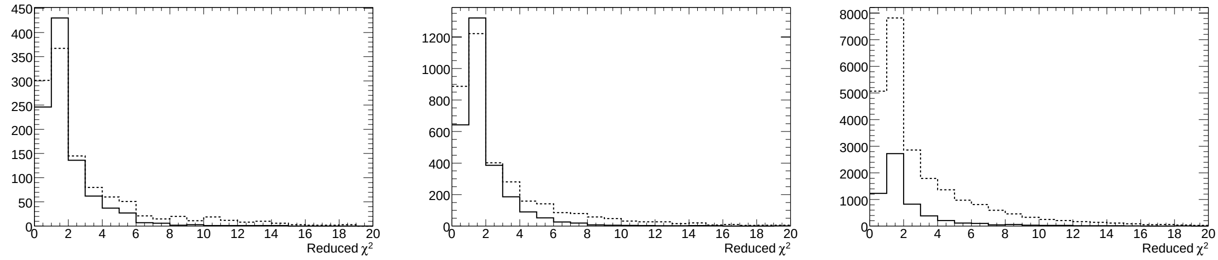

(d) Reduced χ^2 from J1 sample. (e) Reduced χ^2 from J3 sample. (f) Reduced χ^2 from J6 sample.

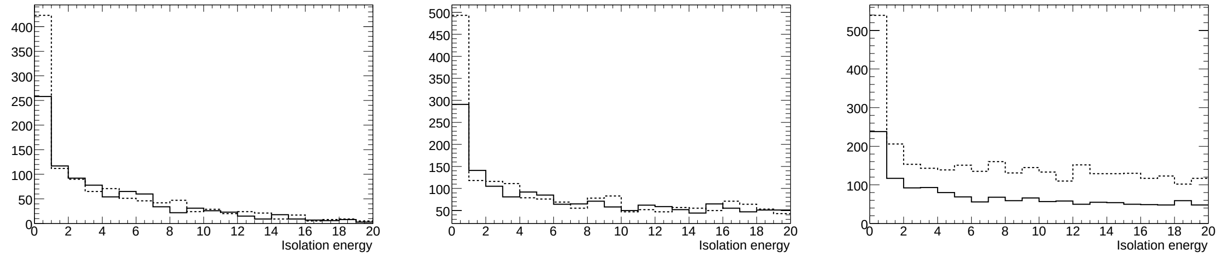

(g) Isolation energy from J1 sample. (h) Isolation energy from J3 sample. (i) Isolation energy from J6 sample.

Fig. 7.7: Distributions of well-reconstructed and mis-reconstructed muons. Dashed histograms are of mis-reconstructed muons and solid ones are of well-reconstructed muons.

Data set name	J0	J1	J2	J3	J4	J5	J6
ε_{miss} [%]	21.5	24.5	23.7	25.4	26.6	34.6	49.8

Table 7.6: The mis-reconstruction ratio in each di-jet sample after applying the track selection.

Result

After applying the track selection, the muon trigger efficiency as a function of p_T of reconstructed muons are measured. Obtained efficiencies are fitted by the following function:

$$\epsilon_{1\mu} = \frac{A}{1 + e^{-a(p_T^{\mu} - b)}}, \tag{7.5}$$

where A, a and b are the fit parameters. The results are shown in Fig. 7.8 and summarized in Table 7.7. Fluctuations appeared in Fig. 7.8 are derived from the statistical uncertainty of the Monte Carlo simulation. Typically about 10 % of statistical uncertainty is included in the efficiency for high-p_T regions (p_T > 10 GeV).

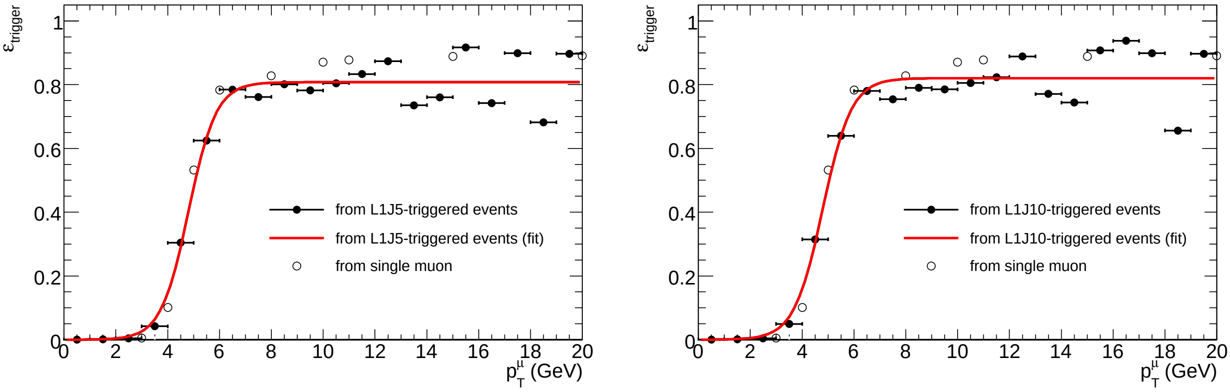

(a) (b)

Fig. 7.8: The muon trigger efficiency as a function of p_T with the track selections fitted by Eq. 7.5. Open points represent the exact values. (a) is the case of using L1J5 trigger and (b) is using L1J10.

	L1J5	L1J10	exact value
Trigger efficiency at the threshold (6 GeV)	74.8 (%)	74.5	79.0
Trigger efficiency at the plateau (> 10 GeV)	82.9	83.9	88.9

Table 7.7: Fit results of the muon trigger efficiency obtained from calorimeter-triggered events. Exact values from single muon samples are also shown.

As you can see from Table 7.7, although the muon trigger efficiency is still somewhat lower than the exact values, it can be measured within an error of ∼ 5 % using this method. It is enough to find out a problem of the system and this method is useful at the early stage of the data taking. However, this method largely depends on the performance of the reconstruction and the background environment, and the systematic uncertainty included in the simulation is large. Because of the presence of background, this method is not appropriate for the precise measurement of the muon trigger efficiency.

7.3 Measurement using muon-triggered events

While quick measurements can be done by using calorimeter-triggered events, we need efficiency measurements not affected by quality of reconstruction, uncertainties in simulation and amount of background. Such high-precision efficiency determination is necessary for the cross-section measurements and detailed study of the detectors. It can be achieved by using events with di-muon final states, which can be triggered by the single muon trigger. This method is called "tag-and-probe" method. A schematic view of the method is shown in Fig. 7.9 and is detailed below:

- First, each reconstructed muon is examined whether it is triggered or not by using the matching criteria explained in the first section of this chapter. If it is triggered, it is assigned as a tagged muon;
- Second, another muon from the same event is searched for. In order to obtain a prompt muon and distinguish from a decay of the parent particle, it is examined further by reconstructing the invariant mass of the muon and the tagged one. If the second muon is found, it is named a probe muon;
- Finally, using the probe muon, the muon trigger efficiency is calculated.

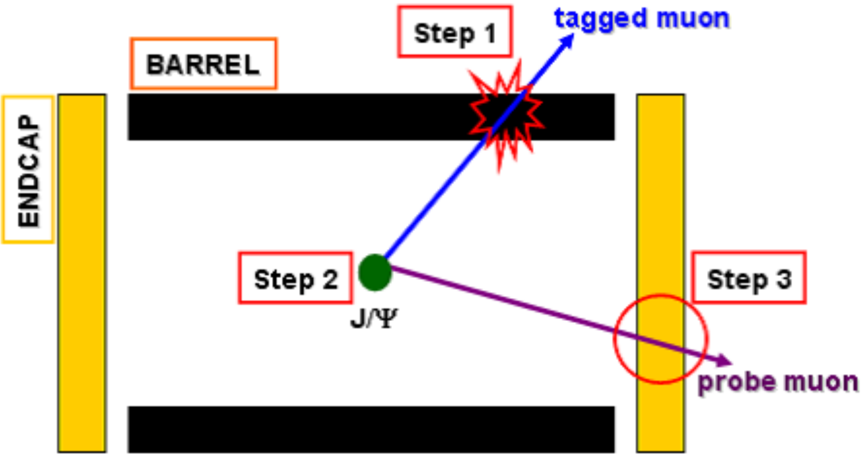

Fig. 7.9: Schematic view of the tag-and-probe method.

The muon trigger efficiency, $\epsilon_{1\mu}$ is calculated as the ratio between the number of probe muons which were triggered ($N_{probe\&triggered}$) among the total number of probe muons (N_{probe}),

$$\epsilon_{1\mu} = \frac{N_{probe\&triggered}}{N_{probe}}. \tag{7.6}$$

Efficiencies are also calculated as a function of kinematic variables of muons, p_T, η and ϕ. Sharp changes are expected to be observed in the efficiency due to structual features such as the support structures of the detector.

To measure the trigger efficiency for low-p_T muons, the decay muons from J/ψ, $J/\psi \to \mu\mu$ events, are used. Since enough statistics can be obtained from $J/\psi \to \mu\mu$ events even in low luminosity runs, the process is widely used not only for the trigger efficiency measurement but also for detector alignment, reconstruction efficiency measurement and energy calibration of calorimeters. Events with J/ψ are also important for b physics. When the beam energy and intensity become high enough to produce high mass states copiously, $Z \to \mu\mu$ events can also be used. With this process, the muon trigger efficiency for higher-p_T region can be measured.

By using these two processes, the trigger efficiency can be measured for a wide p_T range. Monte Carlo samples are used again to study the performance of the tag-and-probe method. The details of these samples and the event selections are explained below.

7.3.1 Measurement using J/ψ events

Monte Carlo J/ψ samples

Two sets of J/ψ samples are used. One includes J/ψ from b quark decays in $b\bar{b}$ pair-production and the other includes J/ψ directly produced from pp collision. Crosssection of these two processes are about 11 nb and 22 nb, respectively. It is required that at least one J/ψ in each event decays into a muon pair. The following conditions are required in generator level to efficiently generate the events:

- one muon with p_T more than 6 GeV in $|\eta| < 2.4$;
- another muon with p_T more than 4 GeV in $|\eta| < 2.4$.

Figure 7.10 and 7.11 show distributions of kinematic variables of J/ψs and muons in each sample. The generator level cuts above can clearly be seen. It can be said from Fig. 7.11-(a) that these samples are appropriate to measure the trigger efficiency for low-p_T region up to ~15 GeV and, from Fig. 7.11-(b) and (c), we can obtain muons in the whole detector region.

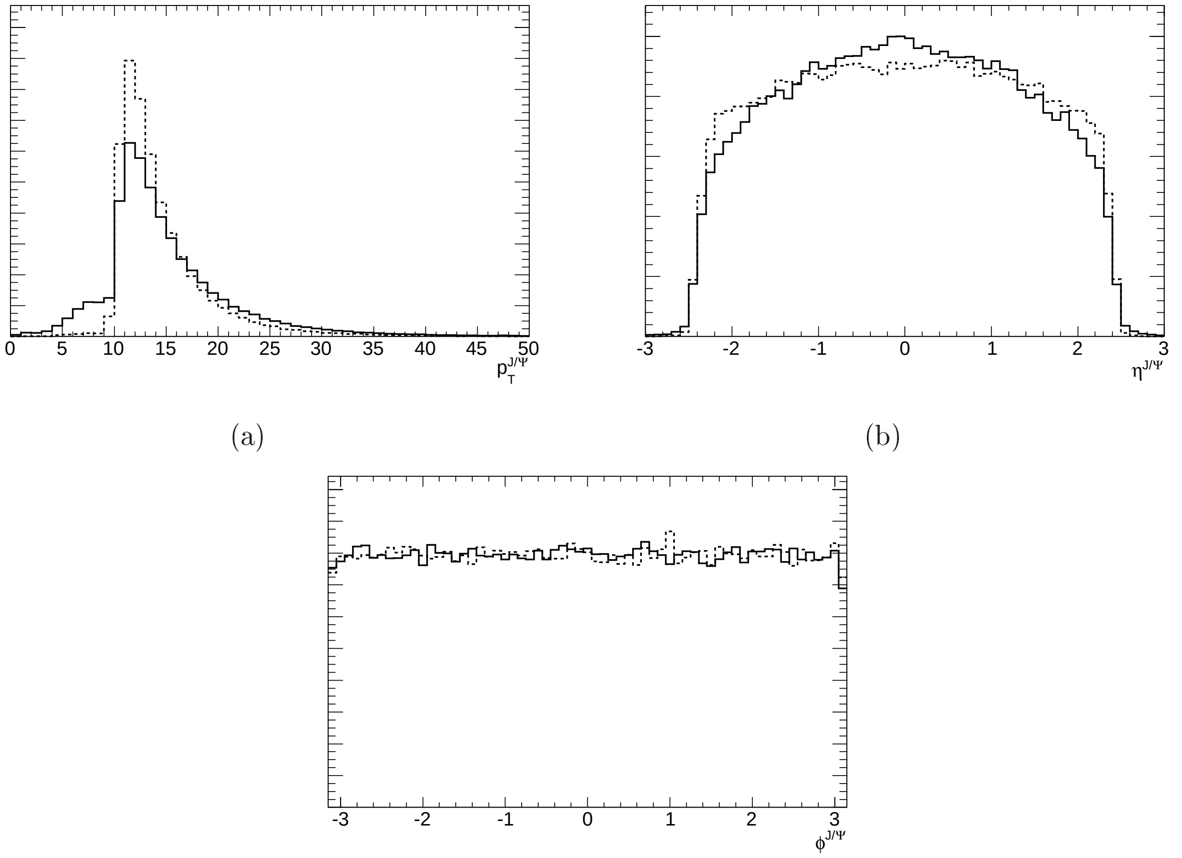

(a)

(b)

(c)

Fig. 7.10: Distributions of kinematic variables of J/ψs. Solid histograms represent distributions of J/ψs from $b\bar{b}$ pair production, while dashed histograms do those from direct production of J/ψ from pp-collision. All distributions are area-normalized to 1.

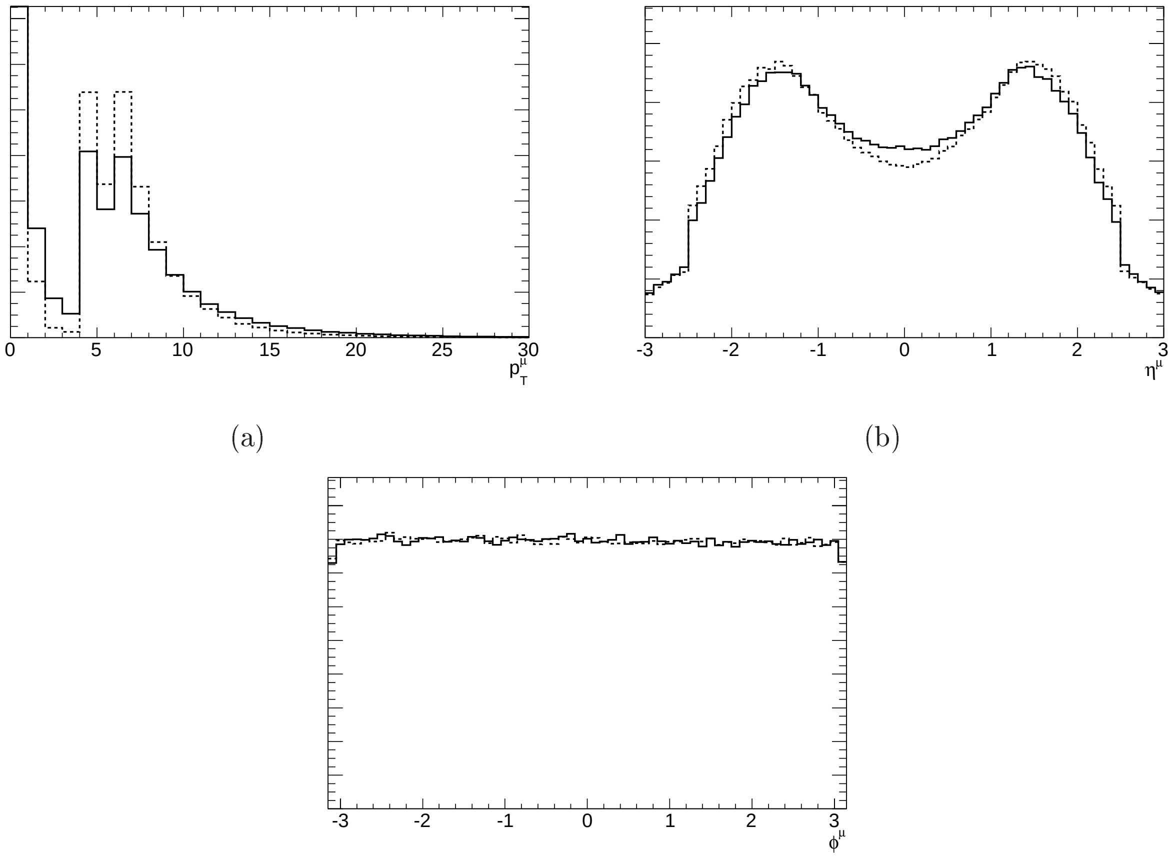

(a)

(b)

(c)

Fig. 7.11: Distributions of kinematic variables of muons in J/ψ events. Solid histograms represent distributions of them in J/ψ events from $b\bar{b}$ pair production, while dashed histograms do those events from direct production of J/ψ from pp-collision. All distributions are area-normalized to 1.

Event selection

Following requirements are imposed for selecting J/ψ events.

Mass cut	2.88 GeV< $M_{\mu\mu}$ <3.3 GeV
Track type	combined track
Separation cut	$\Delta R_{\mu_1\mu_2} > \sum \Delta R^{\mu_i}_{match}$

Table 7.8: Event selections for $J/\psi \to \mu\mu$ events.

The mass range is determined from the reconstructed invariant mass distribution shown in Fig. 7.3.1. We take 3σ value of the distribution to collect J/ψ events. Only combined tracks explained in Section 5.2 are used for the measurement. In order to further reduce the mismatching between muons and RoIs, which may closely be located in space, only the events are used where the opening angle of the two decay muons at the pivot plane is greater than the sum of the limit of the matching ΔR of the two. Applying these selections, tagged muons are selected using the matching criteria explained in Section 7.1, then, the second muons from J/ψ are looked for by the mass cut. The fraction of remaining events after each cut is summarized in Table 7.9. Note that the generator level cuts are included in these values. After these selections, about 20 % of $J/\psi \to \mu\mu$ events remain. The kinematic variables of the probe muons are shown in Fig. 7.13 are obtained. Some dips can be seen around $\phi \sim -1.6$ in Fig. 7.13-(d) and $\eta \sim 0$ and ± 1 in Fig. 7.13-(e). The dips at $\phi \sim -1.6$ and $\eta \sim 0$ are due to the support structures of the ATLAS detector, where there are no muon detectors. The regions, $\eta \sim \pm 1$, are the overlap regions between the end-cap and the barrel, where the magnetic field is very complex. In such regions, trajectory measurements for low-p_T muons can not be done correctly. However, there still exist probe muons even at the worst point, and the muon trigger efficiency can be measured for low-p_T muons at both the end-cap and the barrel with this process.

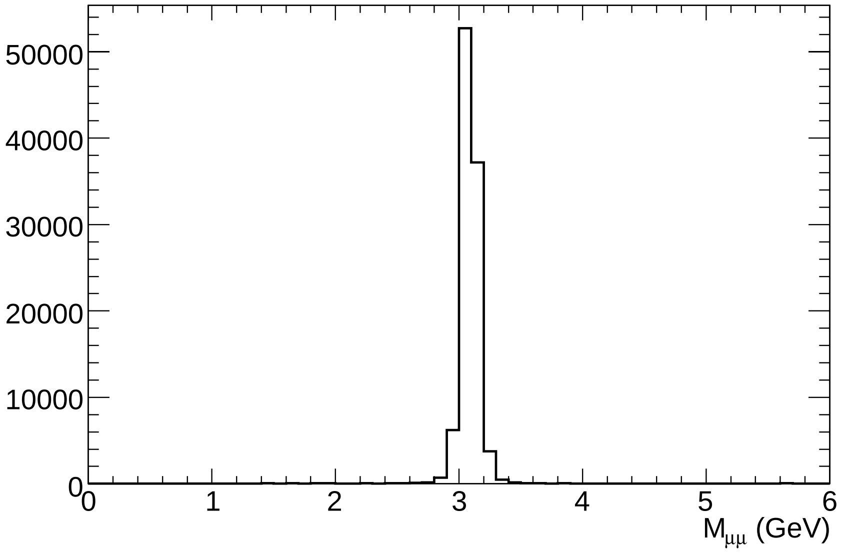

Fig. 7.12: Invariant mass distributions of two reconstructed muons.

	$pp \to J/\psi \to \mu\mu$	$bb \to J/\psi \to \mu\mu$
Mass cut	83.5 (%)	77.3
Combined muon selection	69.8	64.7
Separation cut	22.1	19.8
Probe muon at the end-cap	5.3	3.9
Probe muon at the barrel	15.7	15.0

Table 7.9: Percentage of remaining events after each cut to the total number of events.

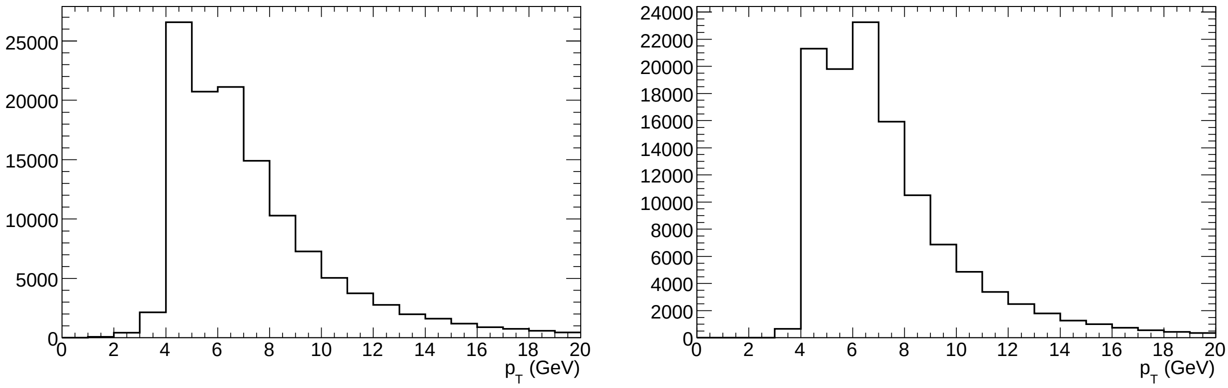

(a) p_T of the end-cap muons

(b) p_T of the barrel muons

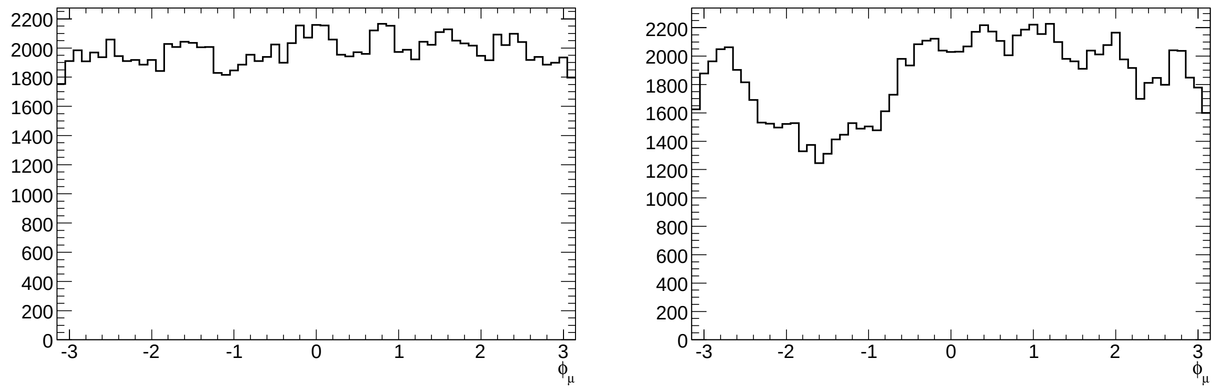

(c) ϕ of the end-cap muons

(d) ϕ of the barrel muons

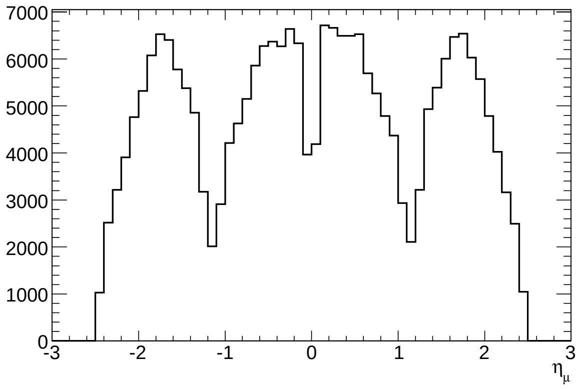

(e) η of muons

Fig. 7.13: Distributions of kinematic variables of probe muons from J/ψ.

Results

The muon trigger efficiency is measured as a function of p_T, η and ϕ of reconstructed muons for the end-cap and the barrel, respectively. The results are shown in Fig. 7.14. The efficiencies for both the barrel and the end-cap rise around the threshold similar to that for the single muon samples. The position dependence can also be seen for both η and ϕ. Note that the p_T dependence is included there. The efficiency drops around the structures for both η and ϕ. In addition, it can be seen that the efficiency drops around the toroid coils, where complex magnetic field is produced and trajectories of low-p_T muons can not be completely followed. These results are compared with those from the single muon samples and those from $Z \to \mu\mu$ events described in Section 7.3.3.

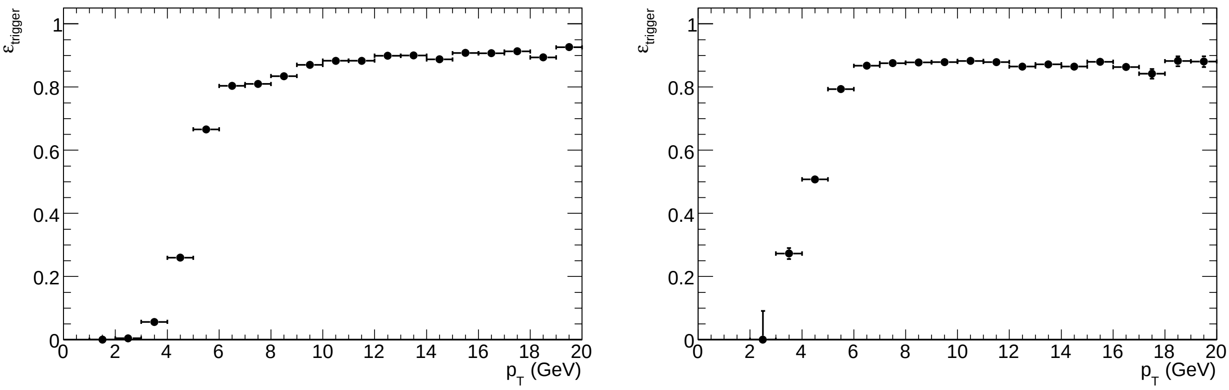

(a) Trigger efficiency vs. p_T^μ for the end-cap.

(b) Trigger efficiency vs. p_T^μ for the barrel.

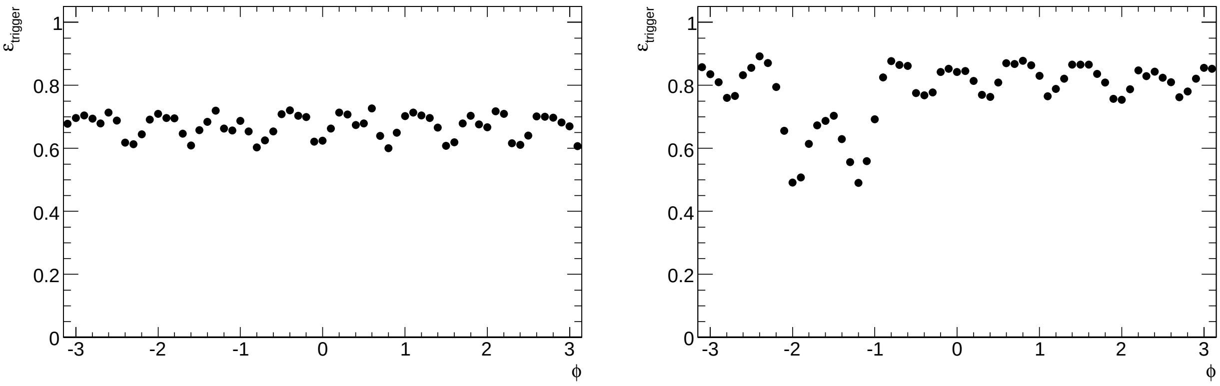

(c) Trigger efficiency vs. ϕ^μ for the end-cap.

(d) Trigger efficiency vs. ϕ^μ for the barrel.

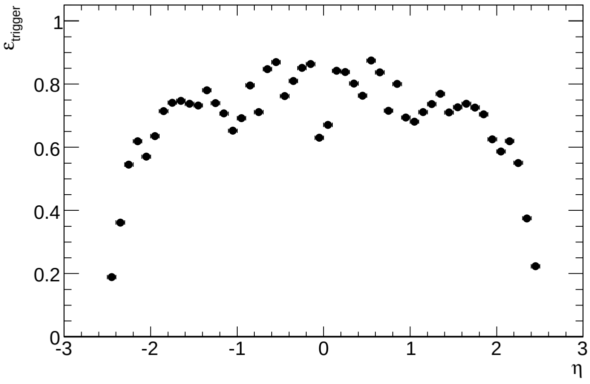

(e) Trigger efficiency vs. η^μ for overall.

Fig. 7.14: Trigger efficiencies from $J/\psi \to \mu\mu$ events.

7.3.2 Measurement using Z events

Monte Carlo Z samples

We use $Z \to \mu\mu$ samples where the following cuts are applied in event generation:

- the invariant mass between the two muons should be more than 60 GeV;
- there should be at least one muon with p_T more than 5 GeV in $|\eta| < 2.8$.

Kinematic variables of Z bosons and muons are shown in Fig. 7.15 and 7.16. The crosssection of this process after the generation cut is about 1662 pb. This sample seems to be appropriate for high-p_T region measurement as shown in Fig. 7.16-(a) and whole detector regions can be covered as shown in Fig. 7.16-(b) and (c).

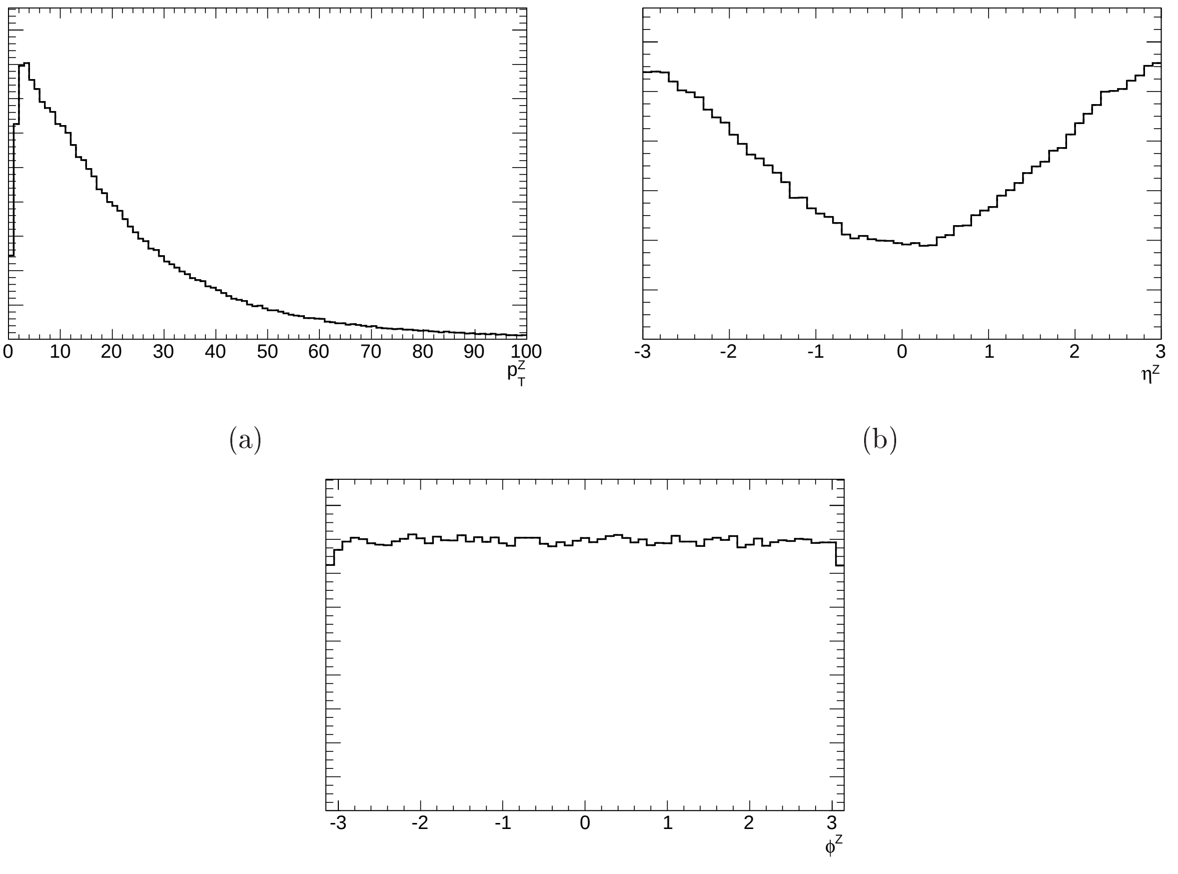

(a)

(b)

(c)

Fig. 7.15: Distributions of kinematic variables of Z bosons. Figure (a), (b) and (c) represent p_T^Z , η^Z and ϕ^Z distributions, respectively.

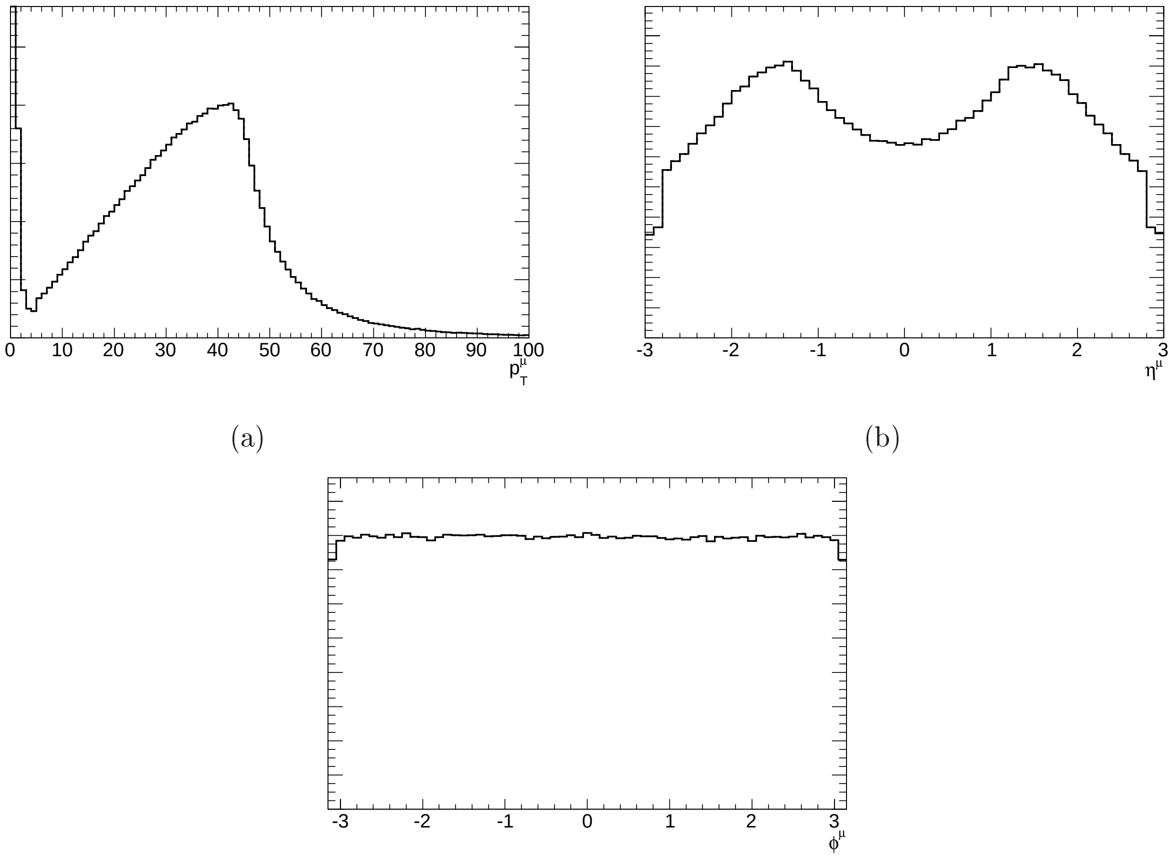

(a)

(b)

(c)

Fig. 7.16: Distributions of kinematic variables of muons from Z. Figure (a), (b) and (c) represent p_T^μ , η^μ and ϕ^μ distributions, respectively. The generator-level cut appears in Fig. (b), while whole detector regions of $|\eta| < 2.4$ are covered.

Event selection

In order to reduce background, the following cuts are applied to each event.

Mass cut	81.19GeV < $M_{\mu\mu}$ < 101.19GeV
Track type	combined track
Momentum cut	$p_T^\mu > 15$GeV

Table 7.10: Event selections for $Z \rightarrow \mu\mu$ events.

As opposed to the case of J/ψ, background environment after the Z selection from two muons is much lower. In addition, the mass distribution is determined by the Z mass natural width, not by the momentum resolution of the muon. The mass cut range is determined to be between ± 10 GeV from Z mass. Only combined muons are used for the measurement. Note that we use muons with p_T more than 15 GeV and all tracks are supposed to be straight: the matching between muons and RoIs is performed without using “Extrapolator”. The limit of matching ΔR is fixed to be 0.15. With this limit, more than 99.9 % of triggered muons with p_T more than 15 GeV can be selected. Both tagged muons are found and probe muons are selected with the event selection described above. Percentage of remaining events after each selection is summarized in Table 7.11. After these selections, we obtain probe muons with those kinematics as shown in Fig. 7.18. We can collect ~40 % of $Z \to \mu\mu$ events. With this process, the muon trigger efficiency can be measured, especially for high-p_T region ($p_T > 15\text{GeV}$) in both the end-cap and the barrel region.

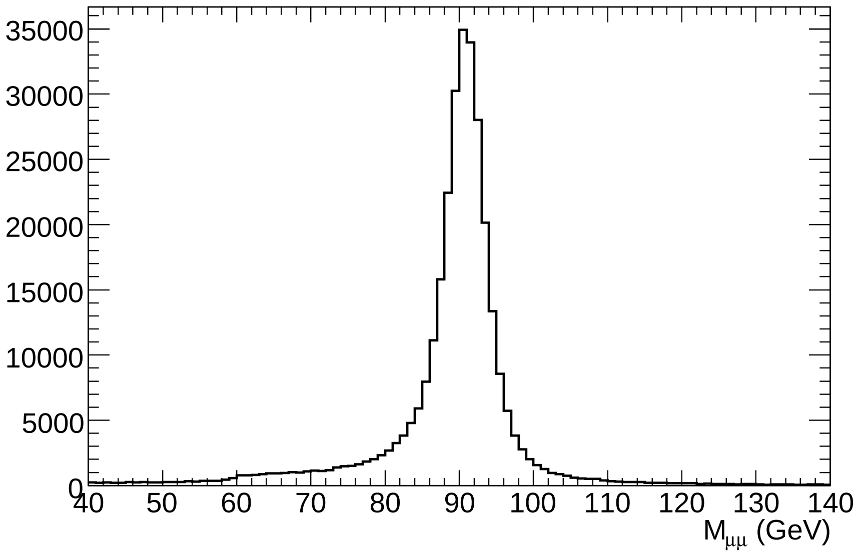

Fig. 7.17: Invariant mass distribution of two reconstructed muons in Z events.

Mass cut	47.1
Combined muon selection	42.0
Probe muon at the end-cap	27.3
Probe muon at the barrel	28.0

Table 7.11: Percentage of remaining events after each cut to the total number of events.

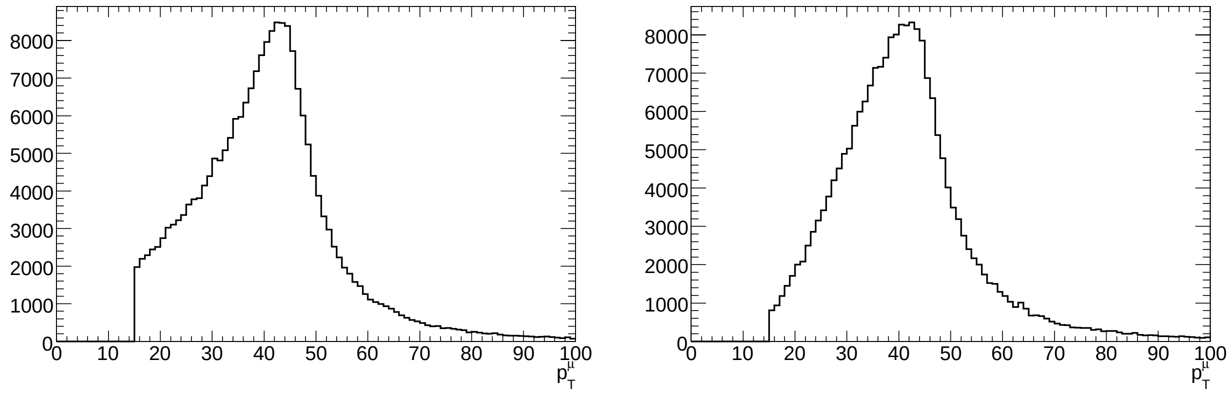

(a) p_T at the end-cap (b) p_T at the barrel

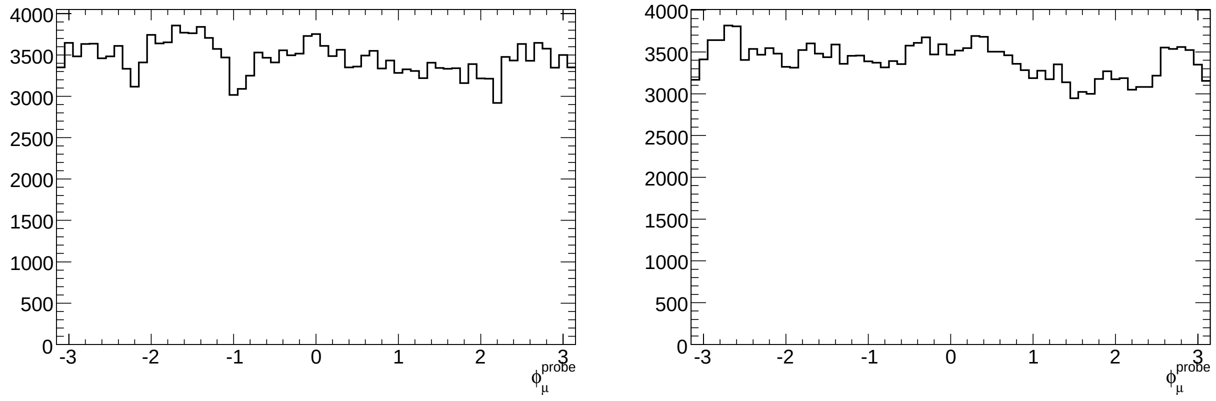

(c) ϕ at the end-cap (d) ϕ at the barrel

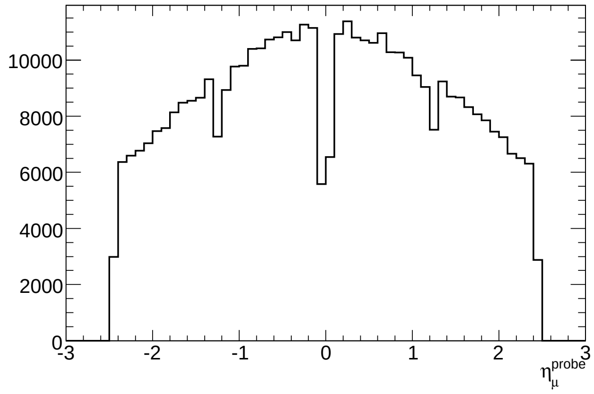

(e) η

Fig. 7.18: Probe muon kinematics from Z.

Results

The muon trigger efficiency is measured as a function of p_T, η and ϕ of reconstructed muons for the end-cap and the barrel, respectively. The results are shown in Fig. 7.19. The efficiencies for both the barrel and the end-cap are nearly flat for high-p_T muons like that from the single muon samples. There is little ϕ dependence of the efficiency for the end-cap, while there can be seen the structural effects in ϕ for the barrel and in η for both regions. These results are evaluated in the next section with those from $J/\psi \to \mu\mu$ events.

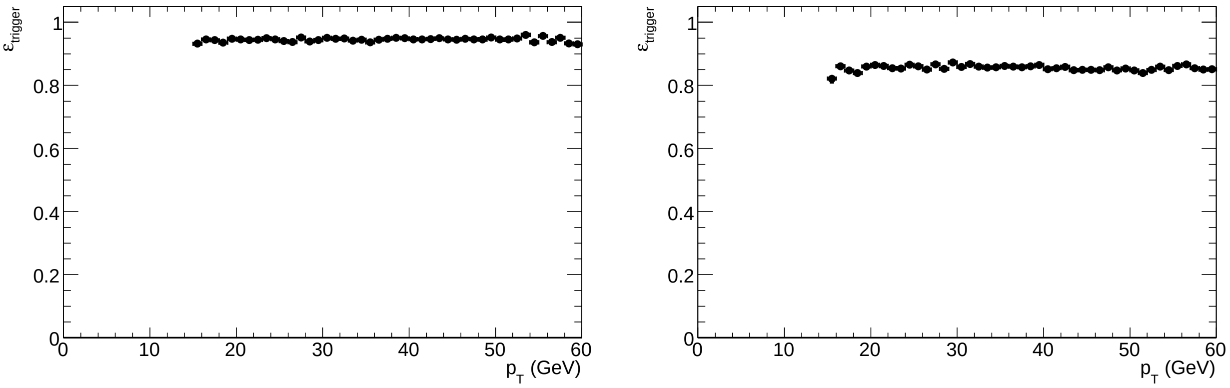

(a) Trigger efficiency vs. p_T^μ for the end-cap. (b) Trigger efficiency vs. p_T^μ for the barrel.

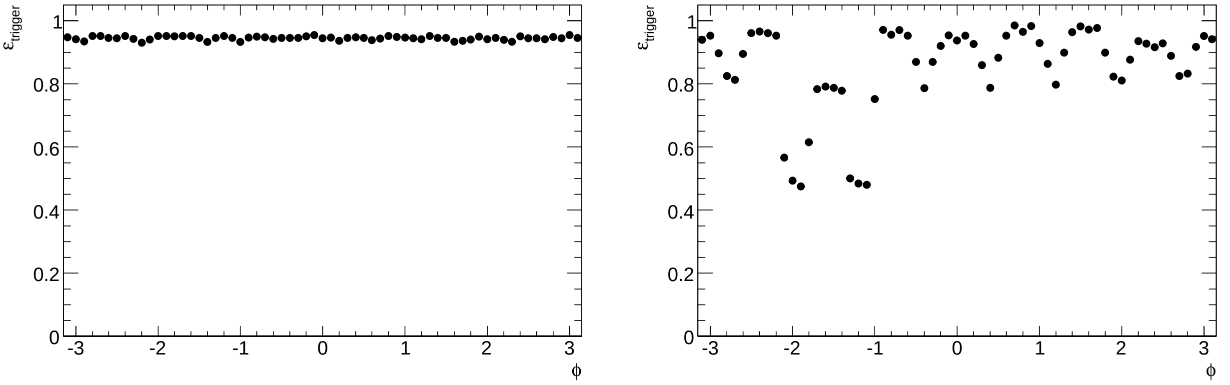

(c) Trigger efficiency vs. ϕ^μ for the end-cap. (d) Trigger efficiency vs. ϕ^μ for the barrel.

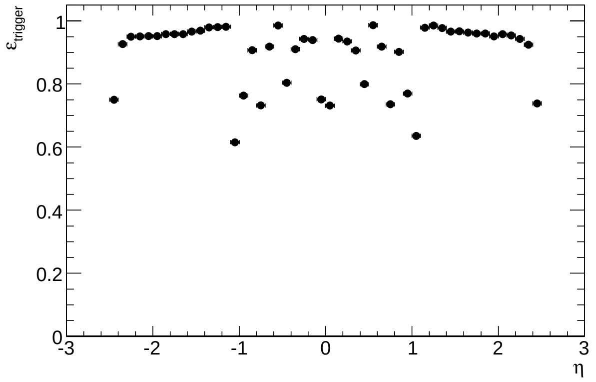

(e) Trigger efficiency vs. η^μ for overall.

Fig. 7.19: Trigger efficiencies from $Z \to \mu\mu$ events.

7.3.3 Expected performance of tag-and-probe method

Performance of the tag-and-probe method with J/ψ and Z events is evaluated by comparing with the exact values from the single muon sample. Here, the muon trigger efficiency as a function of p_T is fitted by Eq. 7.5. The results are shown in Fig. 7.20 and Table 7.12. The result from Z events is used to evaluate the result at the plateau; the result form J/ψ events around the threshold. The fit parameter A is obtained from the result from Z events; a and b from J/ψ events. The difference of the efficiencies is less than 5 % in the turn-on region ($4\text{GeV} < \mathrm{p_T} < 8\text{GeV}$) and becomes smaller as

p_T increases. At the plateau ($p_T > 8$GeV), the difference is about 1 %. The difference is considered to be derived from the accuracy of the matching between the muon and the RoI, and from the muon reconstruction efficiency as described in Chapter 5.

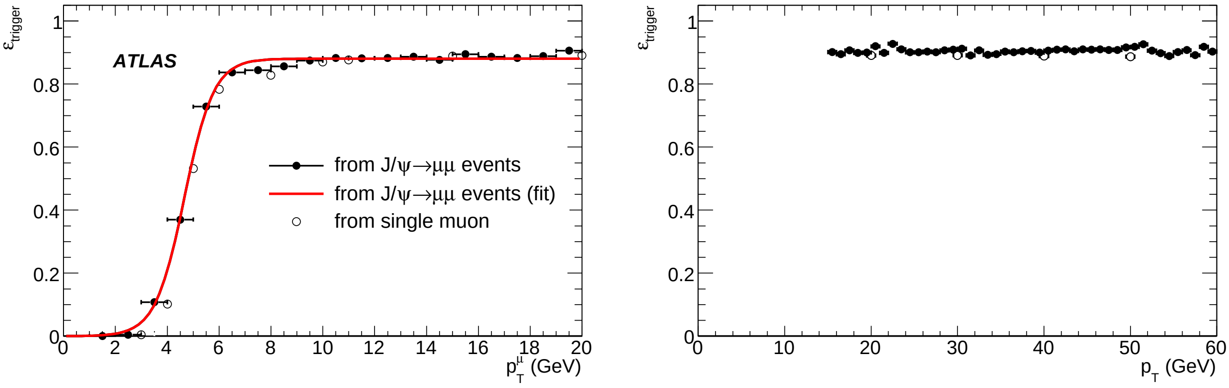

(a) (b)

Fig. 7.20: Muon trigger efficiencies as a function of p_T: (a) from $J/\psi \to \mu\mu$ events and (b) from $Z \to \mu\mu$ events. Filled circles in both figure show the overall muon trigger efficiency from the tag-and-probe method; open circles are from single muons. The result of the fit (see text) is also shown.

	A	a	b	$\epsilon_{trigger}$ at the threshold	$\epsilon_{trigger}$ at the plateau
tag-and-probe	0.91 ± 0.001	2.0 ± 0.5	4.4 ± 0.2	77.9 %	90.6 %
exact value	0.89 ± 0.001	2.6 ± 0.6	4.8 ± 0.2	79.0 %	88.9 %

Table 7.12: Fit results of the muon trigger efficiencies obtained from J/ψ and Z events using tag-and-probe method. Expected values are also represented.

Another key issue for the efficiency measurement is the precision due to limited statistics. The statistical uncertainty of the efficiency measurement as a function of the integrated luminosity is therefore evaluated. Figure 7.21 shows the ratio of the statistical error of the trigger efficiency to the efficiency itself as a function of the integrated luminosity. The ratio for the efficiency at the threshold (6GeV) is calculated from the result of J/ψ, while that at the plateau is calculated from the result of Z. It is found that the muon trigger efficiency, integrated over the whole angular range, at the threshold can be measured within an error of about 1 % and that at the plateau can be measured within an error of 0.1 % for an integrated luminosity of 100 pb^{-1}. Note that we include no background effects, which are studied in the following.

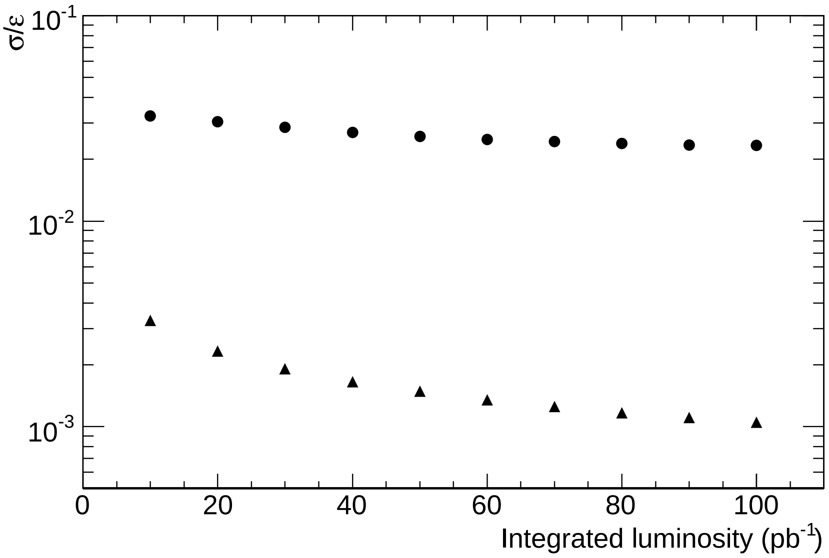

Fig. 7.21: Expected accuracy of the muon trigger efficiencies, integrated over the whole angular range, using the tag-and-probe method. Circles show the value for the efficiencies at the threshold (6GeV) from the J/ψ result and triangles show the value for the efficiencies at the plateau from the Z result.

Background effects

Fake J/ψs or Z bosons might be selected from accidental match of two muons from background sources. These muons may affect the trigger efficiency measurement and the effects should be estimated. The following Monte Carlo samples are used for this purpose:

- For J/ψ study,
  - $b\bar{b} \rightarrow \mu + X$ (6145 nb)
- For Z study,
  - $W \rightarrow \mu + \nu$ (13861 pb)
  - $Z \rightarrow \tau + \tau$ (1639 pb)
  - $t\bar{t} \rightarrow l + \nu + X$ (461 pb)
  - $b\bar{b} \rightarrow \mu + \mu + X$ (110500 pb)

where crosssections for each process are shown in brackets.

Figure 7.22 represents distributions of the invariant mass between two muons in each event. After applying the mass window explained in the previous sections, the remaining fraction of these background sources are 19.6 % for J/ψ and 11.3 % for Z.

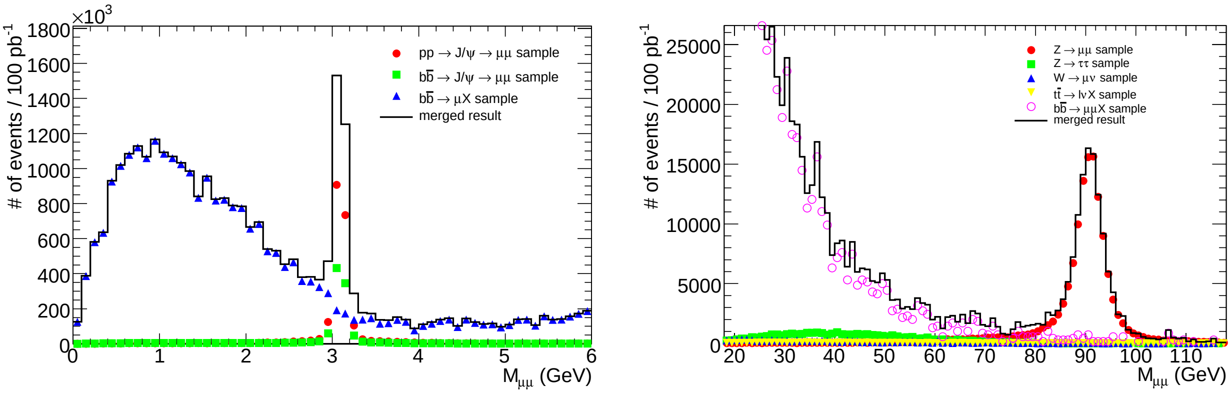

(a) (b)

Fig. 7.22: Distributions of the invariant mass between two reconstructed muons. All background samples listed above are included. (a) J/ψ and (b) Z.

The trigger efficiency is measured from the background samples applying the same event selections above. The results are shown in Fig. 7.23 together with the fitted function of the trigger efficiency. The results from the di-muon events and those with background events are also shown there. The statistics of the available background samples is small, leading to large statistical uncertainties on the muon trigger efficiencies, which are of the order of 20 % for most of the p_T regions. This uncertainties result in the fluctuations appeared in the merged muon trigger efficiencies.

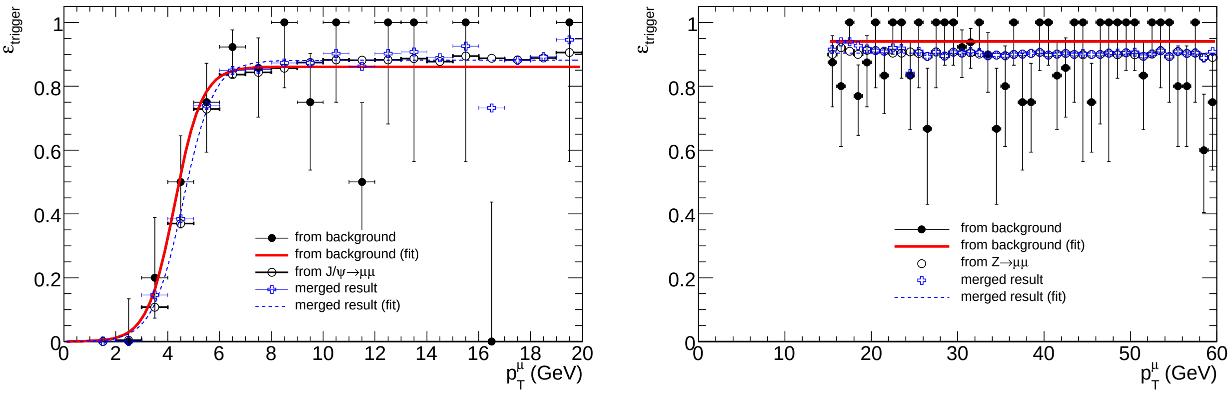

(a) (b)

Fig. 7.23: The muon trigger efficiency as a function of p_T with and without background. Filled plots in each figure show the efficiency with background and open plots show that without background. (a) is the case of J/ψ and (b) is the case of Z.

Table 7.13 shows the fit results of the muon trigger efficiencies from the di-muon events, from the di-muon events with backgrounds and from the background events. It can be seen that the differences between the results from the di-muon events and the backgrounds are a few % for all p_T regions. They are well in agreement, within statistical errors, with the efficiency from the signal samples. When we merge the results taking into account their crosssections, the differences become smaller than 0.5 % at the plateau and a few percent around the threshold. Therefore, it can be concluded that the background gives negligible contribution at the plateau and only gives small increase of the efficiency in the threshold region.

	A	a	b	$\epsilon_{trigger}$ at the threshold	$\epsilon_{trigger}$ at the plateau
from di-muon events	0.91 ± 0.001	2.0 ± 0.5	4.4 ± 0.2	77.9 %	90.6 %
from background events	0.94 ± 0.014	1.9 ± 0.9	4.3 ± 0.4	82.9 %	93.7 %
from merged events	0.91 ± 0.001	2.6 ± 0.7	4.8 ± 0.2	80.4 %	90.9 %

Table 7.13: Fit results of the muon trigger efficiencies with and without background.

8 Di-muon trigger efficiency for $J/\psi \rightarrow \mu\mu$ events

In the previous chapter, the methods to measure the muon trigger efficiency from collision data are described. The muon trigger efficiency can be measured using the tag-and-probe method with statistical uncertainty of ~1 % and systematic uncertainty of ~1 % for an integrated luminosity of 100 pb^{-1}.

If the level-1 single muon trigger rate is much larger than expected, it will be pre-scaled. In such a case, the level-1 di-muon trigger, which requires at least two muons with p_T over the threshold, can still be used to collect di-muon final states needed for e.g. B physics studies. The di-muon trigger is expected to be able to collect events including low-p_T muons with stable trigger rate: at high luminosity runs, the single muon trigger with low threshold will be pre-scaled and instead the di-muon trigger plays an important role to collect events with low-p_T muons. Therefore, as same as the muon trigger efficiency, it is important to measure the di-muon trigger efficiency from collision data. The di-muon trigger efficiency, $\epsilon_{2\mu}$ can be calculated as the product of the two muon trigger efficiencies, $\epsilon_{1\mu}$ for each muon, assuming that there is no correlation between the muon trigger efficiencies for the two, as:

$$\epsilon_{2\mu} = \epsilon_{1\mu}(p_T^{\mu_1}, \eta^{\mu_1}, \phi^{\mu_1}) \times \epsilon_{1\mu}(p_T^{\mu_2}, \eta^{\mu_2}, \phi^{\mu_2}). \tag{8.1}$$

$\epsilon_{1\mu}(p_T^{\mu}, \eta^{\mu}, \phi^{\mu})$ can be obtained from the muon trigger efficiency in detail as a function of p_T, η and ϕ of muons by the tag-and-probe method. In this chapter, we examine the method and evaluate its performance by comparing the results with the trigger-level output of the level-1 di-muon trigger using $J/\psi \rightarrow \mu\mu$ events.

8.1 Trigger efficiency map

To calculate the trigger efficiency for di-muon final states using Eq. 8.1, the muon trigger efficiency curves obtained by the tag and probe method are parameterized in each small region. In this study, the detector is divided into 10×10 regions of η and ϕ for the barrel ($|\eta| < 1.05$). For the end-cap ($1.05 < |\eta| < 2.4$), we assume that there is a complete symmetry between octants and divide one octant into 10×6 regions of η and ϕ. The trigger efficiency curves as a function of p_T are obtained in each region and fitted by the following function:

$$\epsilon_{1\mu} = \frac{A}{1 + e^{-a(p_T^{\mu} - b)}}, \tag{8.2}$$

which is the same as used in the previous chapter. Figure 8.1 and 8.2 show the results of each of the divided range using about 20 pb^{-1} of luminosity of J/ψ events with fitted curves. It is shown that the efficiency curves behave differently in each region but in a smooth way, except for a small region around $|\eta| \sim 0.725$ and $\phi \sim -1.6$, where the efficiency is very low due to the absence of the detectors. Then, the values of A, a and b in a given point in (p_T, η, ϕ) is obtained by linear interpolation as shown in Fig. 8.3 and 8.4 for the end-cap and the barrel respectively. They are collectively named "trigger efficiency map". Using the map, $\epsilon_{1\mu}$ in Eq. 8.1 can be obtained for muons at given kinematic points.

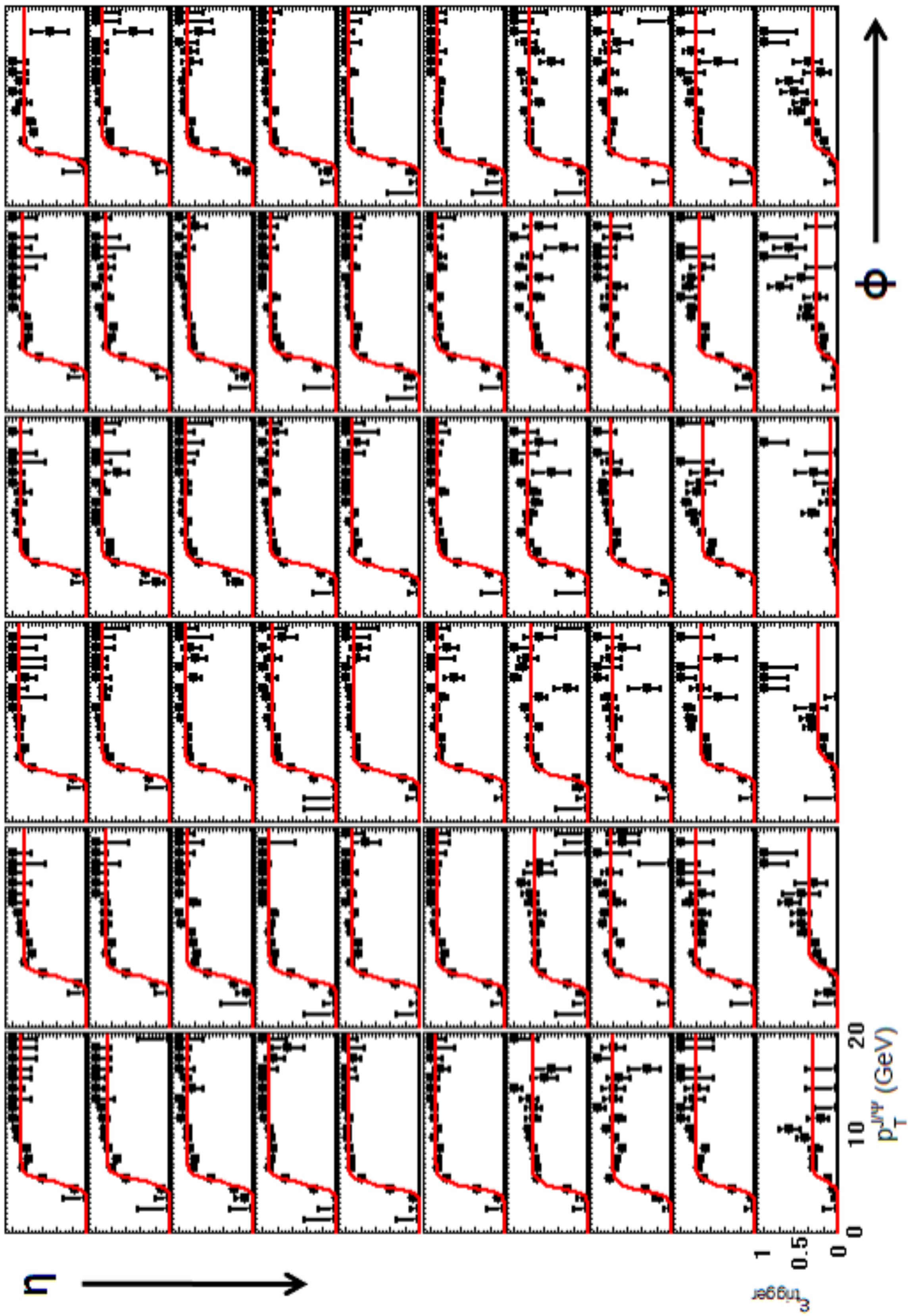

Fig. 8.1: Trigger efficiencies for each region in the end-cap. The x-axis in each graph is p_T^μ in GeV from 0 GeV to 20 GeV. The y-axis means the trigger efficiency from 0 to 1.1. The top left corner represents the smallest point in η and ϕ. η increases with line number and ϕ increases with row number.

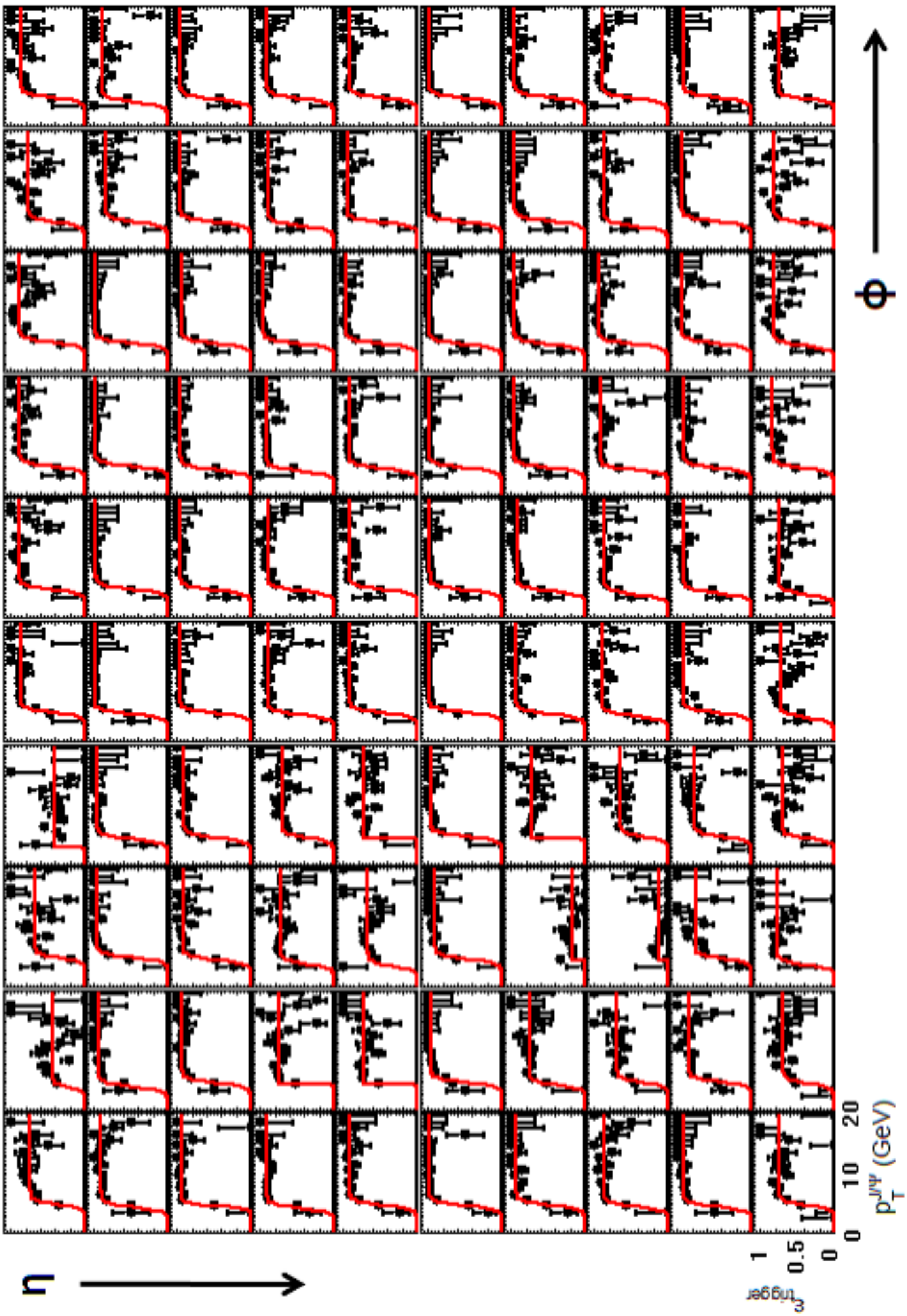

Fig. 8.2: Trigger efficiencies for each region in the barrel. The x-axis in each graph is p_T^{μ} in GeV from 0 GeV to 20 GeV. The y-axis means the trigger efficiency from 0 to 1.1. The top left corner represents the smallest point in η and ϕ. η increases with line number and ϕ increases with row number.

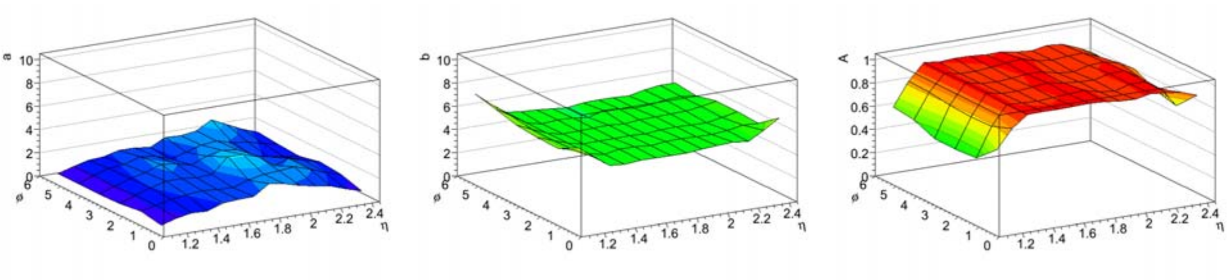

a b A

Fig. 8.3: Trigger efficiency map for the end-cap.

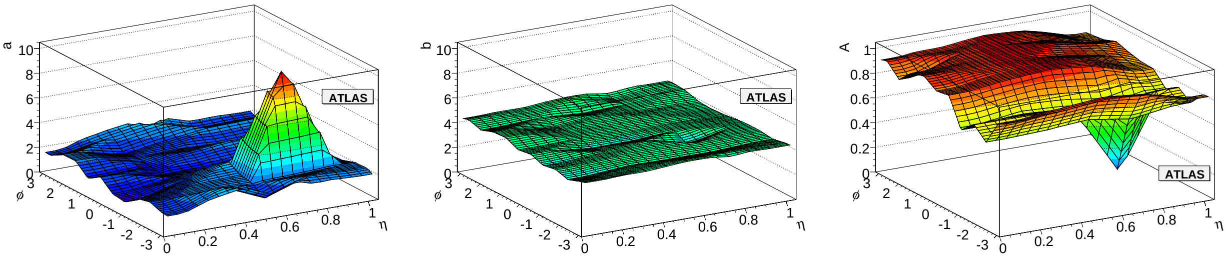

a b A

Fig. 8.4: Trigger efficiency map for the barrel.

8.2 Measurement of di-muon trigger efficiency for $J/\psi \to \mu\mu$ events

Di-muon trigger efficiency for J/ψ events can be calculated using the trigger efficiency map, taking into account the dependence on kinematic variables of the muons. For example, trigger efficiencies for J/ψ particles depend on the kinematical distribution of the two decay muons. Kinematical variables of the decay muons, p_T, η and ϕ, are functions of the J/ψ variables, $\cos\theta^*$ and ϕ^*. The value θ^* represents the decay angle of the muon in the J/ψ rest frame with the z-axis pointing to the J/ψ direction in the laboratory frame and ϕ^* is the azimuthal angle of the decay muon in the J/ψ rest frame. The efficiency, $\epsilon_{J/\psi}$ can be calculated using the muon trigger efficiencies as:

$$\epsilon_{J/\psi}(p_T^{J/\psi}, \eta^{J/\psi}, \phi^{J/\psi}) = \frac{1}{2\pi}\int\int \epsilon_{1\mu}(p_T^{\mu_1}, \eta^{\mu_1}, \phi^{\mu_1})\epsilon_{1\mu}(p_T^{\mu_2}, \eta^{\mu_2}, \phi^{\mu_2}) f(\cos\theta^*) d\cos\theta^* d\phi^*, \tag{8.3}$$

$f(\cos\theta^*)$ is the angular distribution of the decay muon from J/ψ normalized as

$$\int f(\cos\theta^*) d\cos\theta^* = 1. \tag{8.4}$$

To get the overall efficiency of J/ψ events, the integration on J/ψ variables must be performed in the kinematic region of the cross-section definition, as:

$$\epsilon_{J/\psi} = \int\int\int \epsilon_{J/\psi}(p_T^{J/\psi}, \eta^{J/\psi}, \phi^{J/\psi}) dp_T^{J/\psi} d\eta^{J/\psi} d\phi^{J/\psi}. \tag{8.5}$$

Kinematics of J/ψ in the Monte Carlo samples

Distributions of reconstructed J/ψ variables, $p_T^{J/\psi}$, $\eta^{J/\psi}$, $\phi^{J/\psi}$, $\cos\theta^*$ and ϕ^* after applying the selection criteria of muons ($p_T^\mu > 6$GeV and $|\eta^\mu| < 2.4$), are shown in Fig. 8.5. The open histograms are for all J/ψs in the Monte Carlo sample and the filled histograms are for events where the level-1 di-muon trigger, requiring at least two muons with $p_T > 6$GeV, is fired.

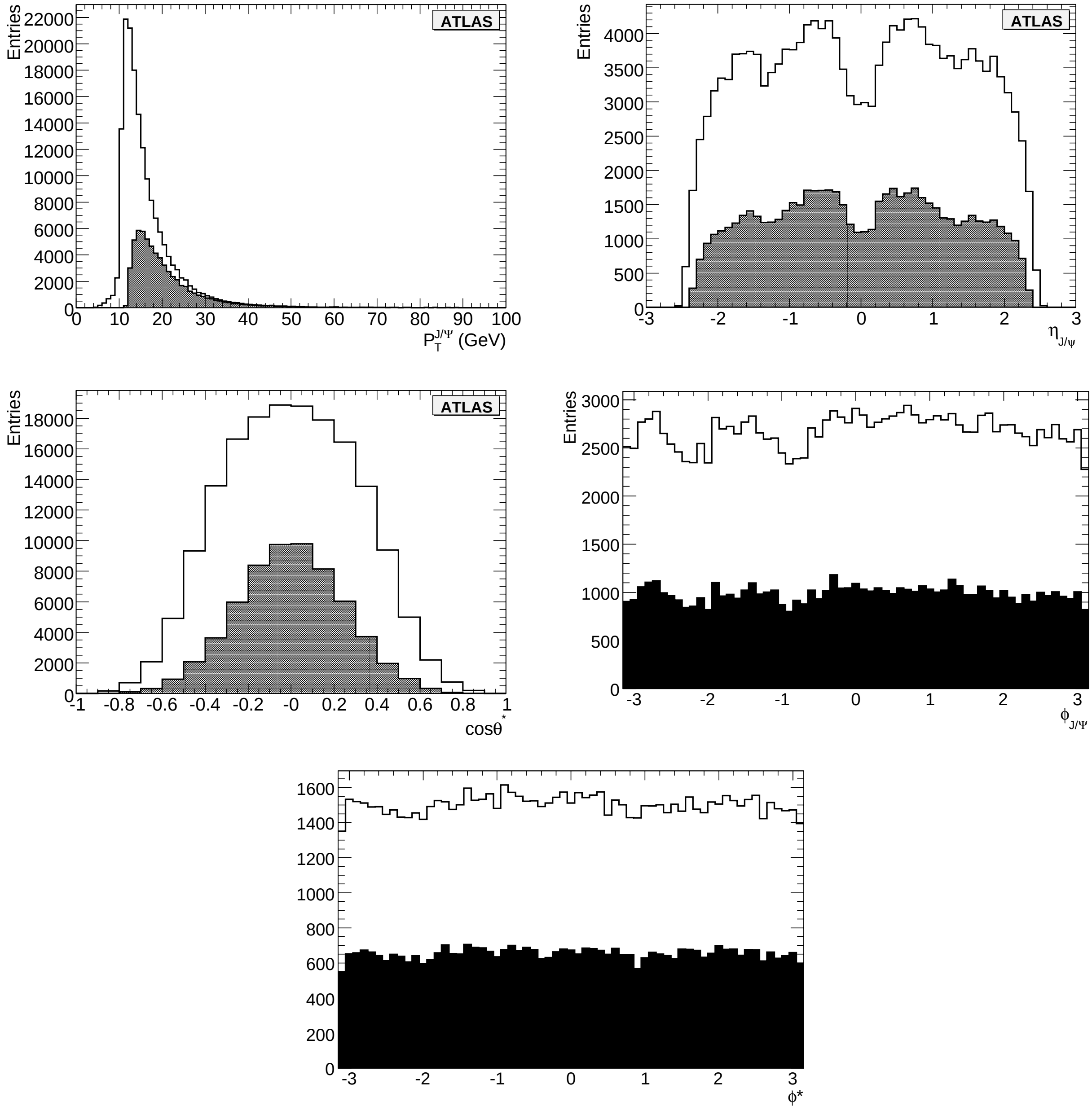

Fig. 8.5: J/ψ distributions.

The $\cos\theta^*$ distribution reflects the polarization state of the J/ψ and is flat without polarization. Since the $\cos\theta^*$ distribution itself is an interesting quantity to measure, we do not make any assumptions about this distribution but instead try to measure the efficiency as a function of $\cos\theta^*$. Although the generated $\cos\theta^*$ distributions are flat, reconstructed distributions may be biased by the p_T cuts applied at the generator level. For example, at $|\cos\theta^*| = 1$, one of the decay muons flies in the opposite direction to the J/ψ and has a low transverse momentum. Therefore, these events are more likely to be rejected by the p_T cut above.

Results and performance of the method

Figure 8.6 shows the J/ψ efficiencies as a function of $p_T^{J/\psi}$, $\eta^{J/\psi}$ and $\cos\theta^*$ calculated by the following two methods. The open circles represent the results obtained by checking the decision of the simulated level-1 di-muon trigger. The filled circles are the results using the trigger efficiency map. It can be seen that the efficiency drops at $\eta = \pm 1{,}0$ due to the layout of the muon trigger chambers. The difference between the two di-muon trigger efficiencies is most pronounced around $p_T^{J/\psi}$ =10 GeV. This is because the efficiency from the map uses only muons from J/ψ decay, while one from the trigger decision uses all muons in the event. If one or more muons are produced from sources other than J/ψ decay, such muons may be triggered so that the efficiency from the trigger decision becomes higher than that calculated from the map. The number of muons from sources other than J/ψ decay per event is shown in Fig. 8.7, where muons with p_T >6 GeV in $|\eta|$ <2.4 are counted. About 2 % of events have more than one such muons. Distribution of their p_T is also shown in Fig. 8.8.

The error bars in Fig. 8.6 represent the sum of the statistical and systematic errors added in quadrature. The statistical errors correspond to the 20 pb^{-1} of $J/\psi \rightarrow \mu\mu$ events. The systematic uncertainty of the method is estimated by taking difference from the results using another trigger efficiency map created as follows. The detector is divided into 16×16 regions of η and ϕ instead of 10×10 regions for the barrel and, for the end-cap, one octant is divided into 15×10 regions of η and ϕ instead of 10×6 regions. Then, the muon trigger efficiencies are fitted by another function because of the following reason. In some regions of the barrel, for example in the third graph from the left in the fourth line of Fig. 8.2 corresponding to $|\eta| \sim 0.35$ and $\phi \sim \frac{\pi}{4}$, the efficiency decreases at higher-p_T region. This is because high-p_T muons can not be triggered because of the absence of the detectors, while low-p_T muons can be triggered because their trajectories are well bent into the detectors around the structures. Therefore, the alternative fit function is:

$$\epsilon_{1\mu} = \frac{A - cp_T}{1 + e^{-a(p_T^{\mu} - b)}}, \tag{8.6}$$

where the term cp_T is added to describe the decrease of the efficiency at the plateau. Since there is no dead region of the trigger chamber in the end-cap region, the second fit function is used only for the barrel region.

Differences between the di-muon trigger efficiencies obtained by using the map and that obtained from the trigger decision are shown in Fig. 8.9, where the results using three different maps created with the standard method, the finer binning and the second fit function are shown. The statistical uncertainty is also indicated in the same figure. As seen in Fig. 8.9-(a), the differences in low-p_T region are reduced by using the finer binning. This may be because the finer binning can follow the sharp change of the muon trigger efficiency for low-p_T muons. In high-p_T region, the behavior of the efficiency using the second fit function is different from the others. Around $p_T^{J/\psi}$ =30 GeV, the result using the second fit function is better than the others. This represents that the new fit function can follow the decrease of the muon trigger efficiency better in this region. However, the difference becomes as large as that of the others in higher $p_T^{J/\psi}$ region, where enough statistics can not be obtained from available events so that the shape of the muon trigger efficiency can not be parameterized well. This may explain the difference in Fig. 8.9-(c) around $|\cos\theta^*| = 1$, where one of the two muons from J/ψ decay has comparatively high-p_T.

The systematic errors are of the order of the statistical errors. A more sophisticated parameterization on the trigger efficiency curve and the increasing number of binning may be used with larger statistics for reducing the remaining systematic errors, especially for high-p_T region and around the structures.

The overall efficiencies calculated in the kinematic region of $p_T > 12$ GeV and $|\eta| < 2$ are 76.1 % and 77.0 % using the trigger decision and the trigger efficiency map, respectively. The average di-muon trigger efficiency from $J/\psi \to \mu\mu$ events can be measured within the error of about 1 % for the integrated luminosity of about 20 pb^{-1}.

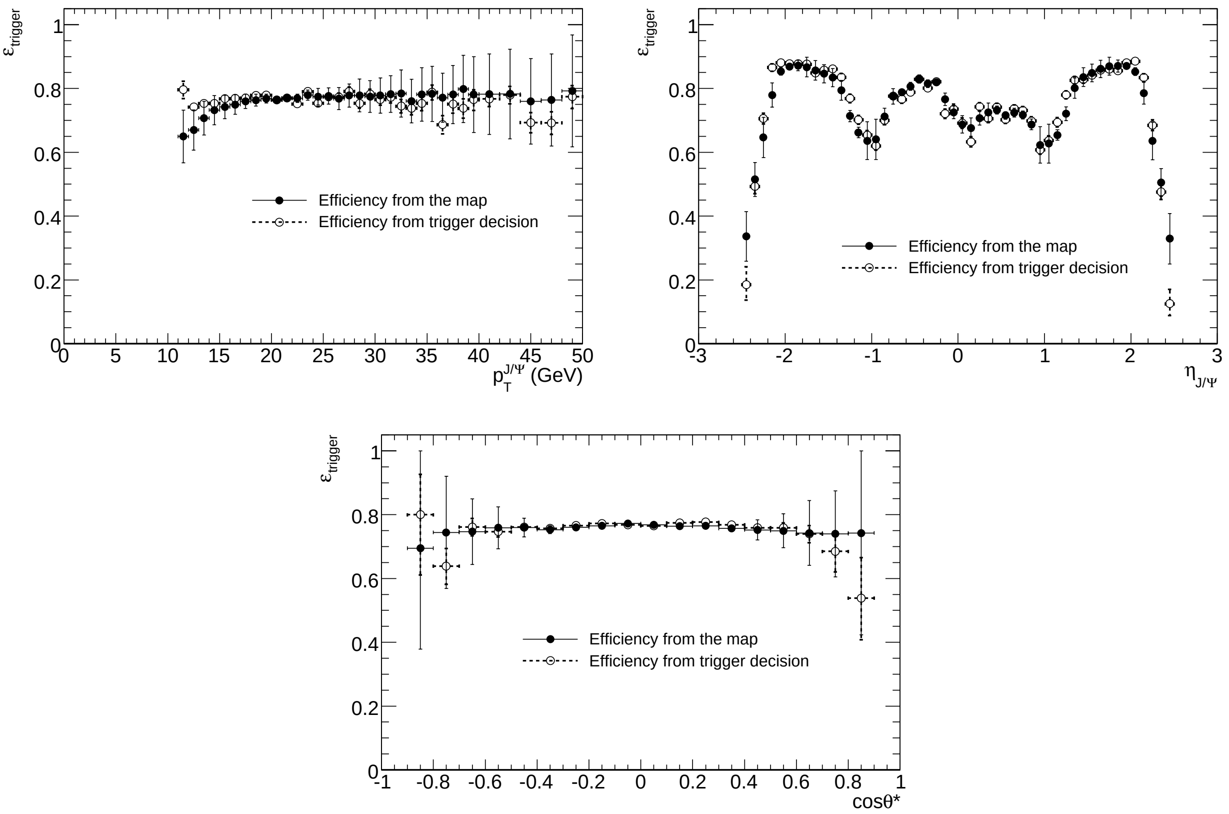

Fig. 8.6: Trigger efficiency for J/ψ events as a function of J/ψ kinematical variables.

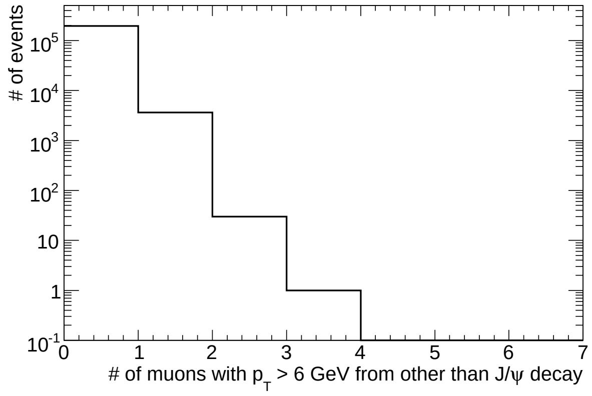

Fig. 8.7: Number of muons from other than J/ψ decay per event. Only muons with p_T >6 GeV in $|\eta|$ <2.4 are counted.

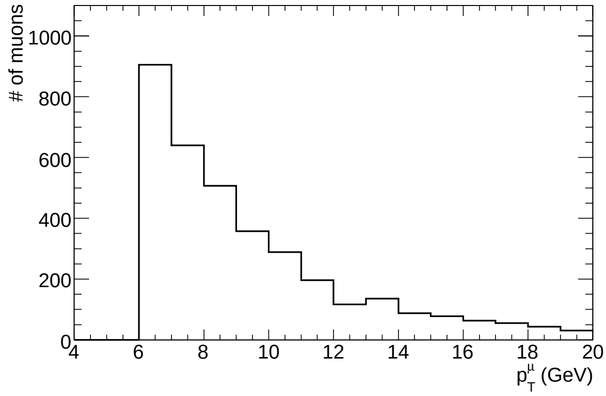

Fig. 8.8: Distribution of p_T of muons from other than J/ψ decay.

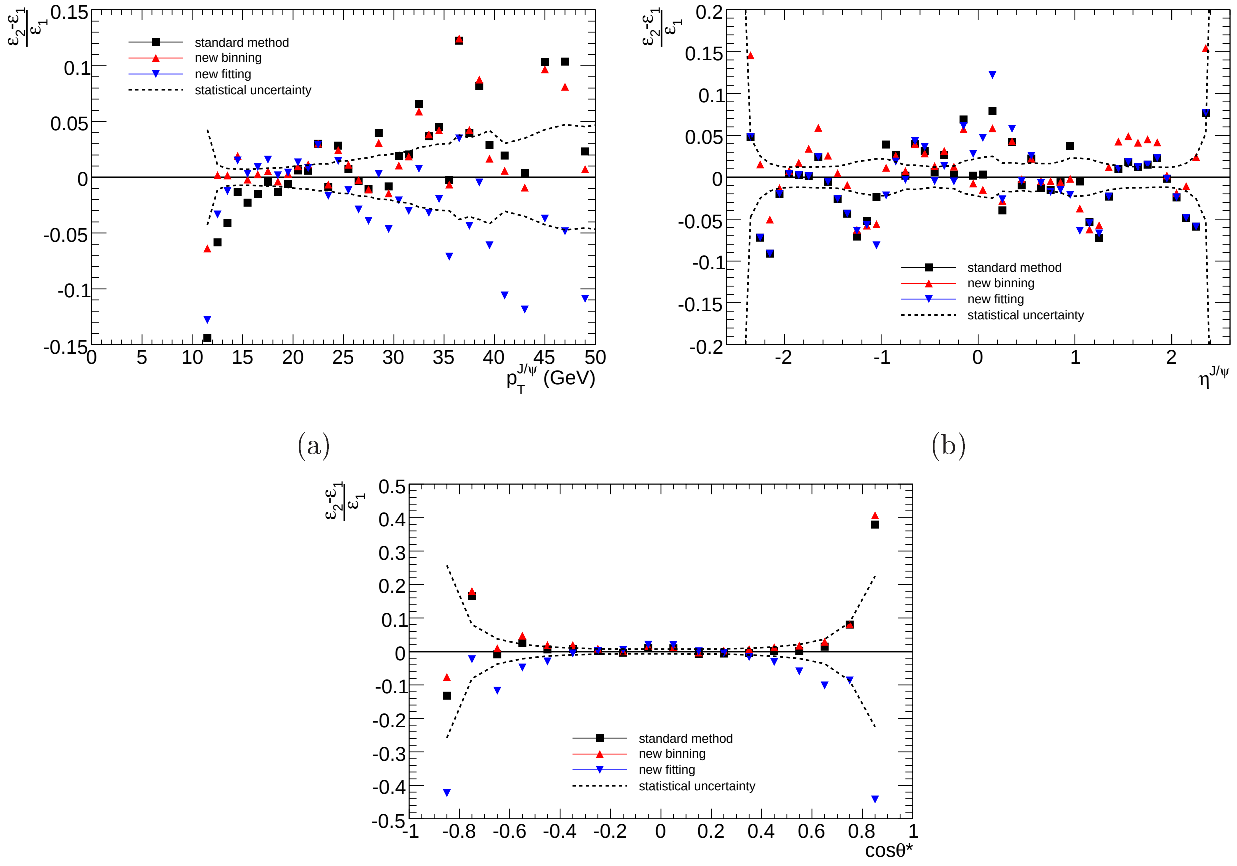

(a)

(b)

(c)

Fig. 8.9: Difference between the di-muon trigger efficiencies from the map and from the trigger decision as a function of J/ψ kinematical variables. The y-axis represents the value $\frac{\varepsilon 2-\varepsilon 1}{\varepsilon 1}$, where the value ε_1 is the efficiency from the trigger decision and ε_2 is one from each map. The statistical uncertainty of ε_2 divided by ε_1 is indicated in each figure.

9 Summary

In autumn 2009, the ATLAS experiment at the Large Hadron Collider will start, where we can search for the Higgs boson and explore new physics beyond the Standard Model. The event trigger system is very important to pick up rare signal events in the large background environments.

Muon trigger efficiency is very important for evaluating the performance of the muon trigger and for the cross-section measurement. It should be directly measured from collision data. In this study, the following two methods are examined using the Monte Carlo simulation and their performances are evaluated by comparing the results with those from the single muon samples.

The first method uses the level-1 calorimeter trigger to collect events. Since the calorimeter trigger is independent from the muon trigger, muons can be selected by only some track quality cuts for the muon trigger efficiency measurement. In this study, this method is applied to the Monte Carlo di-jet samples triggered by the level-1 single jet trigger. In order to reduce the effect of mis-reconstructed and fake muons in the events, only the combined and isolated muons fitted with low reduced χ^2 were used. As a result, it is expected that the muon trigger efficiency can be measured within a systematic error of about 5 %. Due to the large statistics expected, this method is useful in the early stage of the data taking. However, due to the systematic uncertainties from the background sources and included in the simulation, this method may not be appropriate for the precise measurement.

The second method is called tag-and-probe method, which uses di-muon events triggered by the level-1 single muon trigger. This method is much less affected by quality of reconstruction, uncertainties in simulation and amount of background than the first method. By using the invariant mass for the muon selection, higher purity of reconstructed muons can be achieved. In this study, $J/\psi \to \mu\mu$ samples and $Z \to \mu\mu$ samples are used. The former is appropriate for the measurement for low-p_T muons (p_T <15 GeV) and the latter for high-p_T muons (p_T >15 GeV). Muons can be obtained in the whole detector regions from both processes. After applying the muon selection, about 20 % of $J/\psi \to \mu\mu$ events and about 40 % of $Z \to \mu\mu$ events are collected.

Using the method, the muon trigger efficiency is measured as a function of p_T, η and ϕ. As a result, it is expected that the muon trigger efficiency as a function of p_T can be measured with the statistical uncertainty of a few percent at the threshold and about 0.1 % at the plateau for the integrated luminosity of 100 pb^{-1}. The effects from the background events are also evaluated. The effect is a few percent for low-p_T region and less than 1 % at the plateau.

By measuring the muon trigger efficiency as a function of p_T for each subdivided region of η and ϕ using the tag-and-probe method, the muon trigger efficiency map is created. This map represents the p_T, η and ϕ dependency of the muon trigger efficiency, which is quite useful for various physics measurements (crosssections, primary distributions of produced particles, multi-muon trigger efficiencies, etc.). In this study, a strategy to measure the di-muon trigger efficiency is described as an applied use of the map. For this purpose, the trigger efficiency map is created by measuring the muon trigger efficiency as a function of p_T for each subdivided region of η and ϕ. Using the map, the di-muon trigger efficiency for $J/\psi \to \mu\mu$ events is calculated as the product of the muon trigger efficiency for each decay muon. The performance of this method is evaluated by comparing the results with the decision of the level-1 di-muon trigger itself. As a result, it is expected that the di-muon trigger efficiency for $J/\psi \to \mu\mu$ events can be measured within the error of 1 % in average.

In this thesis, strategies for measuring the muon trigger efficiency and the di-muon trigger efficiency are established and their performances are assured by the Monte Carlo simulation. Tools for all methods have been already developed and are waiting for the optimization using the collision data. When the data taking starts, the muon trigger efficiency will be measured by the tag-and-probe method for all physics studies requiring the muon trigger.

Appendix

Performance of TGC under neutron irradiation

When the ATLAS experiment starts, a large amount of radiation background is expected around the ATLAS detectors. Detectors must work stably under such an environment. Especially, neutron can affect the detector operation badly for the following reason. Neutrons of a few hundred keV to a few tens of MeV cause a scattering of nuclei in the materials and produced nuclei of less than 10 MeV has a large stopping power. For example, if a proton of 1 MeV crosses the gas volume in TGC for a few millimeters, it deposits almost all kinematic energy as ionized gas in a small localized area. The density of an electron cloud produced by such a proton of a few MeV is estimated to be 10^2-10^3 times larger than that produced by a minimum ionization particle (MIP) such as a cosmic muon. These large deposited energies not only create huge pulse signals but also cause discharges between an anode wire and cathode plane. Protons of less than 10 MeV cannot achieve a gas volume by going through the TGC surface structure, but neutrons recoiled by protons can be emitted inside the gas volume. Thus, performance study of TGC for intense neutron is important.

The performance study was performed using 2.5 MeV and 14 MeV neutrons provided by a Fusion Neutronics Source (FNS) beamline at Japan Atomic Energy Agency (JAEA). These neutrons are produced through the following processes:

- $D + D \rightarrow^3 He + n + 3.27MeV$ (2.5 MeV),
- $D + T \rightarrow^4 He + n + 17.6MeV$ (14 MeV),

where Deuteron ions are accelerated to 350 keV using a Cockcroft-Walton accelerator and then extracted to an experimental room and with Deuteron or Tritium target.

In this study, the following four contents are studied.

Detection efficiencies of TGC for neutrons

The detection efficiencies are measured to be 2.4 % and 8.3 % for 2.5 and 14 MeV neutrons, respectively. The difference are well explained with a detector simulation using GEANT4. As shown in Fig. 9.1, neutron sensitivity due to interactions in the gas becomes smaller against the neutron energy, while contribution by the main TGC structure, FR4 becomes much larger with the energy. The sensitivity is about three times larger at the energy of 14 MeV than at the energy of 2.5 MeV. This well explains the experimental result.

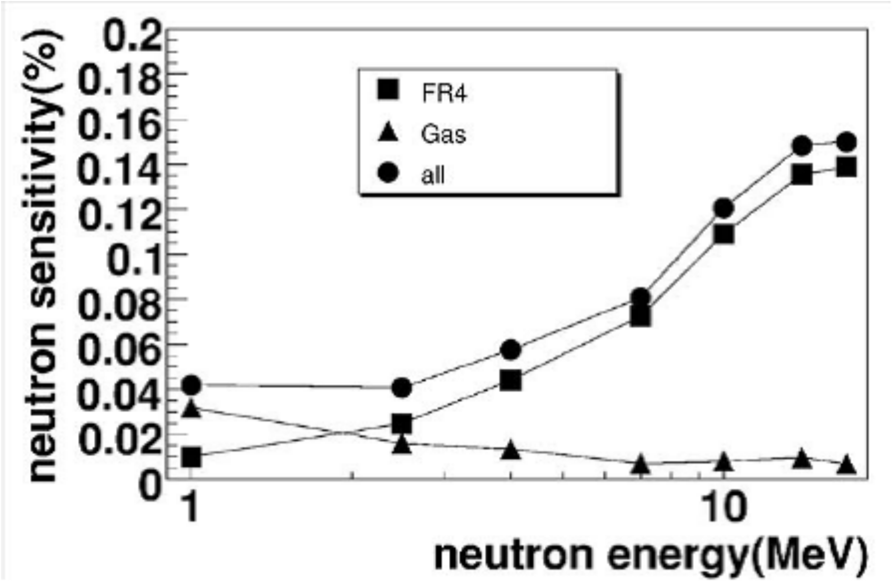

Fig. 9.1: Neutron sensitivity as a function of neutron energy for TGC components (gas and FR4) by GEANT4 simulation.

Output charge of TGC for neutrons

Charge distributions from the output pulse irradiating 2.5 and 14 MeV neutron are shown in Figs. 9.2 and 9.3, respectively. The operation voltage is 3.1 kV which is almost the same condition at ATLAS. For each distribution, the lower peaks are caused by gamma rays and the larger peaks are caused by neutrons. There can be seen the following phenomena:

- the neutron peak by 2.5 MeV neutrons is broader than that by 14 MeV neutrons;
- the mode value of the distribution by 2.5 MeV neutrons is greater than that by 14 MeV neutrons.

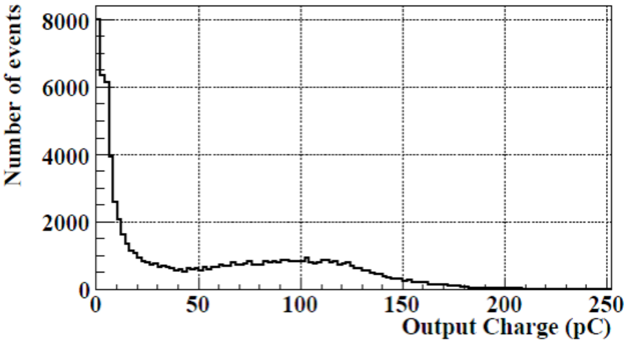

Fig. 9.2: Output charge distribution in the case irradiating 2.5 MeV neutrons.

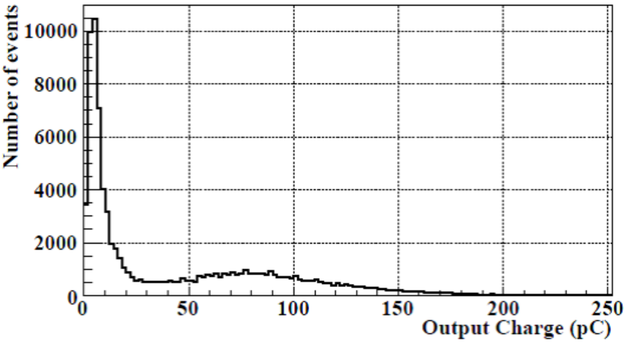

Fig. 9.3: Output charge distribution in the case irradiating 14 MeV neutrons.

Discharge rate

Discharge probabilities are measured for several operation voltages. The result is shown in Fig. 9.4. The discharge probability for 14 MeV neutrons is about 10^{-9} count/neutron for the operation voltage of 3.1 kV, while no discharge was observed during this study for the operation voltage less than 3.8 kV for 2.5 MeV neutrons.

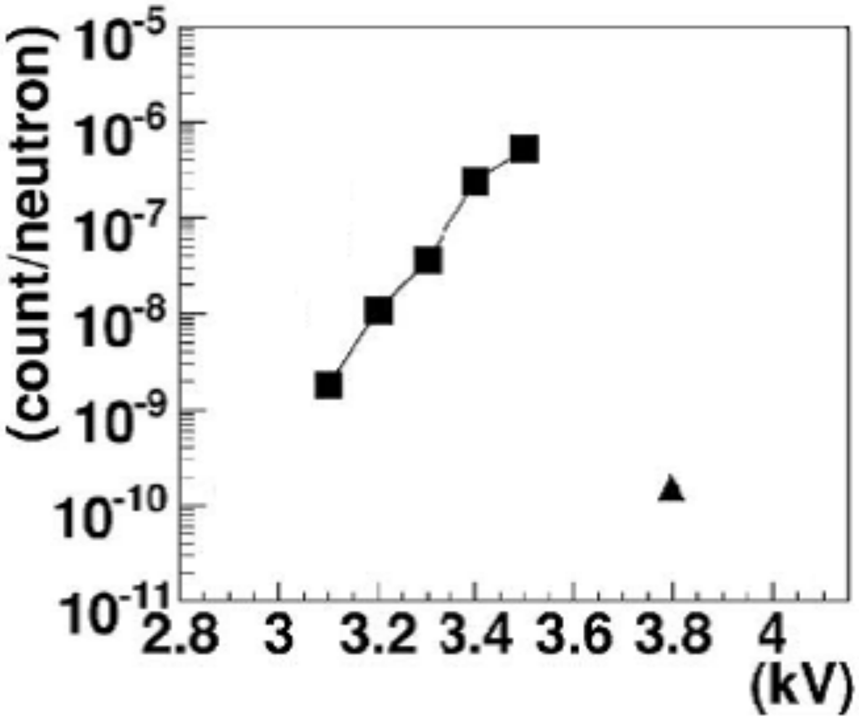

Fig. 9.4: Discharge probability as a function of operation voltage. Triangle plot shows that for 2.5 MeV neutrons and square ones show that for 14 MeV neutrons.

Aging

In this study, two TGCs (named TGC1 and TGC2) were irradiated with 14 MeV neutrons. TGC2 was placed about three times farther from the Tritium target than TGC1. By measuring the output charge of each TGC for ^{90}Sr-β rays before and after the irradiation, the degradation of TGCs by neutrons was estimated. Through the test, typical neutron frequency was 3.1×10^{7} neutrons/cm^{2}/s for TGC1 and 3.3×10^{6} neutrons/cm^{2}/s for TGC2, respectively. Total deposited energy in the gas volume of TGC1 was 2.73×10^{8} MeV/cm^{2} corresponding to about 60 years of operation at the ATLAS middle station. For TGC2, it was 2.87×10^{7} MeV/cm^{2} corresponding to about 15 years of operation at the same position.

Figure 9.5 shows the peak value of the output charge distribution of the TGCs for ^{90}Sr-β rays. There can be seen some decrement for both results of TGC1 and TGC2. For example, the output charge was reduced by 16 % for TGC1 and 11 % for TGC2 at the operation voltage of 2.9 kV. However, both TGC1 and TGC2 still have more than 99.0 % of detection efficiency for cosmic muons at the operation voltage of 2.7 kV and less than 25 ns of time jitter at the operation voltage of 2.8 kV.

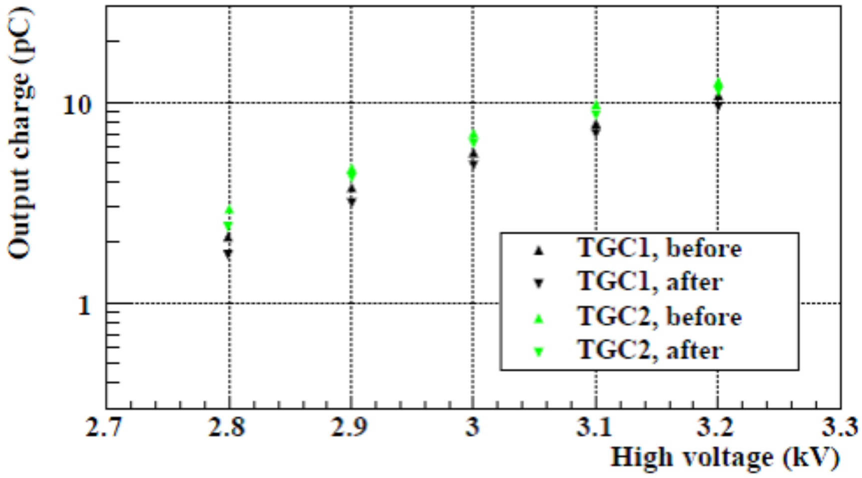

Fig. 9.5: Peak value of the output charge of TGCs for ^{90}Sr-β rays before and after the irradiation.

Conclusion

Through the test, TGCs were stably operated and kept their efficiencies enough high. Therefore, TGCs can work well more than 10 years after the data taking starts. Details of this study is in [35][36].

Acknowledgement

My heartfelt appreciation goes to Prof. Hisaya Kurashige whose comments and suggestions were innumerably valuable throughout the course of my study. I'm also indebt to Prof. Kiyotomo Kawagoe, Prof. Yuji Yamazaki and Prof. Hiroshi Takeda whose comments made enormous contribution to my work. The supports offered by Dr. Atsuhiko Ochi, Dr. Takashi Matsushita and Dr. Akimasa Ishikawa were also invaluable.

I would like to thank Prof. Takahiko Kondo, Prof. Katsuo Tokushuku, Prof. Hiroyuki Iwasaki and Prof. Tomio Kobayashi for their supports and encouragements.

I am deeply grateful to Dr. Takanori Kono (CERN) and Dr. Naoko Kanaya (ICEPP) who taught me various knowledge and techniques for developing the tools and analyzing the data, which provided great support for my study. I also appreciate the advices and supports offered by Mr. Chihiro Omachi. I hope his study will be successful. Discussions with ATLAS-Japan-HLT members have been illuminating. I would like to thank all collaborators for their supports and encouragements.

My stay in Geneva was tough but fulfilling with my good friends and colleagues. I would like to thank them with all my heart and I'm looking forward to seeing them in the near future.

Finally, I would like to express my gratitude to my family and my friends for their moral support and warm encouragements, and I would like to send my special thanks to my father.

Reference

[1] S.Weinberg, Phys. Rev. Lett. **19** (1967) 1264

[2] A.Salam, *Elementary Particle Theory*, ed. N.Svartholm (Almquist and Wiksells, Stockholm, 1968) 367

[3] S.L.Glashow, J.Iliopoulos and L.Maiani, Phys. Rev. **D2** (1970) 1285

[4] P.W. Higgs, Broken symmetries, massless particles and gauge fields, Phys. Lett. **12** (1964) 132-133.

[5] P. W. Higgs, Spontaneous symmetry breakdown without massless bosons, Phys. Rev. **145** (1966) 1156-1163.

[6] P. W. Higgs, Broken symmetries and the masses of gauge bosons, Phys. Rev. Lett. **13** (1964) 508-509.

[7] LEP Collaborations and LEP Electroweak Working Group, A Combination of Preliminary Electroweak Measurements and Constraints on the Standard Model, LEPEWWG/2005-01, hep-ex/0511027, 9 November 2005

[8] J.F.de Troconiz and F.J.Yndurain, Phys. Rev. **D71** (2005) 073008.

[9] M.Spira and P.M.Zerwars, Electroweak Symmetry Breaking and Higgs Physics, hep-ph/9803257 (1997)

[10] S.Asai et al., Prospects for the Search for a Standard Model Higgs Boson in ATLAS using Vector Boson Fusion, Eur. Phys. J. **C32S2** (2004) 19-54

[11] J. Wess and B. Zumino, Nucl Phys. B70, (1974) 39.

[12] P. Fayet and S. Ferrara, Phys. Rep. 32, (1977) 249.

[13] H. P. Nilles, Phys. Rep. 110, (1984) 1.

[14] H, Haber and G. Kane, Phys. Rep. 117, (1985) 75.

[15] R, Barbieri, Riv. Nuovo Cimento. 11, (1988) 1.

[16] W. de Boer and C. Sander, Phys. Lett. B585 (2004) 276.

[17] J. R. Ellis, S. Heinemeyer, K. Olive and G. Weiglein, JHEP 0502 (2005) 13.

[18] H. Baer, C. H. Chen, F. Paige and X. Tera, Phys. Rev. D52, (1995) 2746.

[19] 10. A. Chamseddine, R. Arnowitt and P. Nath, Phys. Rev. Lett. 49 (1982) 970.

[20] 11. R. Barbieri, S. Ferrara and C. Savoy, Phys. Lett. B119 (1982) 343.

[21] 12. N. Ohta, Prog. Theor. Phys. 70 (1983) 542.

[22] 13. L. Hall, J. Lykken and S. Weinberg, Phys. Rev. D27 (1983) 2359.

[23] S.Yamamoto, Strategy for early SUSY searches at ATLAS, ATL-PHYS-CONF-2008-001;ATL-COM-PHYS-2007-081

[24] R.K.Ellis and S.Veseli, Phys. Rev. **D60** (1999) 011501.

[25] H.Georgi, S.Glashow, M.Machacek, and D.V.Napnoulos, Phys. Rev. Lett. **40** (1978) 692.

[26] A.Djouadi, M.Spira, and P.M.Zerwas, Phys. Lett. B264 440 (1991); S. Dawson, Nucl. Phys. **B359** (1991) 283.

[27] CERN Public home ,http://public.web.cern.ch/public/

[28] LHC Design Report, CERN/-2004-003, 4 June 2004.

[29] ATLAS Collaboration, ATLAS DETECTOR AND PHYSICS PERFORMANCE Technical Design Report Volume I, CERN/LHCC/99-14 ATLAS TDR (1999)

[30] ATLAS Collaboration, Calorimeter Performance Technical Design Report, CERN/LHCC 96-40 (1997).

[31] ATLAS Collaboration, Muon Spectrometer Technical Design Report, CERN/LHCC 97-22 (1997).

[32] ATLAS Collaboration, The ATLAS Experiment at the CERN Large Hadron Collider, JINST 3 S08003 (2008)

[33] ATLAS Collaboration, ATLAS Trigger Performance Status Report, CERN/LHCC 98-15 (1998)

[34] ATLAS Collaboration, ATLAS Level1 Trigger Technical Design Report, ATLAS TDR-12 (1998)

[35] A. Ochi et al., Thin gap chamber performance tests under several MeV neutron sources, American Institute of Physics Vol.77, 10E709(2006)

[36] H. Ohshita et al., Neutron irradiation test of an ATLAS Thin Gap Chamber, Nucl. Instrum. Methods **A587** (2008) 259-265

Figure List

Table List